Development and Validation of Fluid-Structure Interaction in Aircraft Crashworthiness Studies

Matthew R. Satterwhite

Thesis submitted to the Faculty of the
Virginia Polytechnic Institute and State University
in partial fulfillment of the requirements for the degree of

Master of Science
In
Mechanical Engineering

Javid Bayandor, Chair
Francine Battaglia
Robert West

July 19, 2013
Blacksburg, Virginia

Keywords: aircraft ditching, finite element analysis, fluid-solid interaction, composite materials

Abstract

Current Federal Aviation Regulations require costly and time consuming crashworthiness testing to certify aircraft. These tests are only capable of a limited assessment of progressive damage and all crash configurations and scenarios cannot be physically evaluated. Advancements in technology have led to accurate and effective developments in numerical modeling that have the possibility of replacing these rigorous physical experiments. Through finite element analysis, an in-depth investigation of an aircraft equipped with a fabricated composite undercarriage was evaluated during water ditching. The severe impact of aircraft ditching is dynamic and nonlinear in nature; the goal of this work to develop a methodology that not only captures the structural response of the aircraft, but also the fluidic behavior of the water. Fundamental studies were first conducted on a well-researched fluid-solid interaction problem, the water entry of a wedge. Typical modeling strategies did not capture the desired detail of the event. An advanced meshing scheme combining meshed and meshless Lagrangian techniques was developed and multiple wedge angles were tested and compared to analytic and qualitative results. The meshing technique proved valid, as the difficult to model phenomena of splashing was captured and the maximum impact force was within five percent of analytical calculations for the 20° and 30° deadrise wedge. Physical small scale aircraft ditching experiments were then performed with an innovative testing platform capable of producing varied aircraft approach configurations. The model was outfitted with an instrumented composite undercarriage to record data throughout the impact while a high-speed camera recorded the event. Numerical simulations of the model aircraft were then compared to experimental results with a strong correlation. This methodology was then ultimately tested on a deformable model of a fuselage section of a full-size aircraft.

Dedication

To

My parents, thank you for all your love and support.

Acknowledgements

I would like to thank those people that had a large influence on my growth as an individual and engineer throughout my graduate studies. First, I must thank my advisor Dr. Javid Bayandor for seeing my potential and giving me an opportunity to work in such an exciting field. His insight and dedication molded me into a first-rate researcher and engineer. I am also grateful to Dr. Francine Battaglia, who was an invaluable asset to me, both professionally and personally. She always set aside time with talk me and provide much needed knowledge and guidance. I must also thank Dr. Robert West, for sharing his knowledge in the field of finite elements. A lot of my research is based off his methods and teachings, especially the often overlooked 'first-cut' of a problem.

I must acknowledge the members of the CRASH Lab for their help and camaraderie throughout my time at Virginia Tech; especially Yangkun, my partner in crime these past two years. I had a great time working with you all and could not ask for better labmates. I would also like recognize the 2012 and 2013 IMPACT teams for their hard work in constructing the experimental test stand and conducting time consuming tests.

Contents

List of Figures

List of Tables

Nomenclature

1-2-3	local coordinate system
A	area
C_{ij}	compliance component
E	Young's modulus
F	force
Fr	Froude number
g	gravity
G	shear modulus
L	length
M_i	mass of wedge
m	mass of displaced water calculated by von Karman
m_w	Mass of displaced water calculated by Wagner
Re	Reynolds number
v	velocity
v_c	constant velocity
v_o	initial impact velocity
V^f	fiber volume fraction
W	smoothing kernel function
w	weight
x-y-z	global coordinate system
α	deadrise angle
ε	strain
ζ	damping ratio

ρ	density
σ	stress
κ	curvature
μ	viscosity
Π	Non-dimensional parameter
τ	shear stress
ω_d	damped natural frequency
ω_n	natural frequency

Chapter 1. Introduction

Aircraft water ditching is becoming an increasingly important topic in commercial aviation. Since 1996 there have been six reported cases in which large commercial aircraft have been ditched, with more than seventeen similar cases dating back to 1952 [1]. The results of ditching are typically catastrophic, resulting in structural failure and loss of passenger life as the aircraft is not particularly designed for soft terrain impact. While regulations set forth by the Federal Aviation Administration (FAA) are extremely stringent, more analysis is needed to improve aircraft structural integrity to meet the FAA's new vision "Destination 2025"; a goal of zero fatal aircraft accidents by the year 2025 [2]. To achieve this objective, new analysis techniques have been investigated to create a numerical analysis methodology to evaluate aircraft crashworthiness and ultimately increase passenger safety.

Ditching is classified as a controlled emergency landing on water or other soft terrain and can be organized into three main phases: aircraft conditions prior to impact, structural response at impact, and ensuing floatation time [3]. This research focuses mainly on the second phase, the impact, but it is important to highlight the significance of all three ditching stages.

For a successful ditching, control of the aircraft is vital. Depending on the source of emergency, from foreign object damage to hydraulic system failure, each scenario limits the amount of control the pilot has over the aircraft. The damage conditions in turn control the way in which the aircraft is ditched. A ditching with functional engines is much more feasible than without [4]. This is due to the fact that the pilot has the ability to maintain an air speed above the stall limit to control the speed, glide angle, and attitude of the aircraft. An aircraft that has the capability to ditch with an approach similar to that of normal landing will have the highest probability of success.

An example of an aircraft that ditched with incorrect settings can be seen in the photo sequence in Figure 1.1. The aircraft is the high jacked Ethiopian Airlines Flight 961. After extended loitering, the aircraft ran out of fuel and the pilot attempted to ditch. The aircraft approached the water with a high roll angle, causing the left wing tip to hit the water first. This created a combined

pitch-yaw moment about the body of the plane and violently sheared the aircraft apart. The impact resulted in catastrophic failure of the aircraft, and of the 175 passengers onboard only 50 survived.

Figure 1.1: Failed ditching of Ethiopian Airlines Flight 961.

For a ditching to be disastrous, the aircraft does not necessarily have to approach at such an extreme orientation as shown above. The damage sustained by an aircraft during a soft terrain impact, such as ditching, is much different than a hard surface impact like that of a belly landing on a runway. Aircraft are designed to structurally withstand dynamic hard impacts. Frames and ribs, which compose the structure, effectively redirect and carry the hard impact loads. Imbedded crush mechanisms within the structure absorb energy and reduce the dynamic force transferred to the passengers. In a soft terrain impact, like that of the second phase of water ditching, these mechanisms cannot be fully utilized when the force is not entirely supported by the internal structure. Rather, the frames along with the undercarriage bays are subjected to an enveloping pressure load. Bays covered only by skin panels are not designed to sustain pressure loads and usually rupture. Figure 1.2 is a graph of the undercarriage of an Airbus A320, the aircraft from the US Airways Flight 1549 incident that ditched into the Hudson River after flying into a flock of Canadian geese. With disabled engines, the pilot decided to land the aircraft in the safest place available, the river. The destruction to the undercarriage demonstrates the inability of the panels to

handle such loads under hard ditching conditions. Fortunately, all of the passengers onboard survived, but the rear pressure bulkhead along with the connecting rear skin panels ruptured resulting in a relatively rapid sink rate [5].

Figure 1.2: Ruptured undercarriage bays of the Airbus A320 that ditched in the Hudson River.

The third phase of ditching is the floatation time after impact. Large passenger aircraft are specifically designed with low wings to produce buoyancy in ditching scenarios. With a sealed cabin, the buoyant force holds the fuselage out of the water, allowing for passengers and crew to exit the aircraft before it submerges. If the aircraft is damaged to the extent of Flight 1549 with ruptured bays and pressure bulkhead, the floatation time is drastically reduced. If this incident occurred hundreds of miles from rescue assistance, the results could have been drastically different.

To increase the fuel efficiency and strength of aircraft structures, manufacturers have introduced lightweight composite materials on the current generation of aircraft. These materials have failure mechanisms much different than standard metals that are much harder to predict. Figure 1.3 highlights the small percentage of composite materials used on previous generations of aircraft compared to contemporary designs, where over fifty percent of the structure composed of composites. Accurate failure models for composite materials are vital as the aircraft industry continues to implement novel material systems onto aircraft.

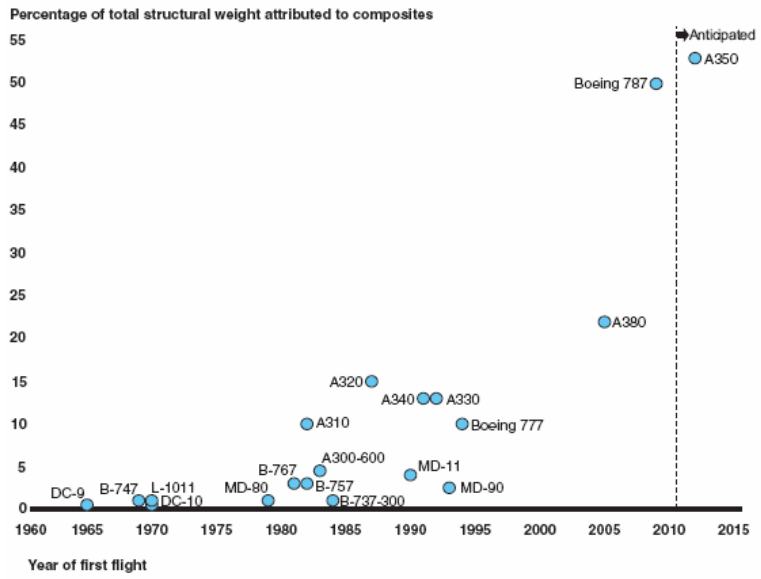

Figure 1.3: The growth of composite materials used in aircraft structures [6].

With the rapid improvement in computational capacity and development of accurate numerical analysis methods, high fidelity numerical investigations into the crashworthiness of aircraft designs are possible. Virtually simulating aircraft designs can reduce the number of experimental tests, developmental costs, and give better insight into progressive damage of the structure. To simulate aircraft ditching, fluid-structure interaction (FSI), also referred to as fluid-solid interaction, must be modeled as the aircraft impacts the water. This involves the coupling of fluid flow and structure mechanics, two fields which are normally solved through separate methods. Computational Fluid Dynamics (CFD) is developed based on the Navier-Stokes equations which define single phase fluid flow perfect for modeling water, while structures are discretized through finite element analysis (FEA) built upon minimum potential energy and the principle of virtual work. However, with the evolution of FEA, accurate modeling of fluids, while it is not as evolved for fluid analysis as CFD, is possible and will be used in this research to capture real time structural deformation and resulting fluid response.

1.1 Project Definition and Scope

The objective of this study is to develop a methodology to accurately model an aircraft structure in an emergency ditching event. This numerical analysis approach will be supported through analytical calculations and experimental results to precisely model the nonlinear FSI

between two drastically different material types: a solid structure and a fluid medium. Future aircraft designs can be enhanced by this novel analysis platform as manufacturers will have the capability to numerically test the crashworthiness of a design concept before it is physically built.

Small scale validation will first be conducted to ensure the foundation of the methodology is sound and accurate. This will be accomplished through a fundamental FSI experiment, ensuring the proper physics are present and accounted for during an impact event (Chapter 4). A FEA will be conducted on a representative FSI problem, the water entry of a rigid wedge. It was discovered typical FEA methods could not capture the complexities of the event. Combining meshed and meshless Lagrangian techniques, a novel advanced meshing scheme will be developed to capture the intricacies of the fluid behavior, including separation and wave generation. Qualitative numerical results will be validated against experimental testing while quantitative results will be compared to analytical solutions.

Next, composite models will be validated using an explicit FEA approach. Composite materials will be incorporated within the methodology to reflect the materials in present-day aircraft. The unknown material properties of a fabricated composite undercarriage will be analytically calculated through Classical Lamination Theory and compared to tension test results. These properties will then be implemented into the numerical analysis and subjected to the tension seen in the physical trial to ensure that the composite materials and element formulation are performing as expected.

After accurately verifying FSI and composite material models on a more basic level, physical and virtual ditching tests of a scaled model Boeing 747-400 will be undertaken (Chapter 6). Physical experiments will be conducted on a scaled plane with an instrumented composite undercarriage to capture damage and impact force as it is ditched. This data will then be used to calibrate the FEA simulations based on the parameters in the physical experimentation. Through dimensional analysis, based on the conservation of momentum, it will be examined whether this small scale model will have similar impact characteristics as that of a full-size aircraft. An initial ‘first cut’ of this problem will be conducted on a fuselage section of an aircraft to analyze the deformation of the structure as it impact water (Chapter 7).

Chapter 2. Literature Review

This chapter is a review of previous research that is related to the development of this aircraft ditching methodology and is divided into two parts. The first section is an overview of basic FSI problems centered on wedge water entry studies. The second section is an examination of more complex FSI problems involving aircraft ditching with incorporated structural damage and the context of the present work.

2.1 Wedge Studies

The earliest research on fluid-solid interaction impact problems was developed based on a two-dimensional rigid wedge impacting a calm water free-surface. von Karman [7] first developed the wedge problem as a way to analytically determine the forces exerted on the bottom of seaplane pontoons during landing. His analysis was based on the conservation of momentum from which penetration depth, sinking velocity, force, and average impact pressure was calculated for a variable velocity wedge. This work was expanded upon by Wagner [8] who accounted for changing boundary conditions with a rising water elevation along the edge of the impacting wedge. He calculated the pressure distribution along the wedge for a constant decent velocity. Sydow [9] combined the work of von Karman and Wagner and developed a force equation for a wedge with variable velocity, accounting for the virtual mass of the elevated water. These three early formulations assume ideal conditions; neglecting viscosity, buoyancy, and compressibility effects. Gravity is also assumed to be negligible due to the large accelerations of the fluid particles and the small time duration of the impact. Since then, numerous other reports have been published analyzing wedge/water impact, but the approximate calculations from these models have matched experimental results well.

Mayo [10] expanded upon the earlier theories on seaplane pontoons by analyzing an oblique wedge impact with downward and forward motion. He found that the previous theories' treatment of the constant total momentum of the float and constant virtual mass of the water is valid when the wedge only has a vertical velocity component. In an oblique impact, the forward motion results in lost momentum in the downwash of the float. Therefore, when testing it is important to insure

that the wedge impacts with only a vertical velocity to compare to von Karman, Wager, and Sydow's analytical formulations.

Dobrovolskaya [11] developed a two dimensional water entry theory based on Wagner's models and similitude. The similarity solution, as it is referred to, is a numerical analysis of a uniform symmetrical entry of a wedge into a half-plane of fluid. Zhao and Faltinsen [12] created a fully nonlinear numerical method based on potential flow theory to predict impact forces two dimensional wedge. Based on Dobrovolskaya's similarity solution, Zhao et al. was able to match experimental results of wedge with a wide range of deadrise angles. The models however, suffer from the inability to model large deformation and fragmentation (splashing) of the fluid, limiting the ability to simulate water entry beyond separation of the jet.

The FSI analysis of the wedge impact model has also been used by naval engineers to study the effects of wave slam on pier pillions. Rather than solving the interaction based on a sharp deadrise angle, calculations are performed on blunt cylindrical shapes. Cointe [13]-[14] considered the effects of a cylinder impacting a calm water surface modeled through an asymptotic matching approach. Inner and outer domains were specified and the behaviors were equated at the asymptote. Through this model Cointe found that the assumptions made by previous researchers considering an incompressible and inviscid fluid without surface tension or gravity allowed for accurate predictions of impact force.

A method to capture splashing and flow separation initially used in free-surface wave simulations by Dalrymple et al. [15], is smoothed particle hydrodynamics (SPH). SPH was originally created as a method to simulate non-axisymmetric astrophysics problems by Lucy, Gingold and Monaghan [16]. The method is based on a Lagrangian framework, but rather than using elements to represent objects, discrete particles compose the medium. The meshless approach does well at modeling objects with large deformations, such as fluids, but is computationally expensive. A way to avoid long computation times associated with SPH, that was first suggested by Monaghan [17] is to reduce the speed of sound within the particle medium. This essentially makes the particle representation an incompressible fluid. However, particle velocity must be closely monitored and should be below Mach 0.1 to maintain an accurate representation of the material properties.

Oger et al. [18] modeled wedge FSI using SPH with a speed of sound that was five percent of the actual value to for particle incompressibility. The numerical model was developed by

spatially varying particles with a dense resolution at the point of impact that gradually become coarser with distance. Local pressure estimation along the wedge boundary was developed by sampling numerous particles in the vicinity of the location of interest to calculate an effective mean pressure rather than the dependency on just one particle. The results of the study match well with those of Zhao et al.

Shao and Lo [19] developed an incompressible SPH code that was used by Shao [20] to model the two dimensional wedge water entry problem. Their code calculates pressure differently than the original SPH formulation by implicitly calculating pressure through the Poisson equation rather than explicitly through an equation of state. The results obtained matched previous solutions well, even with a coarse mesh.

Anghileri et al. [21] conducted experiments involving both triangular and semi-circular composite wedges. Comparing experimental pressures on the wedges to numerical analysis results representing water with SPH, they matched the maximum pressure transducer within 90%, but were unable to match lower pressures. The duration of the impact was also significantly under predicted in their analysis. Errors were attributed to a lack of SPH mesh refinement.

In an effort to reduce computation time using meshless particles with actual water properties, Shah [22] simulated wedge entry with a water bath combining SPH and Lagrangian elements. Comparing accelerations to those in experiments the tests proved to be reasonably accurate but consistently over-predicted accelerations of lower deadrise angles resulting in much higher impact forces. Shah was also unable to accurately capture the fluidic intricacies of the water.

2.2 Aircraft Water Landing Studies

The importance of understanding aircraft ditching was brought to the forefront during World War II. During the war, aircraft were pushed to their limit; many ran out of fuel, had mechanical issues, and/or were shot down by enemy fire. As a result, countless aircraft were forced to ditch. Due to lack of pilot knowledge of how to land in these situations and weak structural integrity of the plane, many aircraft and crew members were lost [23].

Experiments prior to the war had been conducted, but the replica models were not very accurate and tests were conducted on land-based planes as they were for seaplanes; by towing them through the water without accounting for the initial impact. These tests did give some insight

into the hydrodynamic behavior of the planes, but little understanding into the crashworthiness of the aircraft, which in turn has a large effect on hydrodynamics [24].

Realizing the need for in depth analysis of aircraft in ditching events, both the United States and Great Britain began ditching trials. The Royal Aircraft Establishment at Farnborough developed one of the first free-launching platforms in 1941. Model aircraft were accelerated down a rail by a large catapult and released just above a pool of water. The instrumentation was crude for measuring physical data, but cameras captured the aircraft's dynamics throughout the event [24]. The National Aviation Committee for Aeronautics (NACA) used a large 880 meter towing tank constructed in the 1920s to conduct experiments. Aircraft were accelerated through the tank slightly above the water then released when the proper velocity was met. The model aircraft built by the USA and GB were dynamically scaled, meaning not only were the proportions of the aircraft to scale, but also the mass, mass distribution, and strength of materials. This was in an effort to have the models match the behavior of full-size aircraft as close as possible.

Scaled models mean very little if they do not closely relate to the real structures. Intentional full-size aircraft crashes for experimental purposes are rare; not only are they very dangerous, but are also expensive and have been conducted only a handful of times ever. In 1946, NACA tested the correlation between a full-size ditching of an Army B-24 airplane and a $^1/_{16}$ scale model [25]. Aircraft attitude, displacement, and acceleration from both experiments was gathered through crude video analysis. Data from the dynamically scaled model showed a good correlation to that of the full-size ditching validating the ability of models to replicate the true event.

The first experiment of a ditching of a scaled large passenger aircraft was conducted by Fisher and Hoffman [26, 27]. Scaled models of a Douglas DC-4 and a DC-6 were ditched at several different configurations under varying seaway conditions. It was found that the aircraft experienced a lower deceleration with flaps extended with a high pitch angle of 12°. Seaway conditions factored into the impact damage only when the waves grew large and landing parallel to the waves reduced damage.

As aircraft evolved from propeller-driven engines to turbo-compressor jet engines, new experiments were conducted regarding ditching behavior. In 1955, ditching experiments on a scaled model of a Boeing 707 were conducted [28]. As with the DC-4 and DC-6 it was concluded that a nose up pitch angle of 12° was optimum resulting in about 5*g* impact force on the fuselage. The recommended ditching configuration for the B-707 was then extrapolated to many large

passenger aircraft with similar size and weight. In 1969, NASA and the Air Force decided it was necessary to conduct ditching tests on new aircraft that were much larger than the B-707. Scaled model testing of the C-5 military transport were conducted and once again the nose up landing attitude of about 7° was recommended [29].

As computational efficiency has improved, numerical models for aircraft ditching have been developed. Numerical analysis is less time consuming and expensive than experimental models and give a better insight into progressive damage. Earlier FSI ditching models relied on an Eulerian mesh formulation to model fluid properties. However, as FEA has advanced and computing power has increased, new ditching analyses using SPH have been found in the literature.

Montanes et. al [30] compared numerical models to small scale ditching experiments comparing overpressure and suction forces on the aircraft undercarriage. Zhang et al. [31] researched the suction forces through both a small scale experiment and numerical analysis. Both researchers found that suction force was critical in producing an accurate aircraft attitude-time history.

Francesconi et al. [32] investigated impact forces of water impact on a $[90/45/0/45]_s$ composite laminate, a typical layup of an aircraft skin panel. Multiple mesh representations of water were modeled with Lagrangian, Eulerian, SPH, and element free Galerkin mesh. All four models over-predicted the peak acceleration, with the Eulerian scheme matching experimental results the closest.

Climent et al. [3] conducted small-scale experiments on the US Coast Guard platform CN-235-300M to validate finite element simulations using meshless Lagrangian elements. The peak impact pressure from experimental results was over-predicted by the numerical analysis by over two times the amount. The resulting error in analysis was attributed to the necessity to incorporate suction forces to the undercarriage of the aircraft.

The simulation of a full-size aircraft water ditching was conducted by Chandra et. al. [33]. A meshless Lagrangian formulation was utilized to model water and a rigid representation of the aircraft. The acceleration time history produced expected results, with a peak acceleration occurring with the impact of the wings. Without an experiment to validate against, the numerical results are inconclusive.

Toso [34] investigated aircraft ditching using the explicit finite element package Pam-Crash. She conducted simulations of a very basic aircraft model ditched into water represented by meshed

and meshless Lagrangian elements. Numerical analysis results of aircraft attitude, velocity and acceleration were compared to experimental results. It was observed that finer mesh resolution of the water and the addition of suction forces correlate well to experimental measurements. It was also suggested that the water bath be twice the size of the structure at impact.

2.2.1 Full-Size Aircraft Experiments

There have only been two experiments in which large commercial jet aircraft have been intentionally crashed. In both cases the aircraft was impacted onto a soft soil rather than water. The desire, but inability to thoroughly conduct such large scale experiments, highlights the importance of numerical modeling in future aircraft testing. In 1984, the FAA and NASA conducted a soft soil ditching on a full-size Boeing 720 outfitted with instrumented crash test dummies and an experimental flame retardant fuel additive. The objective was to crash the plane in front of a set of cement pillions to shear off the wings, but leave the fuselage intact. This would create a fire in the wings and engines to test the flame retardant additive while crash data from the dummies was recorded.

Due to the difficulty in controlling a full-size aircraft remotely, the plane missed the targeted landing zone. With a high yaw angle, it crashed into the pillions and the entire aircraft exploded into flames. The results were inconclusive, with little data collected from the dummies and the fuel additive not implemented.

Figure 2.1: Soft soil impact of a Boeing 720 conducted by the FAA and NASA [35].

After the NASA experiment, full-size aircraft testing was considered too dangerous, too expensive, and too unpredictable. However, in 2012 a more successful experiment of a soft terrain impact was conducted by The Discovery Channel with a Boeing 727. This time a pilot flew the

aircraft to the impact zone and parachuted out of the plane before touchdown. The plane was then controlled remotely by another pilot in a chase plane to the ground. Again, due to the difficulty in controlling an 86,000 kg aircraft, the impact was not ideal. The vertical descent rate of 10.5 *m/s*, was four times the desired rate and the aircraft impacted slightly nose down with the forward landing gear hitting the ground first. This resulted in the cockpit section shearing off from the cabin and folding under the aircraft. However, this time there was minimal fire and relevant results from the instrumented structure and crash test dummies were gathered. The highest impact force of a deadly 12*g* was located in the first class section. The impact force reduced to 6*g* at the rear of the cabin, which is equivalent to a minor car accident. These forces however, are an effect of the initial impact location and the highest forces are not necessarily in the front of the plane.

The experiment also tested if the brace position that is recommend by airliners, is the safest position to assume in the event of a crash. Crash test dummies were positioned throughout the cabin with some in the brace position with their heads tucked on their lap while others were seated casually. The results show that the casual dummy sustained a severe head trauma caused by the head slamming into the back of the seat in front. The braced dummy did not sustain this injury, but did suffer a broken ankle as its leg was forced back under the chair structure. Depending on the manner in which the aircraft crashes, the brace position could be safer. In some circumstances after a crash, passengers must be alert and aware of the situation to exit the aircraft and/or help other passengers, while in others a quick escape is necessary. In most cases however, the researchers concluded that the brace position is the safest to avoid head injuries and reduce the possibility of being impacted by falling debris.

Figure 2.2: Soft soil impact of a Boeing 727 conducted by The Discovery Channel.

Overall, the experiment was successful with many results and findings that have never been captured before in actual emergency crash landings. However, the monumental amount of time and money required to conduct such an in-depth study is not possible for every aircraft. A numerical analysis simulation relieves the difficulties of conducting an experiment on such a grand scale and has the ability to capture larger amounts of data. The following section details several of the specific crashworthiness requirements that aircraft must meet to be certified for flight.

2.2.2 Aircraft Certification Regulations

Often in ditching emergencies, the achievable descent rate is higher than what is certified by aircraft manufactures. Specifically, Flight 1549 had a descent rate four times the maximum rate specified by Airbus [5]. The pilot in this case had limited use of the engines, while this is not ideal, it is much better than no use at all. More complex structural analysis is needed for soft terrain crashes for worst case scenarios where the aircraft is powerless. Under Title 14 of the Code of Federal Regulations (CFR), Federal Aviation Regulation (FAR) Part 25 addresses the Airworthiness Standards for Transport Aircraft and outlines behavior and response of aircraft during ditching. To meet certification requirements for ditching, the aircraft must comply with Section 25.801 which is summarized below:

(b) Each practicable design measure, compatible with the general characteristics of the airplane, must be taken to minimize the probability that in an emergency landing on water, the behavior of the airplane would cause immediate injury to the occupants or would make it impossible for them to escape.

(c) The probable behavior of the airplane in a water landing must be investigated by model tests or by comparison with airplanes of similar configuration for which the ditching characteristics are known. Scoops, flaps, projections, and any other factor likely to affect the hydrodynamic characteristics of the airplane, must be considered.

(d) It must be shown that, under reasonably probable water conditions, the flotation time and trim of the airplane will allow the occupants to leave the airplane and enter the liferafts required by §25.1415. If compliance with this provision is shown by buoyancy and trim computations, appropriate allowances must be made for probable structural damage and leakage.

In addition, the aircraft must also meet the conditions of Section 25.561 “Emergency Landing Conditions – General” with key points shortened below:

(b) The structure must be designed to give each occupant every reasonable chance of escaping serious injury in a minor crash landing when—

(3) The occupant experiences the following ultimate inertia forces acting separately relative to the surrounding structure:

(i) Upward, 3.0*g*

(ii) Forward, 9.0*g*

(iii) Sideward, 3.0*g* on the airframe; and 4.0*g* on the seats and their attachments.

(iv) Downward, 6.0*g*

(v) Rearward, 1.5*g*

The ditching regulations from FAR 25 will be used as a guideline for the experimental and numerical tests conducted in this research. Special attention will be paid to the ultimate acceleration forces calculated from the impact to remain below the regulation requirement.

Chapter 3. Theory

The multiphase physics incorporated in FSI will be developed in this chapter. First, the theory behind the numerical analysis that will be used in the ditching investigation, explicit FEA, will be discussed. This will be followed by the behavior and response of structural components and their implementation into the numerical code. Next, the development and formulation of FSI as it pertains to the fluid, along with the implementation into an FEA platform will be discussed. Lastly, Classical Lamination Theory of composite materials will be covered. This is the underlying theory in LS-Dyna for composite shell elements which will be used in the ditching analysis. The theory covered in this chapter will be the basis of the FEA ditching methodology developed in this research.

3.1 Finite Element Theory

Finite element analysis is a numerical method used to solve structural mechanics problems. FEA reduces a large, complex problem into multiple, simple problems that can be numerically solved. Finite element theory is developed from two energy methods, the principle of minimum potential energy and the principle of virtual work. These methods and how they relate to FEA will be briefly discussed. An in-depth derivation of these principles will not be done as it is the basis of many of books, but the basic development of the theory will be explained in this section.

Minimum potential energy states that a body will deform or displace to a position that will minimize work. This is defined by the total potential energy of the system, Π_p, is equal to the internal elastic strain energy, $\mathcal{U}$, plus the external work applied Ω. With an infinitesimal change in displacement, resulting in a stationary position, the resulting change in energy is zero (Equation 3.1). From here the equations of equilibrium for an element can be derived.

$$\delta\Pi_p = \delta(\mathcal{U} + \Omega) = 0 \tag{3.1}$$

The theory of virtual work is very similar to that of minimum potential energy. It states that the different displacement paths a particle can take will result in varying amount of work done by a force acting on the particle. The work of the force on the particle along a virtual displacement is

known as the virtual work. The relationship between internal and external virtual work is in Equation 3.2:

$$\int_V \delta\epsilon^T \sigma dV = \int_V \delta u^T F dV + \int_{S'} \delta u^T T dS \qquad 3.2$$

where u is the vector of displacements, T is a vector of distributed forces on section S' of the surface, and F is a vector of body forces. Evoking the principle of virtual work, the left hand side can be written as the change in elastic strain energy due to infinitesimal variations of displacement. The right hand side can be seen as the change of potential work energy when dealing with conservative forces and is negative due to work being performed on the system.

$$\delta\mathcal{U} = -\delta\Omega \qquad 3.3$$

It can be realized by comparing Equations 3.1 and 3.3 that when the two energy methods, the principle of minimum potential energy and principle of virtual work, are reduced, equate to the change in strain energy of the material to the work put into the system. Based on the displacement approach this equates to; the material stiffness matrix K of an element, multiplied by nodal displacement is equal to force F.

$$Ku = F \qquad 3.4$$

This is the fundamental elemental equilibrium equation from which stresses, strains, and displacement can be calculated for elements composing a structure.

3.1.1 Explicit Finite Elements

Using the foundation equations as a basis, finite elements can be solved both implicitly and explicitly. Solving finite elements explicitly is the method of choice for dynamic, non-linear, impact problems. An explicit simulation steps through time and assumes velocity and acceleration are constant during a time step and are then used to solve for the next step [36]. Unlike the implicit finite element method, each computationally inexpensive time step of the solution can be solved without iteration and convergence is not an issue. However, the solution is conditionally stable and to have a valid result the time step must be smaller than the critical time step [37]. The critical increment for the explicit method for structural dynamics is given by the length of the smallest element divided by the speed of sound through its prescribed material. This is developed so that vibrations in the smallest element are accounted for and to ensure that they do not unintentionally pass through the element.

The results calculated through any FEA are only capable of being as accurate as the mesh permits. Creating a model with the correct element type, element size, and mesh scheme is vital to building an accurate virtual simulation. FSI requires even more mesh detail as now the necessity to capture the highly deformable, nonlinear nature of water must be accounted for. There are two mesh techniques that will be used in this research; Lagrangian and meshless Lagrangian. The strength of each scheme is utilized to produce an overall sound methodology. The characteristics of each scheme will be analyzed in the following sections.

3.2 Physics of Structure Impact

In the development of FSI analyses a substantial amount of effort has been focused on the response of the fluid, as it is the more challenging aspect of the event and has large effect on the behavior of the structure. However, typically the goal of conducting FSI simulations is to analyze the response of the structure, not the fluid. In this section, the mechanics and vibrations of structural impacts will be discussed.

To analyze the impact of the structure through engineering vibrations, the structure's initial impact on the water can be thought in terms of an impulse event. The total vibration analysis of an aircraft during ditching would be quite extensive analytical undertaking as mass is distributed over the structure and the impact occurs onto a deformable medium. Thus, the need for FEA. However, if the problem is simplified to the initial moment of impact with the water when the undisturbed surface can be considered hard, the following equations could apply. The subsequent formulation is derived for a hard surface impact of a section of the aircraft.

The following analysis is developed based on the text Engineering Vibrations by Daniel Inman [38]. The equation of motion of a system with damping is expressed by:

$$M\ddot{\delta} + C\dot{\delta} + K\delta = F(t-\tau) \tag{3.5}$$

where M is mass, C is the damping coefficient, K is the stiffness of the system, δ is displacement, and F is force as a function of time t and impact time τ. The equation of motion governs the behavior of a system in terms of motion (displacement, velocity, acceleration) as a function of time. An impulse is a sudden, short-duration of force such as an impact. An arbitrary impulse can be represented by Figure 3.1.

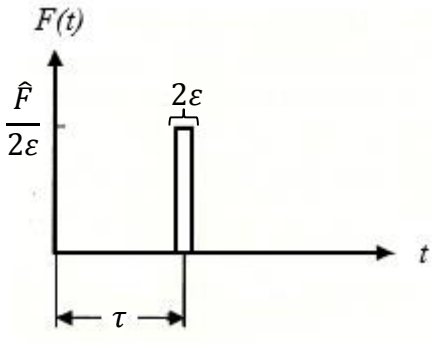

Figure 3.1: Sample impulse function [38].

Initially there is no force applied to the system, but at time τ a large and sudden force occurs. The plot is defined mathematically through the piecewise equation (an extension of the Dirac delta function):

$$F(t) = \begin{cases} 0 & t \leq \tau - \varepsilon \\ \dfrac{\hat{F}}{2\varepsilon} & \tau - \varepsilon < t < \tau + \varepsilon \\ 0 & t \geq tau + \varepsilon \end{cases} \tag{3.6}$$

where ε is a small number that is half the duration of the impact window. Calculating the area under the curve through integration, the intensity of the forcing function $F(t)$ can be defined in terms of $\hat{F}$ which is in terms of momentum, *Newtown ∗ second.*

$$\int_{-\infty}^{\infty} F(t-\tau)dt = \hat{F} \tag{3.7}$$

A solution can be obtained by relating the momentum of the system just prior to and right after the impulse. The change in momentum is equal to $\hat{F} = mv_0$; as the system is initially at rest and has no momentum prior to impact. Solving for the initial velocity and inserting it into the response function of an underdamped system, the response of the structure can now be solved as a function of time.

$$x(t) = \frac{\hat{F}e^{-\zeta\omega_n t}}{m\omega_d}\sin\omega_d t \tag{3.8}$$

As ditching progresses past the point of initial contact, the nature of the impact evolves and a hard impact can no longer be representative. Figure 3.2 is an illustration comparing the impact loads of a hard impact versus a soft impact. A hard impact, such as landing on a runway, has a small contact area which expands as specifically designed components of the structure fail and

absorb energy. In a soft impact, an encompassing pressure is produced onto the skin panels of the aircraft, reducing the ability of the structure components. The panels are not designed for this pressure and areas with high loads typically rupture. Ruptured panels create a high drag force in the water which results in a quicker deceleration of the aircraft.

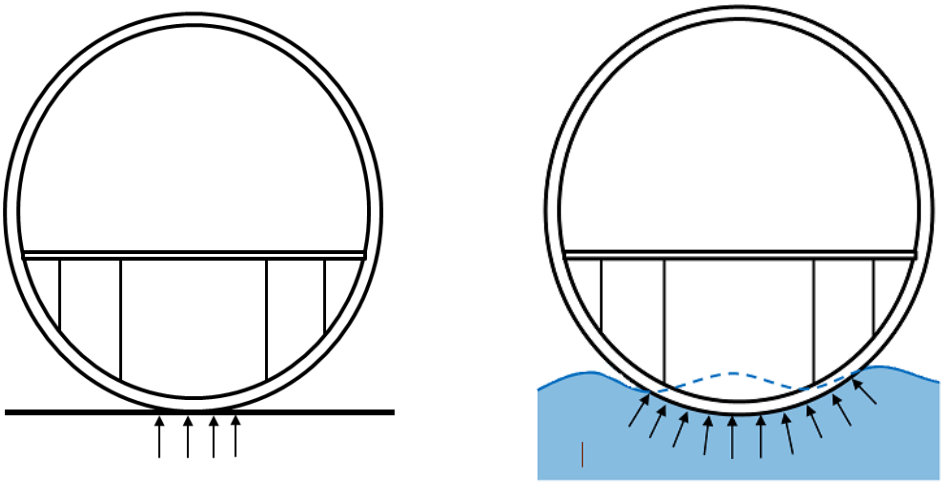

Figure 3.2: Comparison between a hard impact verse soft impact on an aircraft fuselage [39].

The structure is designed for a hard impact as it has energy absorbing components to reduce the force transferred to the passengers. To accurately model this effect, elements that represent the undercarriage must be able to capture bending caused by the pressure. To model these parts a Lagrangian mesh formulation is utilized.

3.2.1 Lagrangian Formulation

The Lagrangian mesh formulation discretely meshes a structure, assigning a fixed grid of nodes and elements to an object. Each element has a fixed mass associated with it and any deformation in the structure is a direct result of the displacement of the element's nodes and thus deformation of the element. This characteristic of the Lagrangian technique enables easy tracking of nodes as the computational domain moves with the particle velocities and no additional nodes outside the domain are required resulting in a very computationally efficient mesh scheme. Figure 3.3 is an example of contact between a ball and a plate, both modeled with a Lagrangian mesh. The deformation and resulting von Mises stress of the plate can be pictured in the elements. However, if elements are poorly formed with high aspect ratios or if large deformations occur, the determinate of the Jacobian matrix, which maps the coordinates between the current and reference configurations, will become inverted resulting in negative element volumes; reducing the

effectiveness of the mesh. To avoid hourglassing a Lagrangian mesh should be used for objects that experience little or no deformation.

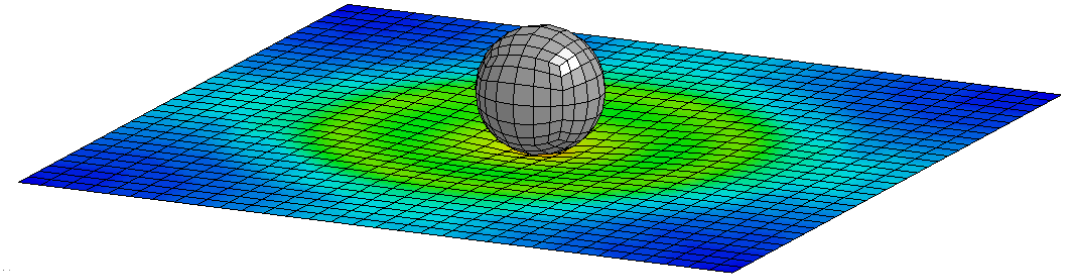

Figure 3.3: Impact of a rigid ball into a plate

Conservation of mass

$$\rho(X,t)J(X,t) = \rho_0(X) \tag{3.9}$$

The basic governing equations for the Lagrangian mesh formulation are written as partial derivatives (except for the conservation of mass, which is in written in terms of material coordinates) are as follows [25]:

Conservation of momentum

$$\frac{\partial \sigma_{ji}}{\partial x_j} + \rho b_i = \rho \frac{dv_i}{dt} \tag{3.10}$$

The variables are Cauchy stress σ_{ji}, body force b, and velocity v. The subscript i relates the coordinate directions.

Conservation of energy

From the first law of thermodynamics, the conservation of energy states that the total change in energy is equal to the added heat minus the work performed by the system, which translates to:

$$\rho \dot{w}^{int} = D_{ij}\sigma_{ji} - \frac{\partial q_i}{\partial x_i} + \rho c \tag{3.11}$$

Where $\dot{w}^{int}$ is rate of change of internal energy per unit mass, D_{ij} is rate-of-deformation, q_i is thermal conductivity, and s is a specific heat source term.

3.3 Physics of Water Impact

The earliest water impact theory and foundation of work since, was developed by von Karman to calculate the impact force on seaplane pontoons when landing on water. von Karman considers a wedge dropped with only a vertical velocity component into a calm horizontal water surface as shown in Figure 3.4.

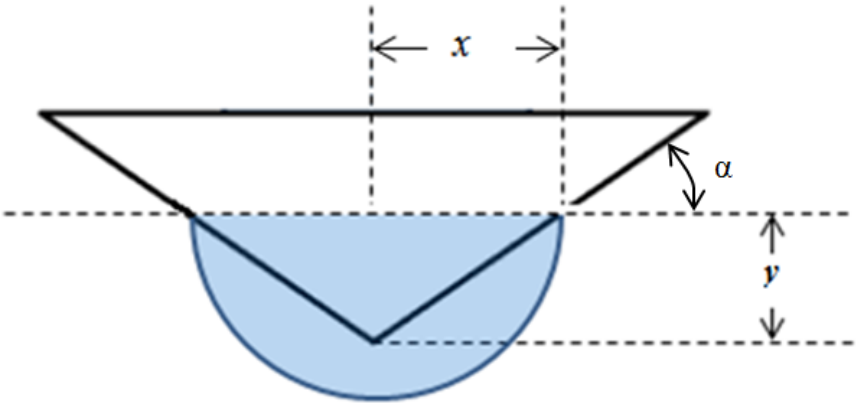

Figure 3.4: Wedge cross-section schematic analyzed by von Karman.

The dynamics of the wedge entering the water are broken down by relating the mass of the wedge M_i to the equivalent mass of the displaced water m through the momentum equation (Equation 3.12) where v_o is the initial velocity at impact and v is the downward velocity of the wedge [7].

$$M_i v_o = (M_i + m)v \tag{3.12}$$

The mass of water is approximated by calculating the mass of water (per unit length) in a semicylinder depicted as the shaded blue area in Figure 3.4 and calculated in Equation 3.13. The radius of the semicylinder is equal to the horizontal distance, x, from the wedge tip to the free surface of the water and can also be calculated in terms of penetration depth y through dead rise angle α.

$$m = \frac{\pi \rho l x^2}{2} = \frac{\pi \rho l (y \cot \alpha)^2}{2} \tag{3.13}$$

Solving for v which can defined as $\frac{dy}{dt}$ as only a vertical wedge velocity component of velocity is assumed. The velocity is equal to:

$$\frac{dy}{dt} = \frac{v_o}{1 + \frac{\rho\pi l x^2}{2M_i}} \tag{3.14}$$

Taking the derivative of this velocity and through Newton's second law of motion, the impact force F as a function of the wetted horizontal distance x is obtained.

$$F = \frac{{v_o}^2 \rho\pi l x \cot\alpha}{\left(1 + \frac{\rho\pi x x^2}{2M_i}\right)^3} \tag{3.15}$$

To calculate pressure, von Karman simply divided the impact force by the area of the wetted surface of the wedge. This results in an average pressure calculation across the face of the wedge.

In an effort to calculate the pressure distribution along the wetted surface of the wedge, Wagner built upon the work of von Karman. Rather than equating the virtual mass of water to a semicylinder with a diameter defined by the free surface of the water (Figure 3.4), he considered the displaced water rising along the edge of the wedge (Figure 3.5).

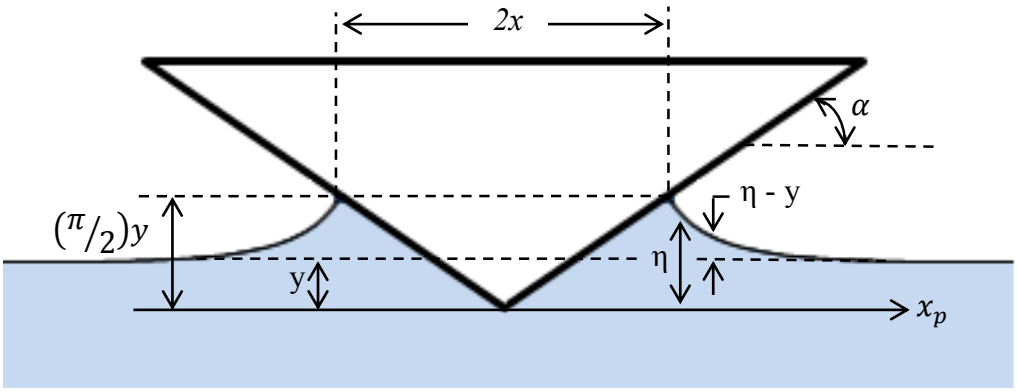

Figure 3.5: Wedge cross-section schematic analyzed by Wagner.

By assuming that the particles on the generated wave move only in the vertical y-direction, Wagner stated that the flow given by these boundary conditions was in close agreement to that of a stationary flat plate in an infinite fluid flow. The normal flow velocity of that on a flat plate with $x_p > x$ can be approximated by [8]:

$$v_n = v\sqrt{1 - \frac{x^2}{{x_p}^2}} \tag{3.16}$$

The elevation η of any point on the free surface of the water can then be written as the integral of Equation 3.17:

$$\eta = \int_0^t v_n dt = \int_0^t \frac{v\, dt}{\sqrt{1 - \frac{x^2}{{x_p}^2}}} \tag{3.17}$$

Changing the independent variable from time *t,* to that of plate width *x,* Equation 3.17 is now:

$$\eta = \int_{t=0}^{t} \frac{v\left(\frac{dt}{dx}\right) dx}{\sqrt{1 - \frac{x^2}{{x_p}^2}}} = \int_{x=0}^{x \le x_p} \frac{u(x) dx}{\sqrt{1 - \frac{x^2}{{x_p}^2}}} \tag{3.18}$$

noting that:

$$u(x) = v(t) \frac{dt(x)}{dx} \tag{3.19}$$

Once the water particle reaches the surface of the plate, $x = x_p$ and the elevation η is now equal to the contour of the impactor η_b, resulting in:

$$\eta_b = \int_0^{x_p} \frac{u(x) dx}{\sqrt{1 - \frac{x^2}{{x_p}^2}}} \tag{3.20}$$

The parameter $u(x)$ is defined as a geometric quantity that only depends on $\eta_b(x_p)$ not on $v(t)$. Wagner states that the water particles will follow the contour of the impactor that is described by the polynomial equation:

$$\eta_b = \beta x_p + \beta_1 {x_p}^2 + \beta_2 {x_p}^3 + \beta_3 {x_p}^4 + \ldots \tag{3.21}$$

Substituting Equation 3.21 into Equation 3.20 the solution for $u(x)$ is realized:

$$u(x) = \frac{2}{\pi}\beta + \beta_1 x + \frac{4}{\pi}\beta_2 x^2 + \frac{3}{2\pi}\beta_3 x^3 + \frac{16}{3\pi}\beta_4 x^4 + \ldots \tag{3.22}$$

A solution can now be calculated if v_n is given as a function of time, by calculating $x = x(t)$ from Equation 3.19 through the use of separation of variables.

Performing this derivation for a triangular shaped wedge with deadrise angle α, results in the horizontal distance *x* from the tip of the wedge for the force calculation to be:

$$x = \frac{\pi}{2} \cot \alpha (\Delta y) \tag{3.23}$$

whereas with von Karman's formulation the length of the wetted side is equal to:

$$x = \cot \alpha (\Delta y) \tag{3.24}$$

This calculation is $\left(\frac{\pi}{2}\right)$ times greater than the von Karman formulation and for a triangular shaped wedge this results in $\left(\frac{\pi}{2}\right)^2$ times the impact force than von Karman.

$$F = \pi\left(\frac{\pi}{2\alpha} - 1\right)^2 \rho v_c y l \tag{3.25}$$

Wagner's formulation however, only accounted for wedges traveling at a constant velocity. For wedges with a variable velocity, Sydow bridged the work of von Karman and Wagner by replacing the virtual mass developed by Wagner into von Karman's equation. This added virtual mass results in a higher impact force than the von Karman formulation and is found to have a good correlation with experimental results. Sydow equates the hydrodynamic force of a constant velocity wedge (Equation 3.26) to the force equation developed by Wagner [9]. The first resulting in the first term equating to zero

$$F = m_w \frac{d}{dt} + v\frac{dm}{dt} \tag{3.26}$$

By setting *v* equal to $\frac{dy}{dt}$, and multiplying both sides by dt, a relationship between the virtual mass of the water m_w and penetration depth of the wedge *y,* is now obtained.

$$\int_0^{m_w} dm_w = \int_0^{y} \left[\pi\left(\frac{\pi}{2\alpha} - 1\right)^2 \rho y l\right] dy \tag{3.27}$$

Through integration, Eq. (15) can be easily integrated to calculate m_w.

$$m_w = \frac{\pi}{2}\left(\frac{\pi}{2\alpha} - 1\right)^2 \rho l y^2 \tag{3.28}$$

Substituting this virtual mass into the von Karman equation, a resulting force equation for a variable velocity wedge accounting for the pileup of fluid on the wetted surface is obtained.

$$F = \frac{{v_o}^2 \rho \pi l}{\left(1 + \frac{m_w}{M}\right)^3}\left(\frac{\pi}{2\alpha} - 1\right)^2 y \tag{3.29}$$

The impact force equations developed by von Karman, Wagner, and Sydow will serve respectively as a upper bound, lower bound, and accurate model for validating the numerical analysis results calculated in the following sections.

3.3.1 Smoothed Particle Hydrodynamics Formulation

Smoothed Particle Hydrodynamics (SPH) is a meshfree particle method based on a Lagrangian framework. SPH particles directly mesh a specimen, but instead of an element grid,

discrete particles replace the elements. This mesh formulation is specifically designed for materials that will occur large deformations, such as fluids. The condition before and after the impact of a ball into an SPH fluid bath is shown in Figure 3.6. There is large deformation of the fluid particles as the ball enters the water, ejecting particles in the form of splashing.

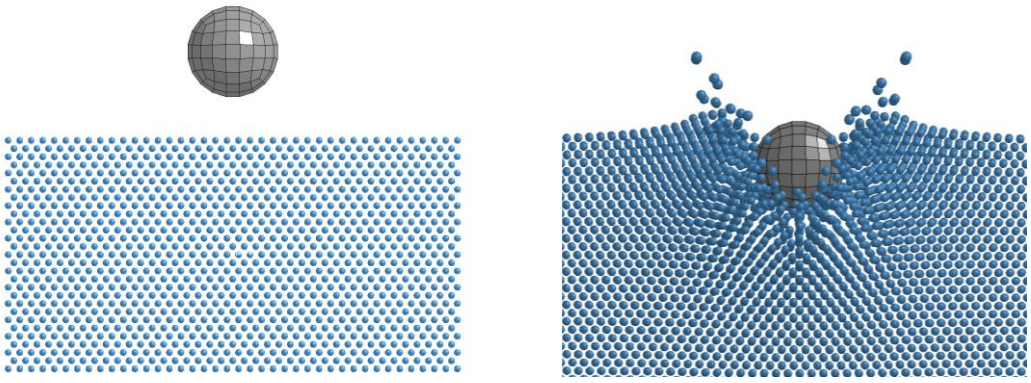

Figure 3.6: Rigid sphere impact into a SPH fluid bath.

The SPH formulation describes each particle's position, movement, and influence on other particles through a kernel function and particle approximation function. The kernel approximation is an integral representation of a field function within the integration domain Ω given by

$$f(x) = \int_{\Omega} f(x')W(x - x', h)dx' \tag{3.30}$$

where x is the position vector within the domain and x' is a dummy position variable, W is the smoothing kernel which is a peaked function with a smoothing length of h [40]. Particles interact through the assigned smoothing length which relates a sphere of influence for each point which governs the interaction between the neighboring particles, much like the interaction of poles on a magnet. In this study, a B-spline smoothing kernel is used with the highest influence at the center of the particle and decreasing with distance and is defined in Equation 3.31,

$$W(u,h) = \frac{C}{h} \times \begin{cases} 1 - \frac{3}{2}u^2 + \frac{3}{4}u^3 & 0 \le |u| \le 1 \\ \frac{1}{4}(2-u)^3 & 1 < |u| \le 2 \\ 0 & 2 < |u| < \infty \end{cases} \tag{3.31}$$

where C is a constant of normalization which can be controlled within the **Section_SPH* card and u is the distance between particle centers [41].

The discretization of the specimen into individual particles with associated mass and space is realized through particle approximation performed in the first step Equation 3.32, continued

from Equation 3.30. The infinitesimal volume dx' is replace by a finite volume ΔV_j, then through the definition of volume $\Delta V_j = \frac{m_j}{\rho_j}$ the discretized particle approximation can be replaced in terms of the mass and density of the particles in the support domain [40].

$$\begin{aligned} f(x) &\cong \sum_{j=1}^{N} f(x_j) W(x - x_j, h) \Delta V_j \\ &= \sum_{j=1}^{N} f(x_j) W(x - x_j, h) \frac{m_j}{\rho_j} \end{aligned} \tag{3.32}$$

The general particle approximation for field variable *x* can now be written in terms of a specific particle *i*.

$$f(x_i) = \sum_{j=1}^{N} f(x_j) W(x_i - x_j, h) \Delta V_j \tag{3.33}$$

This is graphically represented in Figure 3.7 with the smoothing length of particle x_i is represented on particle x_j. In a fully three dimensional model this smoothing length is revolved around the center of the particle in all dimensions.

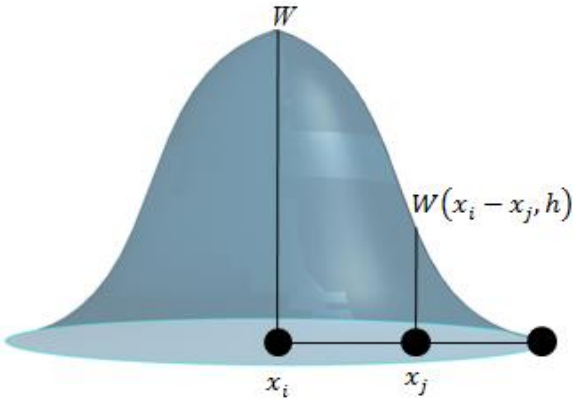

Figure 3.7: Representation of a B-spline smoothing kernel for particle x_i and influence on particle x_j.

The basic governing equations for SPH formulation are written as partial derivatives based on Lagrangian framework. Depending on the material that is being represented, different forms of these definitions are applied. In this research, SPH will only represent fluidic materials so the governing equations are written in fluid form of SPH. To represent a fluidic material LS-Dyna uses the weak form the governing equations as follows:

Conservation of mass

$$\frac{D\rho_i}{Dt} = \sum_{j=1}^{N} m_j {v_{ij}}^{\beta} \cdot \frac{\partial W_{ij}}{\partial {x_i}^{\beta}} \tag{3.34}$$

Conservation of momentum

$$\frac{Dv^{\alpha}}{Dt} = \sum_{j=1}^{N} m_j \left(\frac{{\sigma_i}^{\alpha\beta}}{\rho_i \rho_j} \cdot \frac{\partial W_{ij}}{\partial {x_i}^{\beta}} - \frac{{\sigma_j}^{\alpha\beta}}{\rho_i \rho_j} \cdot \frac{\partial W_{ji}}{\partial {x_j}^{\beta}} \right) \tag{3.35}$$

Conservation of energy

$$\frac{De_i}{Dt} = \frac{1}{2} \sum_{j=1}^{N} m_j \left(\frac{p_i}{{\rho_i}^2} + \frac{p_j}{{\rho_j}^2} \right) {v_{ij}}^{\beta} \cdot \frac{\partial W_{ij}}{\partial {x_i}^{\beta}} + \frac{\mu_i}{2\rho_i} {\varepsilon_i}^{\alpha\beta} {\varepsilon_i}^{\alpha\beta} \tag{3.36}$$

where α and β are the coordinate directions, i and j are references to respective particles i and j, ρ is the density, v is the velocity, e is the internal energy.

3.4 Composite Material Analysis

As the aircraft industry continues the push to create lighter, more fuel efficient planes, new materials are needed to replace aluminum and other lightweight metals which have been pushed to limit of their strength. The current generation of structures has begun to incorporate composite materials which are lighter and in some cases stronger than metals. These materials are also very appealing based on their ability to be tailored to suit specific properties needed in the design; such as a laminate that has a ply orientation that creates a high shear modulus. In order to create a methodology that will be applicable to current and future generations of aircraft, carbon fiber composite materials were implemented in the design. To compare and verify the results calculated through numerical analysis, Classical Lamination Theory (CLT) and composite failure theory were analytically calculated and compared to experimental test results.

3.4.1 Classical Lamination Theory

Carbon fiber composite materials are composed of plies of reinforcing graphite fiber within a polymer matrix that are bonded together to create a laminate. For enhanced strength, laminates are typically constructed from plies with different orientation angles. To calculate the stress within each ply of this heterogeneous material CLT can be applied. CLT is developed from three main

assumptions; smeared fiber and matrix properties (micromechanics), plane stress, and the Kirchhoff Hypothesis.

Each ply of carbon fiber is composed of thin graphite fibers inside an epoxy matrix. The fiber diameters are on the order of 5 μm with a ply thickness of approximately 0.324mm. The fibers give the laminate most of its strength with the matrix adding shear strength and protection of the fibers from the environment. Through micromechanics, the properties of these drastically different materials can smeared into effective engineering properties.

At the (macroscopic or microscopic) level, a composite ply can be represented by a representative volume element (RVE). A RVE captures the properties and phases of the material from which the properties of the entire ply will be extrapolated. Through the use of the RVE, specifically fiber volume fraction, V^f, effective properties are developed from strength of material models and elasticity solutions. Below is a table of calculated effective engineering properties and the model from which they are based.

Table 3-1: Engineering properties for a composite ply based on micromechanics models.

Effective Engineering Property	**Model**
$\boldsymbol{E_1 = {E_1}^f V^f + E^m(1 - V^f)}$	Rule of Mixtures
$\boldsymbol{\frac{1}{E_2} = \frac{1-\sqrt{V^f}}{E^m} + \frac{\sqrt{V^f}}{{E_2}^f\sqrt{V^f} + (1-\sqrt{V^f})E^m}}$	Improved Mechanics of Materials
$\boldsymbol{\nu_{12} = {\nu_{12}}^f V^f + \nu^m(1 - V^f)}$	Rule of Mixtures
$\boldsymbol{G_{12} = G^m\left[\frac{(G^m + {G_{12}}^f) - V^f(G^m - {G_{12}}^f)}{(G^m + {G_{12}}^f) + V^f(G^m - {G_{12}}^f)}\right]}$	Concentric Cylinders

Superscripts *f* and *m* specify the properties are related to the fiber or matrix while subscripts 1-2-3 are the principal material coordinate system corresponding to the longitudinal, transverse, and perpendicular directions. The orientation of these directions will change based on the ply layup within the laminate in the global coordinate system which will be denoted with x-y-z subscripts.

Once the effective properties of the plies are known, stresses and strains within each layer can then be calculated.

To calculate the stresses in a ply based on measured strains, the elastic compliance matrix is required. Since a composite material has three planes of symmetry and is therefore orthotropic, it is described by nine independent material constants C_{ij}.

$$\begin{Bmatrix} \sigma_1 \\ \sigma_2 \\ \sigma_3 \\ \tau_{23} \\ \tau_{13} \\ \tau_{12} \end{Bmatrix} = \begin{bmatrix} C_{11} & C_{12} & C_{13} & 0 & 0 & 0 \\ C_{12} & C_{22} & C_{23} & 0 & 0 & 0 \\ C_{13} & C_{13} & C_{33} & 0 & 0 & 0 \\ 0 & 0 & 0 & C_{44} & 0 & 0 \\ 0 & 0 & 0 & 0 & C_{55} & 0 \\ 0 & 0 & 0 & 0 & 0 & C_{66} \end{bmatrix} \begin{Bmatrix} \varepsilon_1 \\ \varepsilon_2 \\ \varepsilon_3 \\ \gamma_{23} \\ \gamma_{13} \\ \gamma_{12} \end{Bmatrix} \tag{3.37}$$

If the plane stress assumption is invoked, which requires one characteristic dimension to be much smaller than the other two; the stresses in the plane of the smallest dimension can be assumed to be zero. This simplifies a three dimensional state of stress into two dimensions, reducing the elastic compliance from a 6x6 matrix into a 3x3 reduced compliance matrix.

$$\begin{Bmatrix} \sigma_1 \\ \sigma_2 \\ \tau_{12} \end{Bmatrix} = \begin{bmatrix} Q_{11} & Q_{12} & 0 \\ Q_{12} & Q_{22} & 0 \\ 0 & 0 & Q_{66} \end{bmatrix} \begin{Bmatrix} \varepsilon_1 \\ \varepsilon_2 \\ \gamma_3 \end{Bmatrix} \tag{3.38}$$

To equate these local ply stresses into a global coordinate system where the overall behavior of the laminate can be evaluated, a transformation matrix needed. The transformation matrix is composed of simple trigonomic functions that perform rotations about the *z* axis since plane stress is considered.

$$[T] = \begin{bmatrix} \cos^2\theta & \sin^2\theta & 2\sin\theta\cos\theta \\ \sin^2\theta & \cos^2\theta & -2\sin\theta\cos\theta \\ -2\sin\theta\cos\theta & \sin\theta\cos\theta & \cos^2\theta - \sin^2\theta \end{bmatrix} \tag{3.39}$$

The transformation matrix is defined in terms of the global coordinate system, so to transform local stresses into the global stresses the inverse of the transformation matrix is required.

$$\begin{Bmatrix} \sigma_x \\ \sigma_y \\ \tau_{xy} \end{Bmatrix} = [T]^{-1} \begin{Bmatrix} \sigma_1 \\ \sigma_2 \\ \tau_{12} \end{Bmatrix} \tag{3.40}$$

The stress and strain states in a composite material can now be calculated, now plate theory and the Kirchhoff Hypothesis are needed to analyze a composite laminate subjected to various loading conditions.

The Kirchhoff Hypothesis, developed in the 1800's, is a simplified analysis to predict the response of a plate and is widely accepted in engineering. The hypothesis is based on geometry,

not material properties, and describes how layers within a plate deform when subjected to in-plane and out-of-plane forces and moments. Figure 3.8 illustrates different loading conditions that can be applied to a laminate.

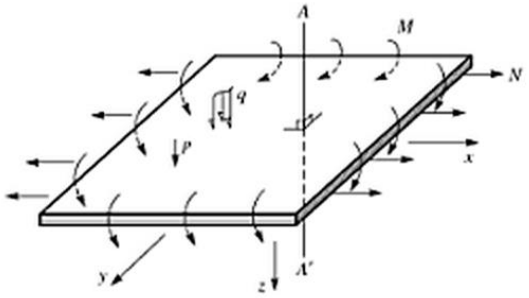

Figure 3.8: A laminate subjected to applied moments, M ; in-plane loads, N ; point load, p ; and distributed load, q [42].

To start the hypothesis, the laminate is defined around the center ply (or interface), labeled as the geometric midplane. The positive z-direction points downward and the laminate ranges in thickness from $-\frac{H}{2}$ to $\frac{H}{2}$ with the top (most negative z value) ply marked as layer 1. Each ply is assumed to be perfectly bonded to the layer above and below it and does not slip. As a result, strains across the thickness of the laminate are continuous while the stresses within the plies are often discontinuous due to different stiffnesses based on orientation angle. Figure 3.9a is a cross-section view of a four ply laminate in the x-z plane that is perpendicular to the midsurface and normal line A-A'.

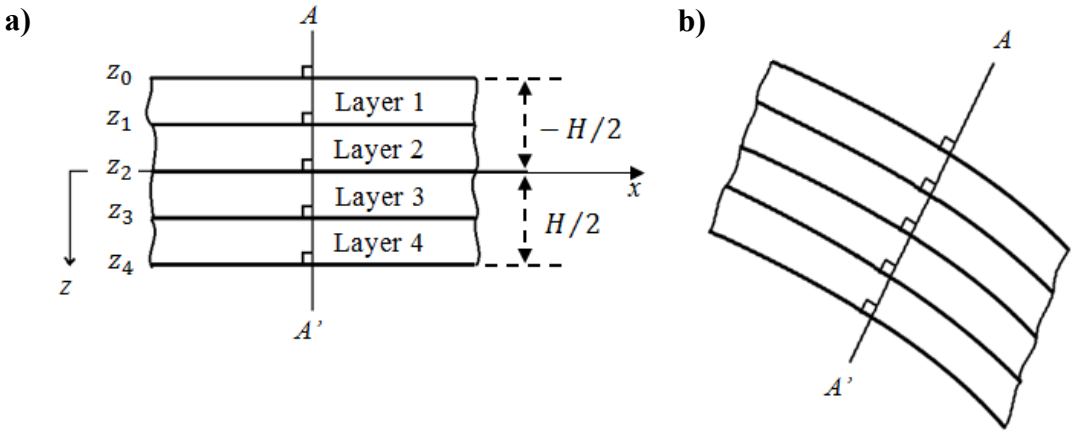

Figure 3.9: **a)** Unstressed composite laminate **b)** Deformed composite laminate with un-deformed normals.

With deformation of the laminate (Figure 3.9b), the normal line remains straight and perpendicular to each ply. Displacements and rotations of material points along A-A' are assumed to be small and strains and curvatures throughout the laminate can be expressed in terms of midplane values ε°, γ°, and κ°.

$$\begin{aligned} \varepsilon_x(x,y,z) &= \varepsilon_x^{\circ}(x,y) + z\kappa_x^{\circ}(x,y) \\ \varepsilon_y(x,y,z) &= \varepsilon_y^{\circ}(x,y) + z\kappa_y^{\circ}(x,y) \\ \gamma_{xy}(x,y,z) &= \gamma_{xy}^{\circ}(x,y) + z\kappa_{xy}^{\circ}(x,y) \end{aligned} \tag{3.41}$$

The relationship between mid-surface strains and curvatures can be related to force and moment resultants through the laminate stiffness matrix, commonly referred to as the ABD matrix. As a result of elastic coupling in composite laminates, in-plane responses are coupled to out-of-plane plane conditions. This can result in an in-plane load producing a curvature in the plate. By inverting the ABD matrix stresses and strains at any point within the composite can be calculated based on force and moment resultants. One point to note is that plane stress specifies that $\sigma_3 = 0$ while in Kirchhoff ε_3 is not assumed to be zero and thus σ_3 can be calculated. This is the inherent contradiction within CLT between the Kirchhoff and plane stress assumptions that must be accepted when performing this analysis.

$$\begin{Bmatrix} N_x \\ N_y \\ N_{xy} \\ M_x \\ M_y \\ M_{xy} \end{Bmatrix} = \begin{bmatrix} A_{11} & A_{12} & A_{16} & B_{11} & B_{12} & B_{16} \\ A_{12} & A_{22} & A_{26} & B_{12} & B_{22} & B_{26} \\ A_{16} & A_{26} & A_{66} & B_{16} & B_{26} & B_{66} \\ B_{11} & B_{12} & B_{16} & D_{11} & D_{12} & D_{16} \\ B_{12} & B_{22} & B_{26} & D_{12} & D_{22} & D_{26} \\ B_{16} & B_{26} & B_{66} & D_{16} & D_{26} & D_{66} \end{bmatrix} \begin{Bmatrix} \varepsilon_x^0 \\ \varepsilon_y^0 \\ \gamma_{xy}^0 \\ \mathrm{K}_x^0 \\ \mathrm{K}_y^0 \\ \mathrm{K}_{xy}^0 \end{Bmatrix} \tag{3.42}$$

where

$$A_{ij} = \sum_{k=1}^{4} \overline{Q}_{ij}(z_k - z_{k-1})$$

$$B_{ij} = \frac{1}{2} \sum_{k=1}^{4} \overline{Q}_{ij}({z_k}^2 - {z^2}_{k-1})$$

$$D_{ij} = \frac{1}{3} \sum_{k=1}^{4} \overline{Q}_{ij}({z_k}^3 - {z^3}_{k-1})$$

To simplify the analysis of the composite undercarriage used in experimental testing, a four ply $[0/90]_s$ layup was created. This ply orientation, classified as a symmetric cross-ply laminate, was carefully selected to produce an ABD matrix with B_{ij}, A_{16}, A_{26}, D_{16}, and D_{26} equal to zero.

This sparse matrix reduces out-of-plane elastic coupling properties and requires fewer calculations. By decoupling the response significantly, the laminate is orthotropic to both in-plane and bending behavior. Strains can be transformed from the global coordinate system into the local coordinate system to calculate the strains within each ply and check for failure.

3.4.2 Composite Failure Theory

An obstacle in using composite materials is analytically and numerically predicting failure. There is not universally agreed upon composite failure theory that is accurate for all ply orientations and loading conditions. There many failure mechanisms within composite materials which can result in three methods of failure: fiber breakage, matrix cracking, and ply delamination. These mechanisms along with temperature, moisture, and aging can affect the material by reducing its strength and/or inducing internal stresses.

One of the more common failure theories and the one studied in this work is the Tsai-Wu failure criterion. The Tsai-Wu criterion accounts for interactions between stresses in each orthotropic direction, similar to the von Mises criterion in yielding metals. The combination of stresses must sum to less than one for the theory to predict a stress condition of no failure within the material, written in Equation 3.43.

$$F_1\sigma_1 + F_2\sigma_2 + F_{11}\sigma_1^2 + F_{22}\sigma_2^2 + F_{66}\tau_{12}^2 - \sqrt{F_{11}F_{22}}\sigma_1\sigma_2 < 1 \qquad 3.43$$

Where F_i and F_{ij} are material constants based on maximum tension and compression strength in the longitudinal and transverse directions along with the maximum shear strength. It can be seen from this equation that individual stress terms interact with each other to determine when the material as a whole will fail. Due to its complexity, the Tsai-Wu failure theory can make it more difficult to determine specifically which mode was the cause of failure.

Chapter 4. Preliminary Studies

To insure the validity of the aircraft ditching numerical analysis, several fundamental studies were first conducted. By matching the results from smaller virtual simulations to physical experiments, validated FSI phenomena and material properties can be applied to the larger ditching simulation.

4.1 Fluid-Structure Interaction Behavior

To initially validate that a numerical analysis program was capable of capturing the physics necessary to model FSI, a thorough investigation of a rigid wedge impacting water was conducted. The goal of this study is to develop a numerical FSI analysis methodology that not only captures the dynamics of the wedge, but also the Newtonian characteristics of the fluid. Accurate behavior prediction of water is difficult due to the implementation of the Navier-Stokes equations within finite elements and the detailed mesh requirement to capture the extreme physical deformation. This study concentrates on the numerical analysis of water entry of rigid wedge specimens with deadrise angles of 20°, 30°, and 40° and compares qualitative results to physical experiments and quantitative results to analytical solutions.

Numerical analyses of basic rigid wedge models have been conducted previously. However, this study will be developed with accurate material properties of water along with the inherent compressibility of meshless particles in a commercial FEA code. Previous researchers have altered the speed of sound through the fluid to enforce incompressibility. For this to be valid, the Mach number of the fluid must remain less than 0.1 [17, 18]. With the difference in scale and velocities between the wedge and the aircraft, a selected speed of sound would not be valid for both problems. Therefore to develop a methodology that can be related to both problems, the material properties will not be changed.

4.2 Experimental Setup

The experimental results used for qualitative analysis were conducted by *Shah* [22]. In the test, wooden wedges with deadrise angles 20°, 30°, and 40° were dropped from an initial height of 150 *mm* into a tank of still water. The wedges were guided by a set of rails which controlled the angle of the wedge for a perpendicular impact. Each wedge weighed 1.639 *kg* and was 333 *mm* long impacting into the water tank with the dimensions 720 *mm* x 337 *mm* x 345 *mm*. This resulted in a near two dimensional flow field with two millimeters of gap between the ends of the wedge and the tank. The ends of the wedges were marked with points that were captured by a high speed camera recording at 500 frames/second. Through motion capture technology, the velocity of the wedges was calculated to be 1.281 *m/s* at initial impact. The results from this experiment will be used to qualitatively validate the numerical analysis of the same parameters.

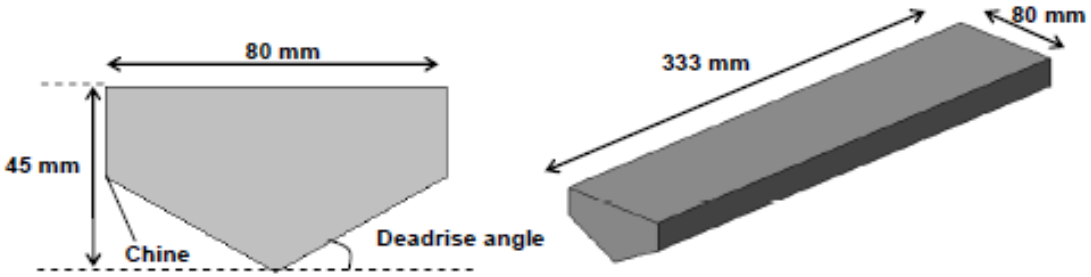

Figure 4.1: Dimensions of experimental wedges [22].

4.3 Modeling Approach

The construction of the experimental testing forced the water to exhibit mainly two dimensional flow characteristics. The geometry of the wedge also enables simplification as a result of symmetry. This allows for only half the wedge to be modeled, reducing the number of elements and in turn computation time. To make this analysis more relevant to the goal of modeling aircraft ditching though, the water entry problem will be developed in three dimensions. Two dimensional flow characteristics will be enforced, but the third dimension will be present. This adds to computation time, but is necessary to understand the element formulations and contact algorithms that will be used in the three dimensional aircraft simulations.

To capture the fluid behavior, including separation and wave generation, a coupled meshing technique was developed to render the intricate details. A mesh scheme composed of meshless

Lagrangian particles at the impact zone and Lagrangian elements away from the impact in less deformed areas. Mesh construction, material properties, along with many other input parameters were studied to develop the most accurate model. The properties, parameters, and geometry in the following section are an overview into the development of the model.

4.3.1 Material Properties and Parameters

To model water, the **Mat_Null* material keyword is used. This card is ideal for water as there is no shear stiffness associated for elements within this material card, while a pressure cutoff can be defined to allow for 'numerical' cavitation [43]. In conjunction, an equation of state (EOS) card which defines the thermodynamic state of a homogeneous material under different physical conditions must also be defined. The EOS relates two state variables such as density, temperature, volume, or internal energy to calculate pressure within the material domain. The most basic EOS to model pressure based on volumetric compression or expansion (density) of a material is a polynomial equation defined below:

$$p = C_0 + C_1\mu + C_2\mu^2 + C_3\mu^3 + (C_4 + C_5\mu + C_6\mu^2)E \tag{4.1}$$

where constants C_x are based on material properties and

$$\mu = \frac{\rho}{\rho_0} - 1 \tag{4.2}$$

is based on the density of water, ρ. With the C_1 coefficient set to the bulk modulus of the fluid and all other coefficients C_x equal to zero an EOS for water can be developed [44]. This card is created for low pressure, linear processes. For material models that are subjected to higher impact forces which will be seen in aircraft ditching, a more complex EOS is preferred. The Gruneisen EOS is capable of more complex calculations with a cubic shock velocity and particle velocity formulation. For compressed materials pressure is calculated by Equation 4.3 and expanded materials by Equation 4.4. [44]

$$p = \frac{\rho_0 C^2 \mu \left[1 + \left(1 - \frac{\gamma_0}{2}\right)\mu - \frac{a}{2}\mu^2\right]}{\left[1 - (S_1 - 1)\mu - S_2\frac{\mu^2}{\mu + 1} - S_3\frac{\mu^3}{(\mu + 1)^2}\right]^2} + (\gamma_0 + \alpha\mu)E \tag{4.3}$$

$$p = \rho_0 C^2 \mu + (\gamma_0 + a\mu)E \tag{4.4}$$

Where C is defined as the intercept of the $u_s - u_p$ curve, where u_s is the particle velocity behind the shock front and u_p is the shock velocity based on Huguenot shock data for water. S_x are the slope coefficients of the curve and γ_0 is the initial Gruneisen gamma. The initial energy term *E,* along with the correction factor of *a,* were both set to one, as the material is not under an initial load.

There is a wide array of values used for slope coefficients found in the literature. These values can have a large effect on calculated pressures, especially at high pressures. A brief study was conducted by compressing a single three dimensional solid element and changing EOS parameters based on those found in the literature (Table 4-1). Four nodes of the element were fixed, while the other four nodes were given a roller constraint and a prescribed displacement to force compression (Figure 4.2).

Table 4-1: Gruneisen EOS values found in the literature.

	C	S_1	S_2	S_3	γ_0
Kuroda et al.	1490	1.79	0	0	1.65
Hertel E.	1647	1.921	0	0	0.35
Liu et al.	1480	2.56	1.96	1.23	0.5
Tabiei A.	1647	1.92	-0.096	0	0.35
Webster K.	2417	1.41	0	0	0

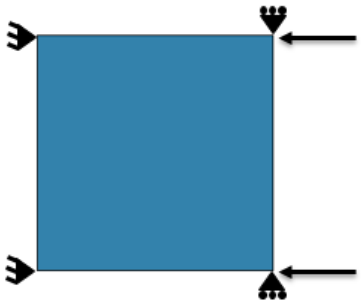

Figure 4.2: Two dimensional schematic of nodal constraints.

The results in Figure 4.3 show the effect of only changing the EOS can have on calculated pressure.

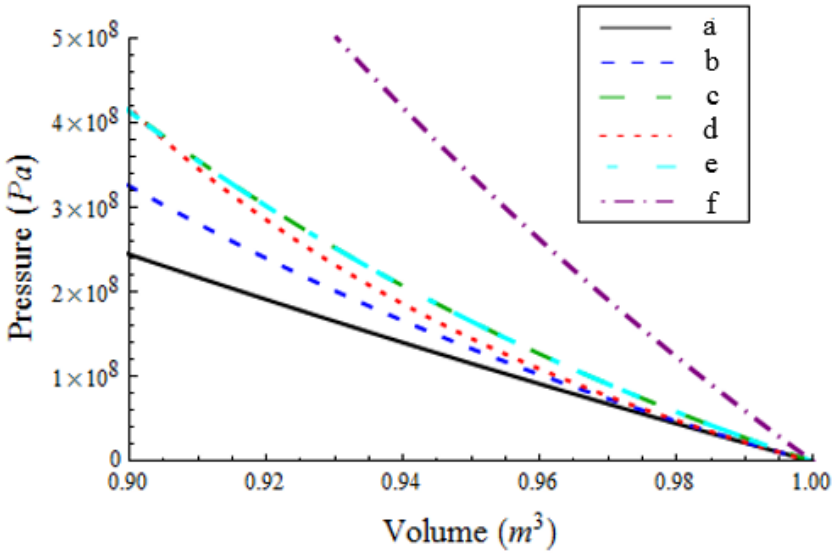

Figure 4.3: Comparison of EOS: a) Linear Polynomial; b) Kuroda et al. [45]; c) Hertel E. [46, 47]; d) Liu et al. [48]; e) Tabiei A. [49]; f) Webster K. [50].

The range of pressures due to compression is large between the Gruneisen values found in the literature. All four values of the Gruneisen EOS result in higher pressure than that of the Linear Polynomial EOS. This is expected as the linear polynomial EOS is recommended for low pressure processes and cannot capture the non-linear values at higher pressures. The Gruneisen parameters outlined by Webster clearly over-predict pressure compared to the other four Gruneisen EOS. While the results from Hertel and Tabiei are the only ones that correlate nicely, as the input parameters are very similar.

The maximum pressure of water in this research will be less than half the order of magnitude shown in Figure 4.3, approximately 10 *KPa*. At this range, the EOS give almost exactly the same resulting pressure profile. Therefore, further analysis will be conducted with the Gruneisen EOS with constants published by Hertel of Sandia National Labs and recommend by LS-Dyna Aerospace Working Group [47], a premiere LS-Dyna consortium. With the material properties and EOS of water selected, virtual simulations can now be conducted with confidence that low pressure water properties are modeled correctly.

To reduce computation time for structures that experience little to no deformation, the material card **Mat_rigid* is selected. This card will be used to model the wedge, which is made out of wood and does not distort when it impacts the water. Structures with this card are considered rigid bodies, thus stress and strain and other history variables are not stored, reducing computation

time. To ensure proper contact with the water, correct material properties are still required. Also to note, boundary conditions must be applied within the keyword using the *center of mass constraint option.* This is important in the wedge simulation, as the movement of the wedge in the experiment is constrained in all directions except for vertical displacement.

4.3.2 Initial Model Geometry

The preliminary model, built upon research conducted by Shah [22], starts where their work finished. Taking advantage of the symmetry of the problem, only half of the wedge and water body were modeled. In this initial model, the area of impact is developed with a constant particle spacing of 1*mm* in a square symmetrical grid pattern. The particle bath is contained by Lagrangian elements which represent the overall size of the fluid tank to ensure proper boundary conditions are accounted for in the simulation. By using a combination of meshless and meshed Lagrangian elements, computation time is reduced in areas of little interest, while maintaining a fine resolution at the impact zone.

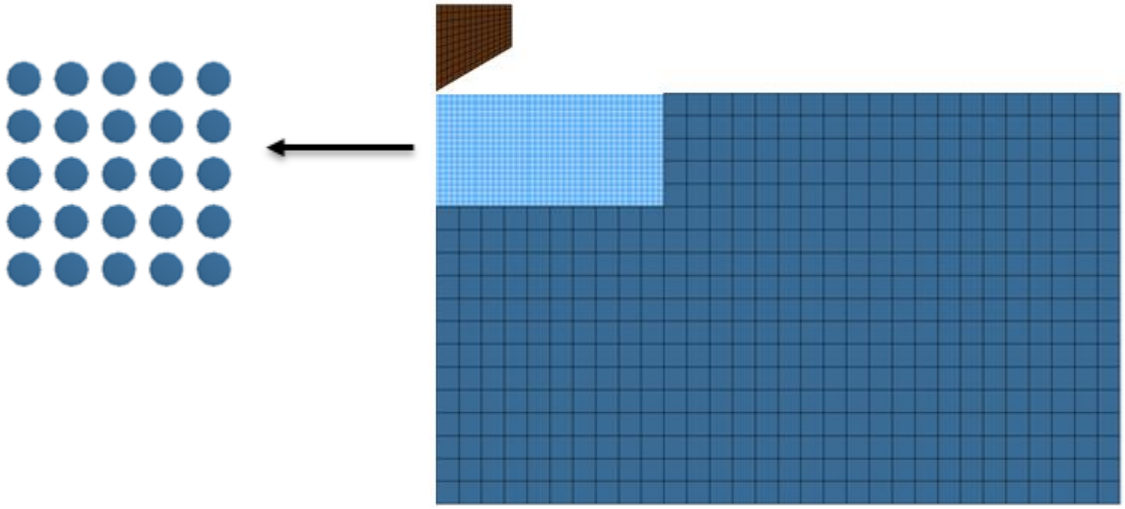

Figure 4.4: Initial model geometry setup.

To enforce boundary conditions on meshless particles, **Boundary_SPH_symmetry_plane* is utilized. Rather than applying boundary conditions straight to the particles, which can create numerical instabilities, this card creates an imaginary plane. The plane reflects forces of 'ghost particles' onto the particles in the model. These particles do not physically exist in the model, however to enforce the boundary, the ghost particles are computationally calculated to reflect an identical velocity, pressure, and density of each particle that is two smoothing lengths away from

the plane. The plane is initially located half a particle distance length away from the particle. Figure 4.5 is a schematic representing how the computer interprets a symmetry plane.

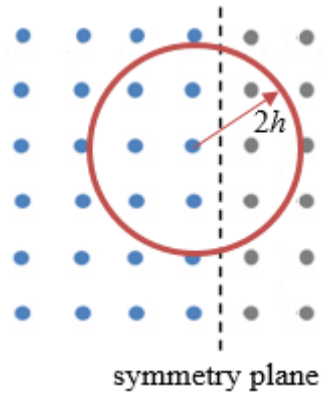

Figure 4.5: SPH symmetry plane representation with fluid particles (blue) and mirrored ghost particle (grey).

4.4 Comparison of Experiment vs. Initial Model Virtual Results

A direct comparison of numerical results at 10*ms*, 20*ms*, and 30*ms* after impact to the experimental tests are pictured in Figure 4.6. On the left side of the images are the results from the experimental testing conducted by Shah [22] compared to the results of the initial numerical analysis on the right. Qualitatively, several key physical fluid phenomena were not captured in these models:

- Splashing is nonexistent
- Generated wave is too large
- Rise of water free-surface is significantly over predicted
- Negative pressure gradient of the eject particles is not present

The more violent impact of the 20° wedge at 10 *ms* is not captured well, while the 30° and 40° appear to initially agree. This is due to the fact that more surface area strikes the water in a shorter amount of time when the 20° wedge impacts; forcing the water out as the pressure is too great for it to remain. This is seen in the experimental results, but numerically is not captured as only a small amount of fluid is leaked around the edge. As time progresses the 30° and 40° wedge models also begin to break down. Minimal splashing is created while an extreme rise in water level produces a wave that is much too large and well above the wedge. Physically a wave this large is not created within 30 *ms* of impact as the water does not have time to react to the impact therefore a pressure is released in the act of splashing occurs. The numerical model does not have the

refinement to eject fluid particles and alternatively the volume of water is moved more slowly in the form of a wave with an increased free-surface level.

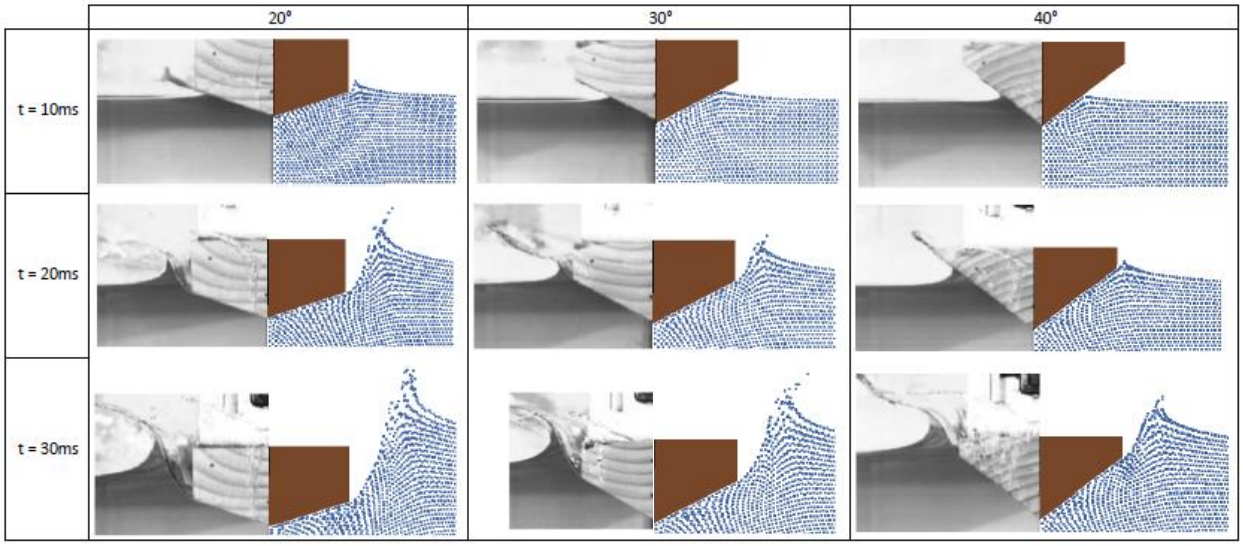

Figure 4.6: Initial numerical results compared to experimental results.

To ensure that the results were not affected by the width of the model, three different sizes were tested: 1*cm,* 2*cm,* and 4*cm.* All three tests were similar in that they lacked qualitative correlation to the physical experiments. The results were also compared quantitatively. The results showed no change in displacement, as all three models follow exactly the same displacement history (Figure 4.7). To reduce computation time, the 1*cm* thickness was used in subsequent analysis as fewer elements are needed, which reduces computation time and produces in the same characteristics as the larger models.

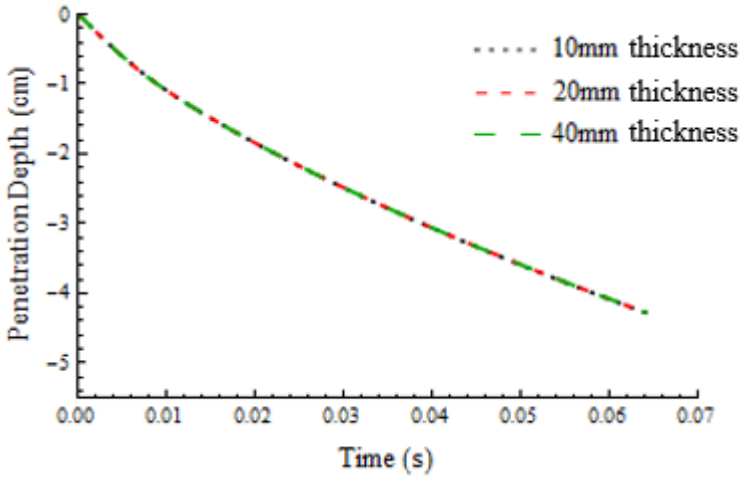

Figure 4.7: Displacement time history for different model thicknesses.

4.5 Advanced Mesh Scheme Geometry

To improve on the results produced by the initial mesh scheme, a model with finer meshless particle spacing was created. The mesh was refined to particle distance of 0.75*mm* over the volume of the SPH bath. This created 166,400 particles that must be individually tracked through the numerical analysis. Tracking this many particles was computationally expensive and resulted in a memory error due to bucket sorting. Bucket sorting is how the code discretizes the particle bath into separate contact volumes or boxes. The computer only calculates the smoothing kernel between particles within the same or neighboring bucket to reduce computation time. The idea is that a particle on one side of the bath will not contact or influence another particle on the other side, so the program will not perform the unnecessary calculation. A memory error resulting in bucket sorting clearly means that the computer has reached its maximum ability. To get around this, a new gradient mesh scheme was developed.

Two advanced gradient mesh schemes were developed: a vertical gradient mesh scheme (VGMS) and a horizontal gradient mesh scheme (HGMS). For each of these schemes, a mesh study was conducted to evaluate if the overall size of the section of dense particles affected the results. A plot of the developed schemes is seen in Figure 4.8. Both schemes have the same particle spacing for the dense (0.75*mm*) and coarse (2.0 *mm*) sections however, the horizontal gradient has a dense section that is wider than the vertical. This was developed to assess the importance of the dense particle distribution relative to the corner of the wedge

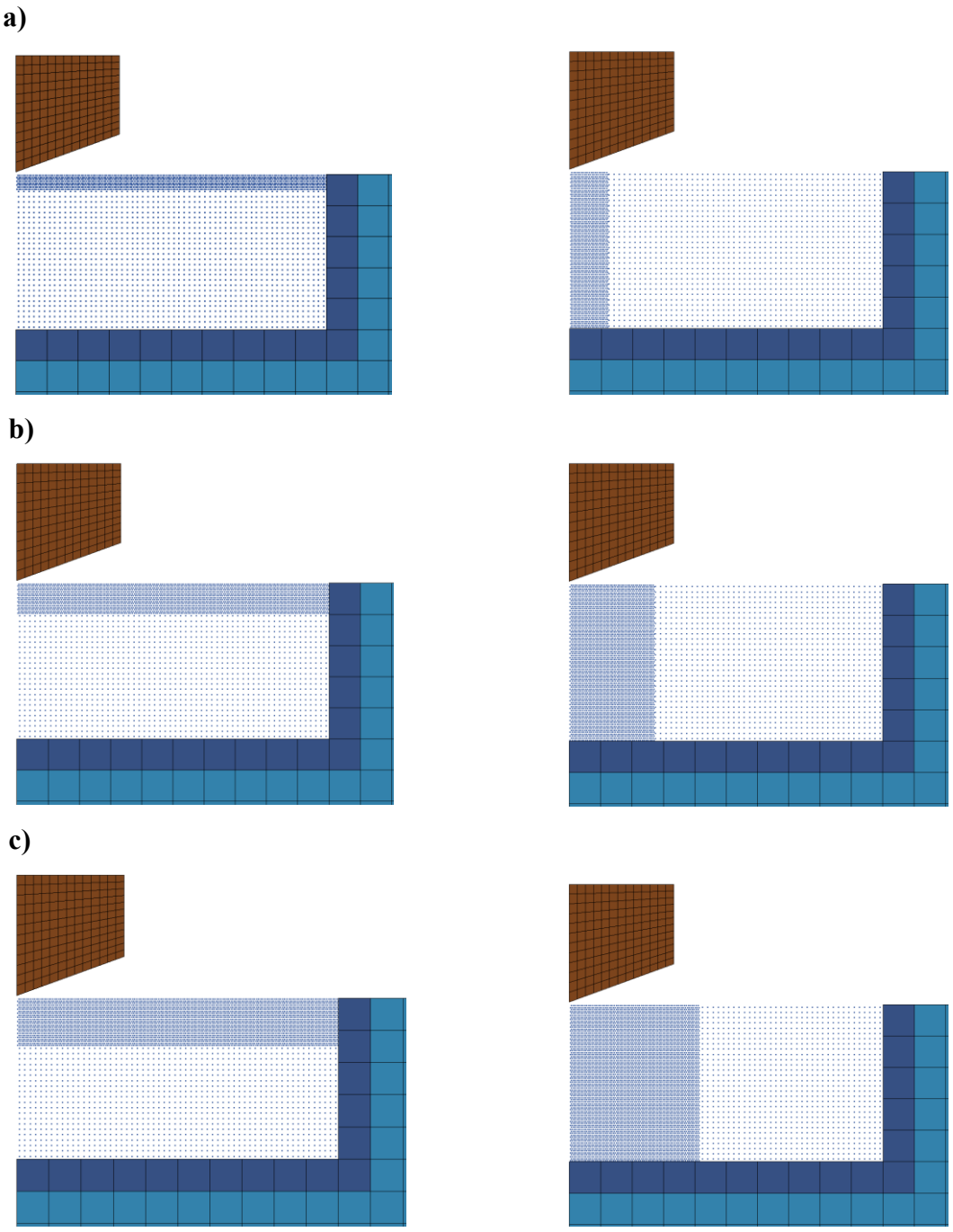

Figure 4.8: Particle distributions for the VGMS and HGMS for: **a)** 20°; **b)** 30°; **c)** 40° deadrise angles

Mesh refinement using SPH is a difficult process due to the necessity of maintaining a constant particle distance which is compounded in three dimensions. To reduce the amount of particles but maintain a refinement SPH gradient mesh schemes were developed. These

arrangements have a dense resolution in the area of impact and become coarser further away as seen in Figure 4.8. This takes advantage of the automatic contact definition within the SPH formulation as a contact keyword is not necessary between the different SPH parts. To avoid instabilities caused by an initial varying particle distance between the dense and coarse SPH layers, different section keywords were defined for each mesh. This provided improved mesh control and allowed the numerical analysis to initialize based on a consistent distance for each section, rather than using the same distance for the two different lengths. A smoothing length, *h(t)*, is calculated for each particle, which varies in time based on the divergence of the particle flow *div(v)* [44].

$$\frac{d}{dt}h(t) = h(t)div(v) \tag{4.5}$$

h(t) is calculated based on the initial particle distance between all particles, h_0, which is the maximum distance between two particles in the section.

$$H_{min}h_0 < h(t) < H_{max}h_0 \tag{4.6}$$

Within the numerical analysis platform, the smoothing length is then varied based on the concentration of particles to maintain the same number of particles in the neighborhood of each particle with H_{min} and H_{max} defaulting to 0.2 and 2. By defining two section cards to describe the respective mesh section, an initial distance h_0 is specified for each section based on the constant particle spacing within the section. The larger initial distance between coarse particles is not applied globally to the dense section allowing for particle interactions outside the intended smoothing length, which would artificially stiffen the water properties.

The orientation of the meshless particles was also modified. SPH particles are typically modeled in a square grid with one particle placed directly above and below the next as seen in 'Mesh 1' of Figure 4.9. This particle distribution is recommended over 'Mesh 2' which has a variation of distances between particles. An equal distribution of particles allows for the solver to start with a constant smoothing length for all particles, as the particles are spaced an equal distance apart with no variation. This scheme however is inherently unstable when modeling fluids, where particles are loosely couple together and able to move easily over one another. An advanced SPH meshing scheme has been developed to avoid this instability by correctly offsetting particles in a lattice configuration; Mesh 3 is a two dimensional view. The lattice retains equidistance between all particles in all three dimensions. This not only allows for better particle stability, but also

enables more particles to be placed in an area compared to ‘Mesh 1’ and allows particles to have a greater influence on out of plane particles.

Figure 4.9: SPH particle spacing.

A new meshing method was utilized which couples meshless Lagrangian and Lagrangian elements into a single ‘hybrid element.’ Hybrid element were placed at the interface between the two mesh schemes. Contact between SPH particles and other mesh types requires a contact definition, usually based on a penalty coupling method. This can add to computation time and inaccuracy as the shock must be extended in a ramp method to avoid instabilities. One way to avoid this is to create an SPH particle (or multiple particles if desired) inside of a Lagrangian solid element (Figure 4.10). This takes advantage of contact between all SPH particles which is, regardless of material type, automatic and accounted for within the SPH formulation. To utilize this, the first layer of Lagrangian solid elements that boarder the SPH bath is enabled with the hybrid SPH keyword. Contact between SPH and Lagrangian is now coupled through the transition zone where the hybrid element allowing forces to be easily transferred between the two element types.

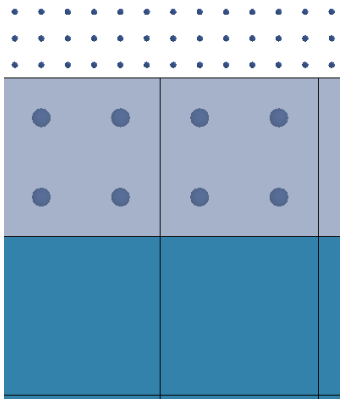

Figure 4.10: Zoomed in view of a hybrid element.

4.6 VGMS Results

The evolution of water impact has been studied by May [51] who researched the water entry of missiles. Through the study of small scale rigid spheres entering water, the response of the fluid was broken into six phases: shock-wave, flow-forming, open-cavity, closed-cavity, collapsing-cavity, and fully wetted. A brief investigation into the first three phases of fluid evolution for the M2 VGMS from Figure 4.15 will be conducted to evaluate the success of the mesh scheme. The wedge does not reach a depth where the wedge is completely enveloped by the water, so the later stages as defined by May are not captured. The results are magnified to present the development of fluid flow and the intricacies captured by the simulation.

As the wedge first contacts the water, the momentum of the relatively high velocity impactor generates a pressure wave through the stationary water. In a homogenous fluid, this results in radiating longitudinal pressure waves that are perpendicular to the direction of travel. The pressure profile is skewed based on the combination of a vertical velocity direction and the angle of the wedge face. The waves travel at the speed of sound through the medium which could not be accurately captured by past simulations that apply a speed of sound much smaller than the actual value. Fluid particles begin to rise along the side of the wedge as they are ejected from beneath the wedge and turned outward in the direction of the deadrise angle.

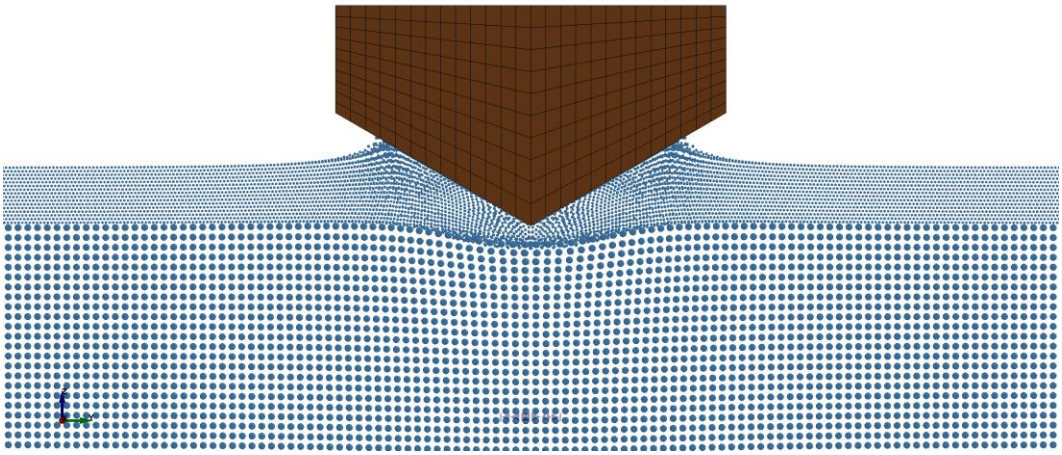

Figure 4.11: 30° wedge impact at 10 *ms*

The development of the wave is most destructive to the impactor. The wedge undergoes a large deceleration as the mass of the fluid must be displaced by the wedge, resulting in exertion of impact force. The simulation shows that a high pressure region within the fluid is produced, which

impinges water particles along the side of the wedge, separating them from the bulk of the fluid. Subsequently as the wedge continues to penetrate the water, a wave is developed. The characteristics of the wave are determined by the wedge deadrise angle. The smaller the deadrise angle, the more surface area strikes the water in a shorter time period. This causes a slamming effect, producing a large wave. Conversely, a large deadrise angle cuts through the water, creating a relatively smaller wave. Thus, the 30° wedge can generate a wave size that is between the size waves generated by the 20° and 40° wedges.

a)

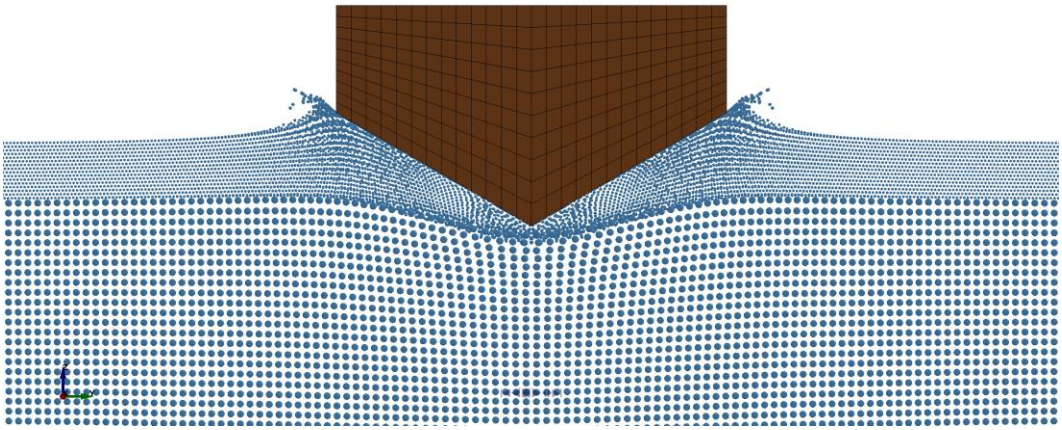

b)

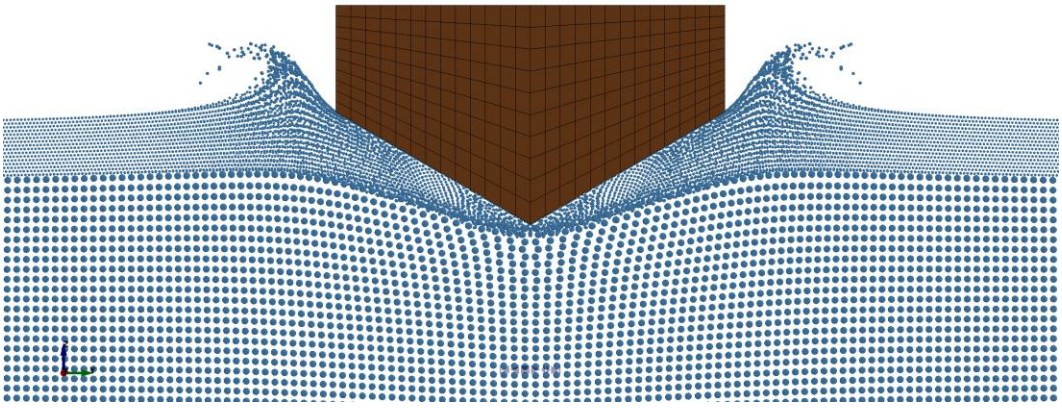

c)

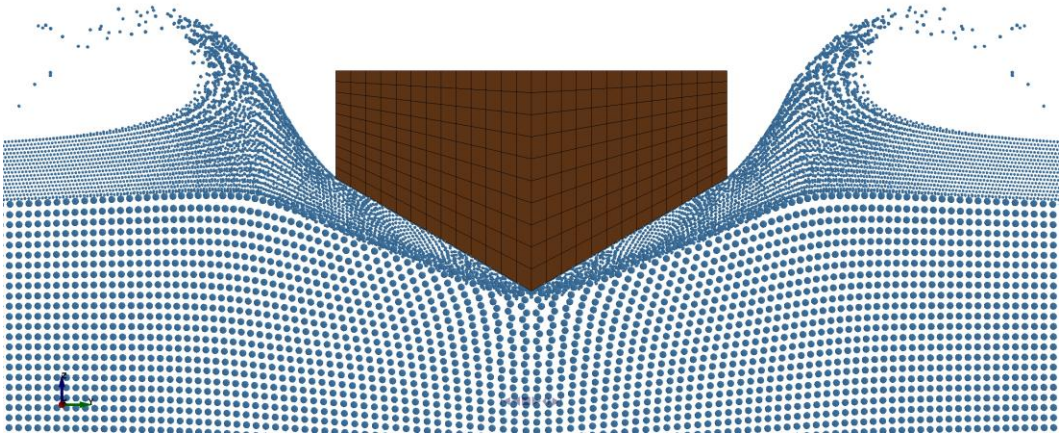

Figure 4.12: 30° wedge impact at: **a)** 15*ms* **b)** 20*ms* **c)** 30*ms*

The momentum of the impactor continues to push the wedge through the water. The flow field on the free surface of the water continues to developed and the wedge is said to be 'cavity running' as it displaces fluid particles that separate from the sides of the wedge, opening a tunnel to the water surface of the water. An early stage of open-cavity can be seen in Figure 4.13.

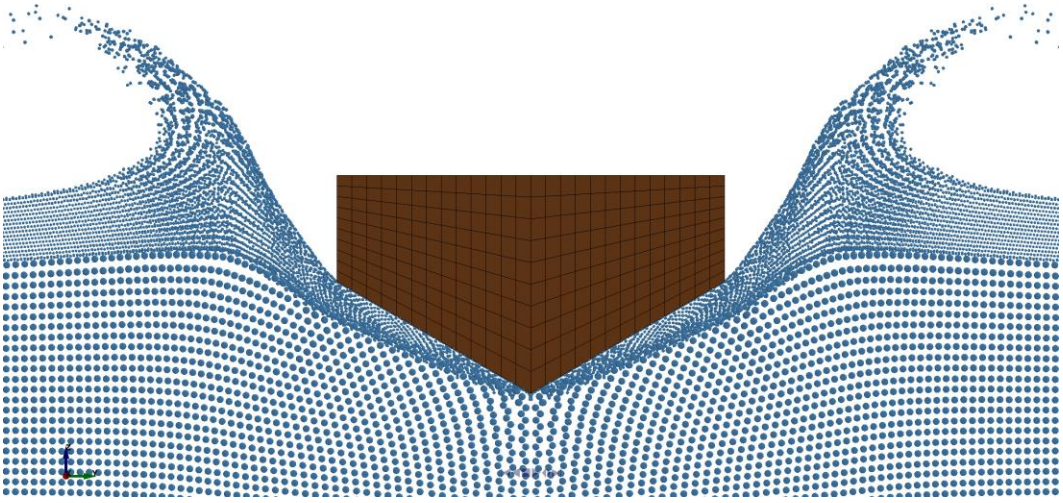

Figure 4.13: 30° wedge impact at 40 *ms*

The progressive qualitative results for each gradient mesh scheme at 10, 20, and 30 *ms* after impact for the remaining wedge angles are shown in Figure 4.14, Figure 4.15, and Figure 4.16. A strong correlation is achieved between the numerical analysis and experimental results. The physics that are absent or over predicted by the initial mesh scheme in Figure 4.6 are captured through the VGMS. Splashing is created as the impact pressure impinges on and ejects the particles

from beneath the wedge. The resulting mass of the fluid is then formed into a wave of similar shape and size to those found in the experiments, while the free surface away from the impact region remains unaffected. The only event that is not represented is the initial splashing due to impact of the 20° wedge. The jet of fluid that is expelled does not fully represent the developed fluid in the experiment. An incompressible fluid formulation might better represent the slamming effect generated by the small deadrise angles. However, the resulting flow characteristics of wave development and cavity opening are present as the wedge continues to penetrate the water.

Overall, there are very subtle differences between qualitative results of the M1, M2, and M3 mesh gradients. All three gradients show a similar splashing and flow development for each respective deadrise angle. However, based on penetration depth of the wedge, the dense gradient section should be varied by deadrise angles. Lower angles slam into the water and do not penetrate as deep, while larger angles cut through the fluid. The dense section should be extended so that the wedge does not penetrate through into the coarse section.

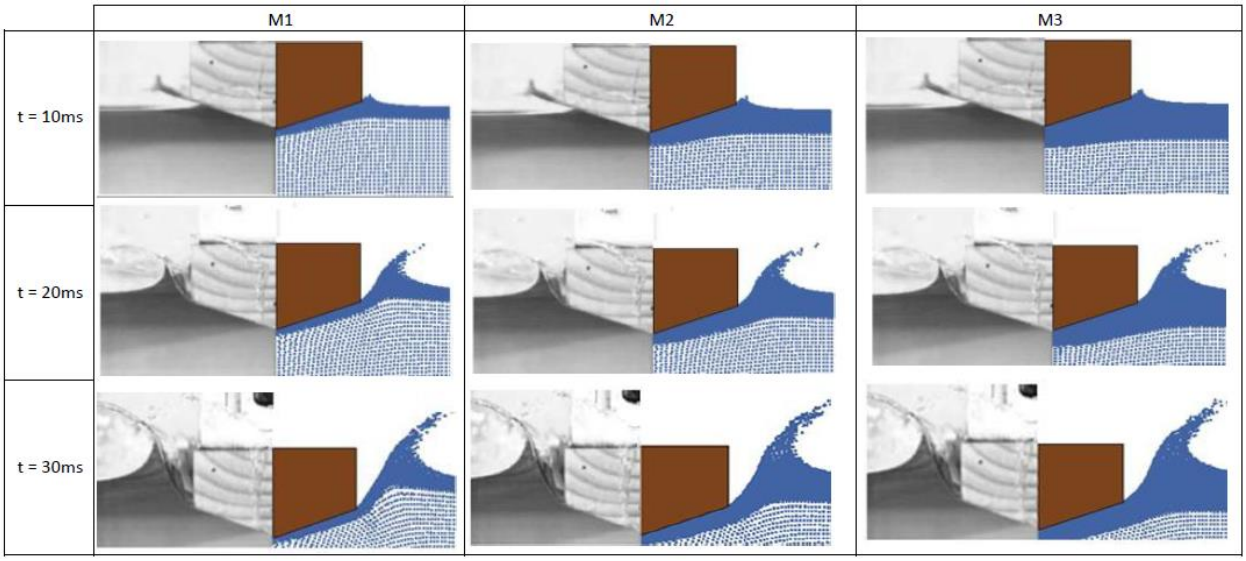

Figure 4.14: Comparison of results for the VGMS 20° deadrise wedge

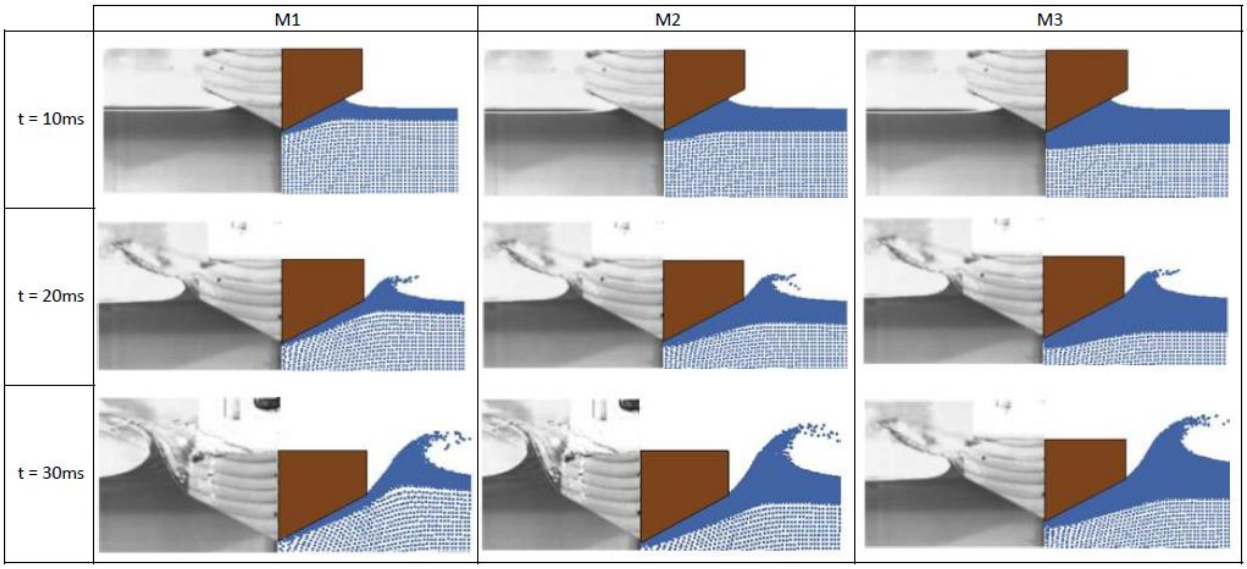

Figure 4.15: Comparison of results for the VGMS 30° deadrise wedge

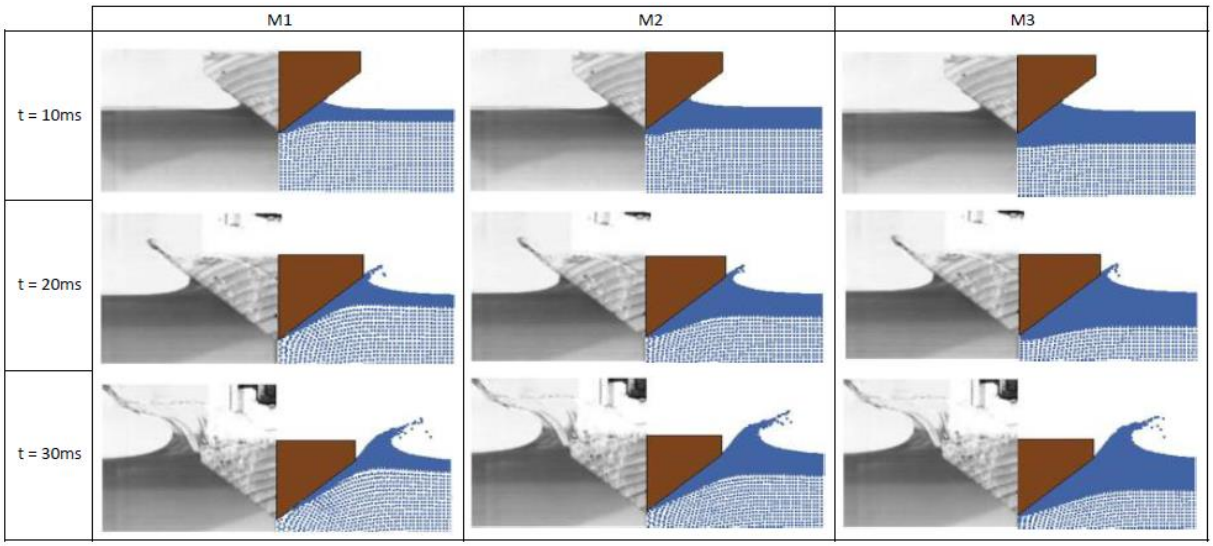

Figure 4.16: Comparison of results for the VGMS 40° deadrise wedge

The vertical displacement and force time histories for each wedge deadrise angle are shown in Figure 4.17, Figure 4.18, and Figure 4.19. The displacement of the wedge, based on the penetration depth of the wedge are compared to results predicted by von Karman. While forces have been normalized by the length of the wedge to allow for a better comparison to experiments with different wedge dimensions. A comparison of numerical results and analytical results predicted by Sydow are displayed. The results of the von Karman formulation are also shown to illustrate the error in this approximation.

As expected, the impact force varies based on the deadrise angle of the wedge. The slamming effect produced by the 20° wedge results in a much higher impact force than that of the 40° wedge, which cuts through the water. The 20° and 30° wedge simulations match the maximum impact force within six percent of Sydow. The 40° wedge impact force however is over predicted with about a twenty-five percent difference. This could be an effect of the depth of the particle section within the Lagrangian bath, as the 40° wedge penetrates deeper into the water. The force decay for all three wedge deadrise angles is over predicted. The force decay in the simulation also takes place much more rapidly than the analytical results. Actual quantitative results from physical experiments are needed to further assess the simulation data to decide the degree of accuracy compared to the analytical predictions.

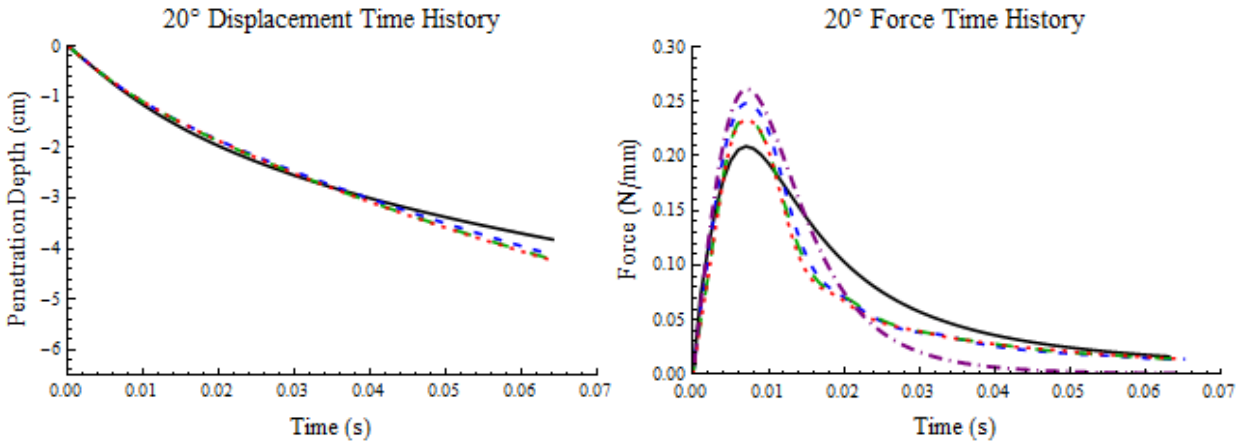

Figure 4.17: VGMS displacement and force time histories for the 20° deadrise angle wedge

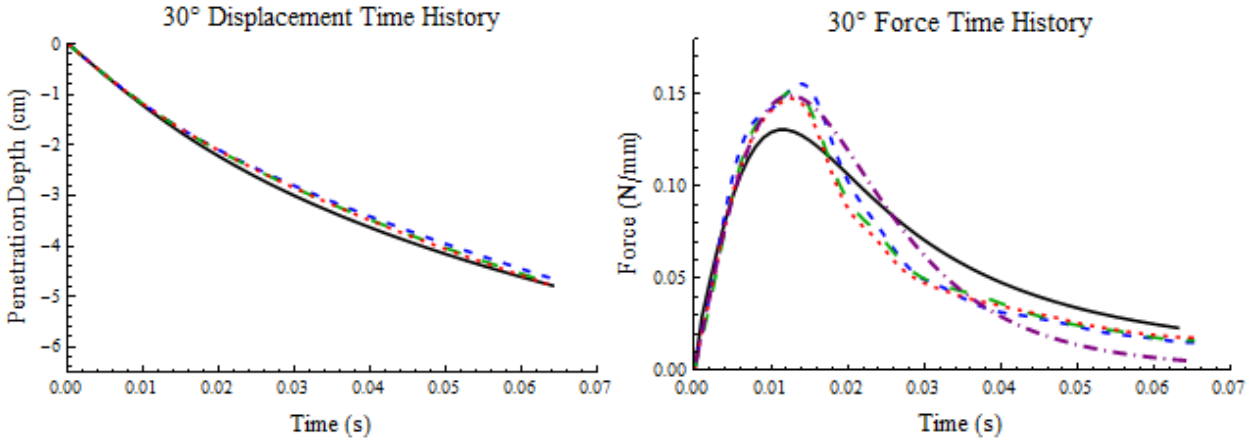

Figure 4.18: VGMS displacement and force time histories for the 30° deadrise angle wedge

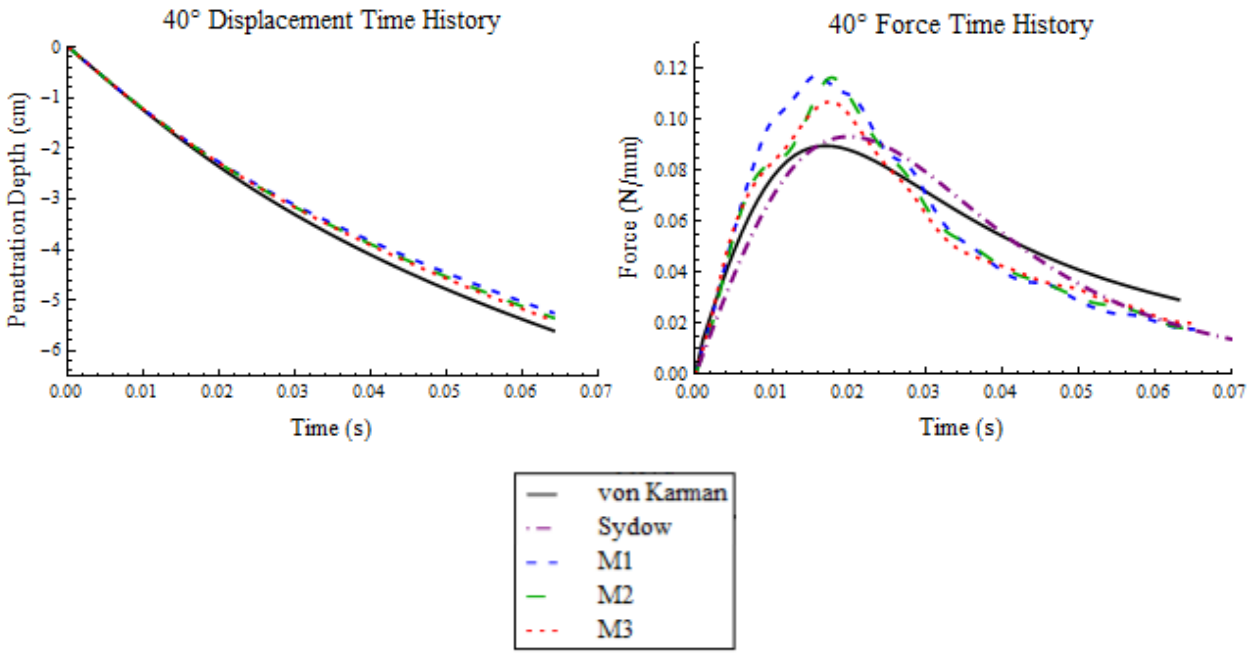

Figure 4.19: VGMS displacement and force time histories for the 40° deadrise angle wedge

4.7 HGMS Results

As with the HVMS, a strong correlation between qualitative numerical and experimental results is achieved. The results of the M3 HGMS are enlarged for a detailed look into the progression of the impact and to compare with the time history figures of the HVMS.

At initial impact, the water begins to rise along the edge of the wedge. The fluid forms into the shape that Wagner based his calculations on, detailed in Section 3.3.

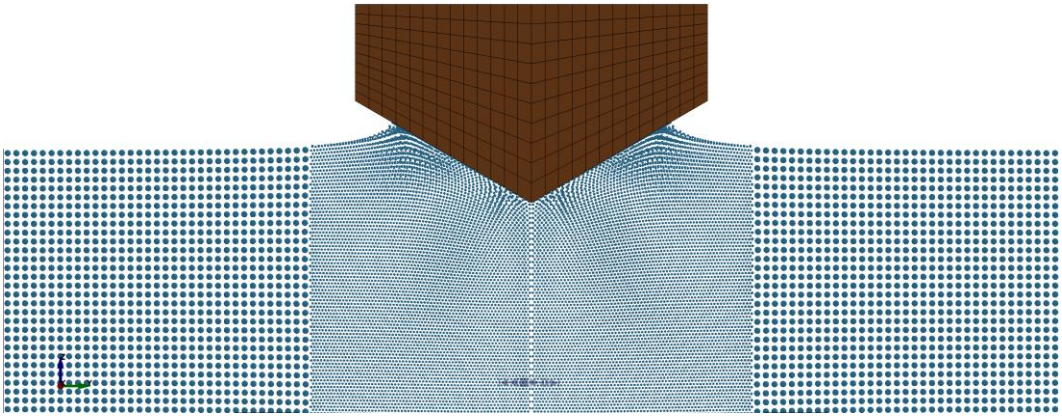

Figure 4.20: 30° wedge impact at 10 *ms*

As the wedge continues to move through the fluid, particles are ejected from beneath the wedge due to the high pressure developed from the impact. The creation of a wave can be seen in the time progressions of Figure 4.21. There appears to be a slight influence of the HGMS on the development of the wave as it moves from the dense resolution to the coarse. The coarser particles have more associated mass and therefore require more energy to be displaced. In Figure 4.21b the bottom of the wave is slightly distorted by the coarse particle resolution. By 30*ms* the particles have been displaced and form into the wave.

a)

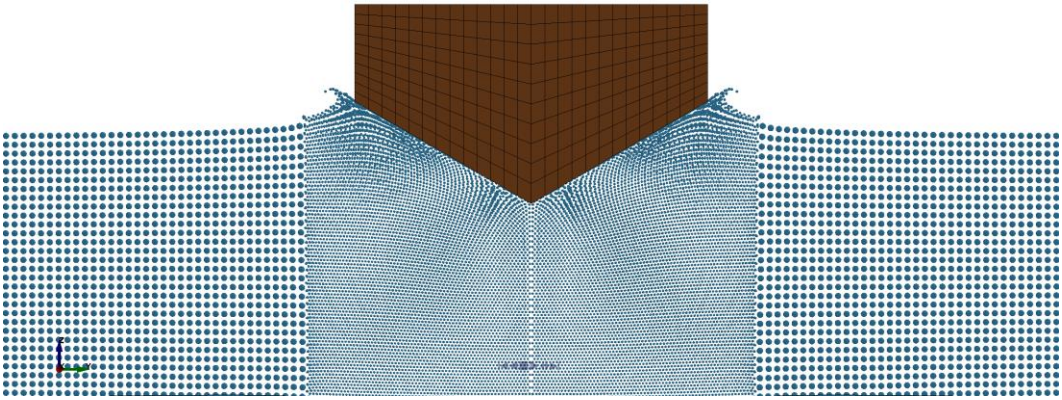

b)

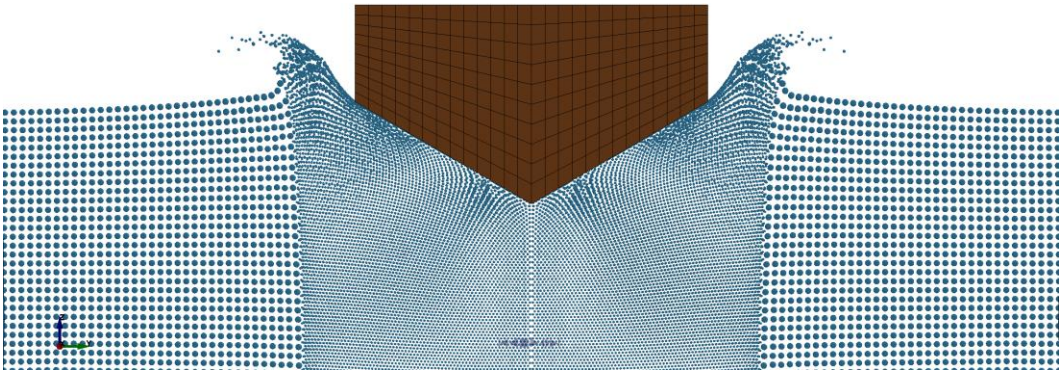

c)

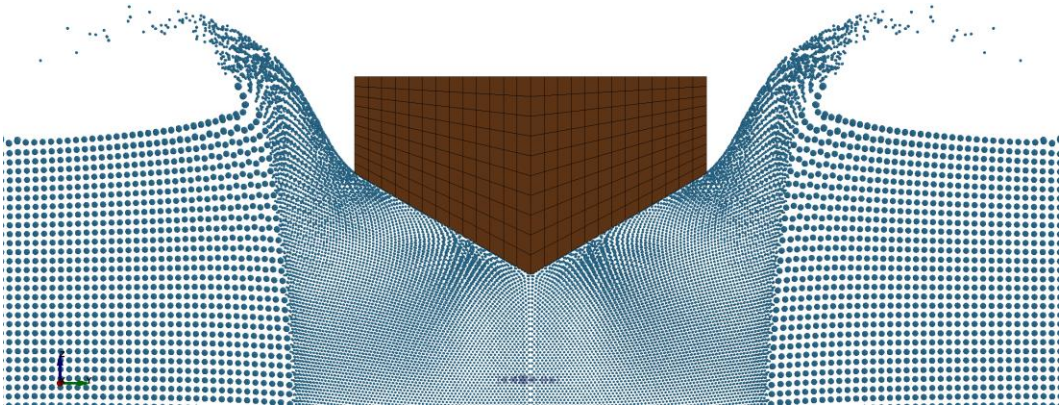

Figure 4.21: 30° wedge impact at: **a)** 15*ms* **b)** 20*ms* **c)** 30*ms*

The momentum of the impact continues to push the wedge through the water. The flow field on the free surface of the water evolves into a larger wave and as with the VGMS the wedge begins the initial moments of cavity running.

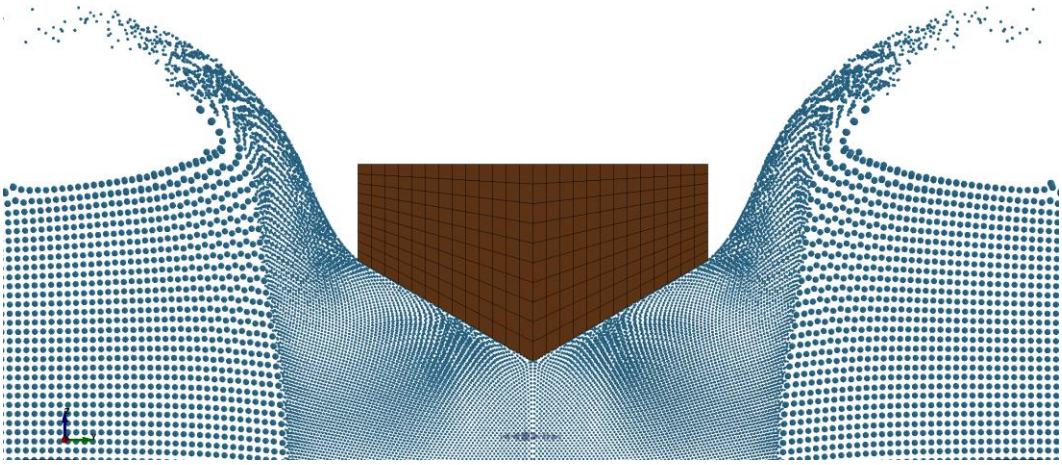

Figure 4.22: 30° wedge impact at 40 *ms*

Similar to the HVMS, the HGMS captures the fluid evolution and properties not found in the initial model. However, the HGMS does show several issues based on wedge deadrise angle and gradient horizontal thickness. There are several interesting characteristics to note when analyzing the results of the M1, M2, and M3 gradients for the 20° deadrise angle in Figure 4.23. The M1 gradient behaves very similar to that of the initial mesh scheme. The dense resolution does not extend far enough into the fluid bath to be utilized. While the dense mesh of the M2 gradient ends

right at the corner of the wedge. The particles are impinged out from the wedge, but the further development of the wave is clearly wrong.

The M1 HGMS for the 30° deadrise angle wedge resulted in numerical instabilities. After the first several time iterations a memory error resulted

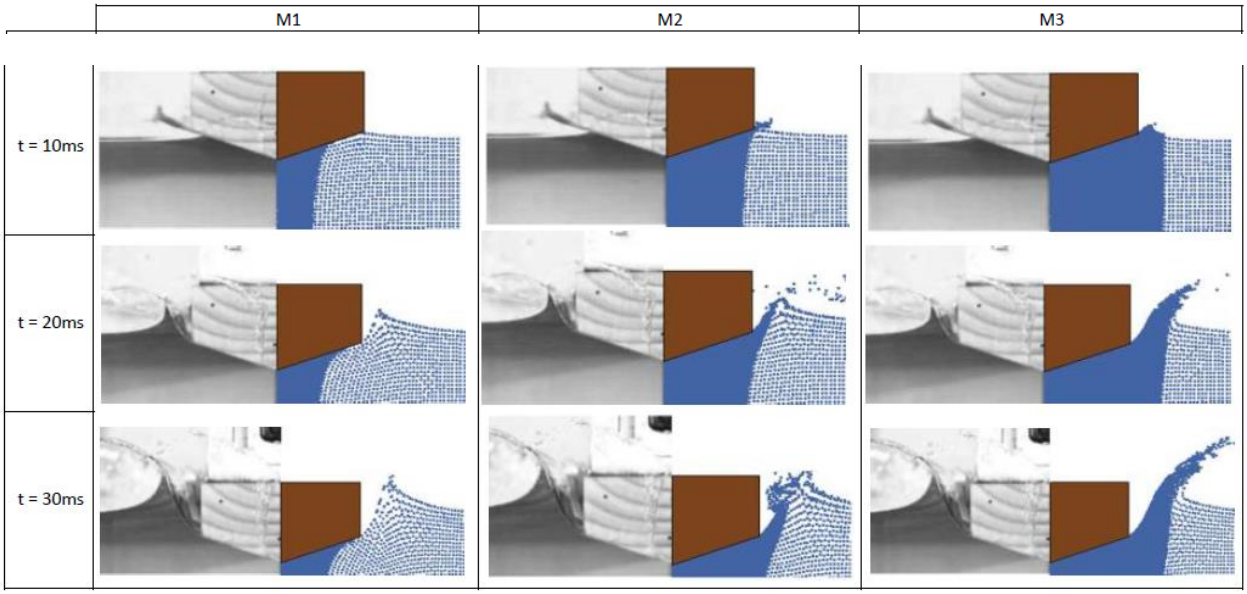

Figure 4.23: Comparison of results for the HGMS 20° deadrise wedge

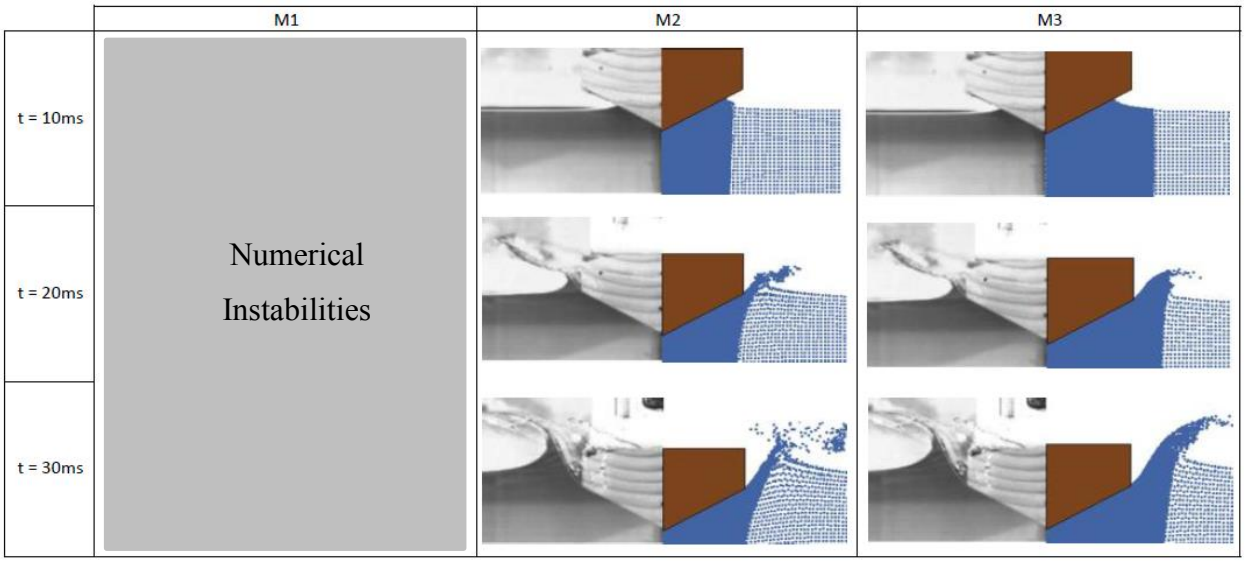

Figure 4.24: Comparison of results for the HGMS 30° deadrise wedge

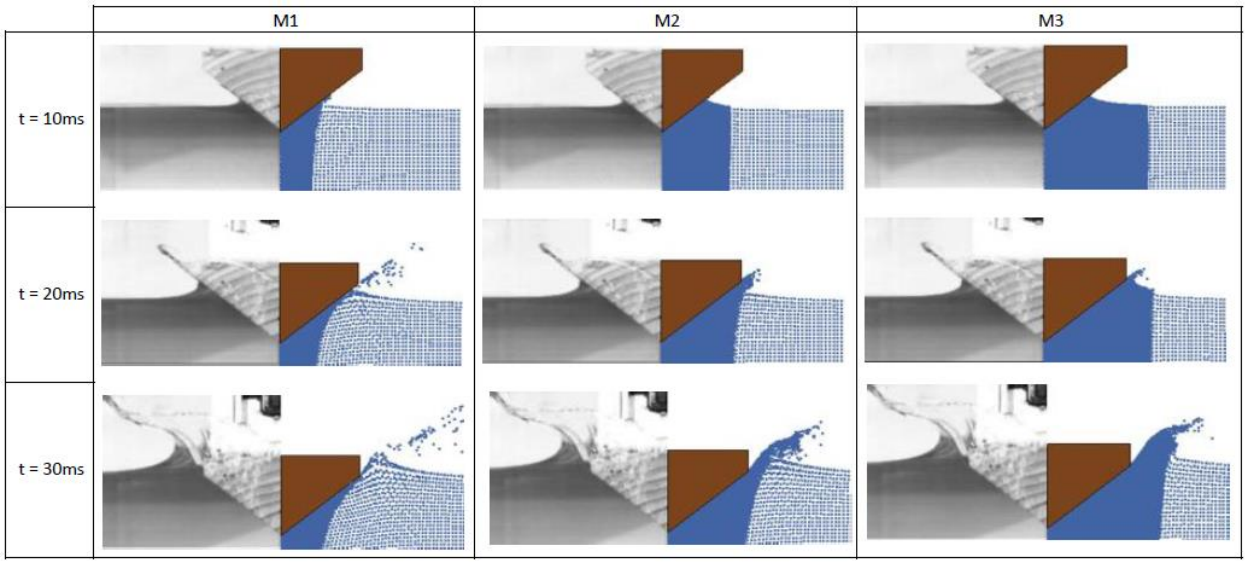

Figure 4.25: Comparison of results for the HGMS 40° deadrise wedges

The penetration depth and force time history of each wedge deadrise angle for the HGMS are shown in Figure 4.26, Figure 4.27, and Figure 4.28. The accuracy of the displacement results compared to the von Karman equation vary amongst the different wedge angles, however all three particle distributions match a very similar displacement slope and finial penetration depth. One phenomenon that is not fully captured in the 20° and 30° deadrise angles is the slight change in the displacement plot when the wedge depth begins to level off. This however, is captured in the 40° wedge as the leveling off is not as well defined and is more vertical in nature. A pattern throughout all three deadrise angles is that M1 exhibits a shallower penetration depth than M2 and M3. This can be attributed to the influence of the coarser particles, which occupy more volume in M1 and therefore more mass associated per particle. This 'heavier' particle requires more force to be displaced and results in a shallower penetration depth. This is a slightly better model when compared to the von Karman equation for the 20° wedge which is a more violent impact, however for the 40° wedge it under predicts displacement. Comparing the results from M2 and M3, there is very little change in displacement slope and magnitude confirming that the particle distribution is converged.

The force time histories displayed in the following figures have a strong correlation to the results predicted by Sydow. The 20° and 30° deadrise angles have an identical impact ramp and match the peak impact force within five percent. The maximum impact force for the 40° over-

predicted compared to Sydow by 12.5 percent, but the maximum force is closer than that calculated by the VGMS.

The force results predicted by the von Karman formulation are severely under-predicted. The virtual mass term that is accounted for by Sydow and present in the qualitative results, is not calculated in the von Karman equation. This reduces the maximum von Karman impact force and does not accurately represent the physics. One aspect of the impact that is not fully captured is the force decay as the simulation decays much faster than the analytical results.

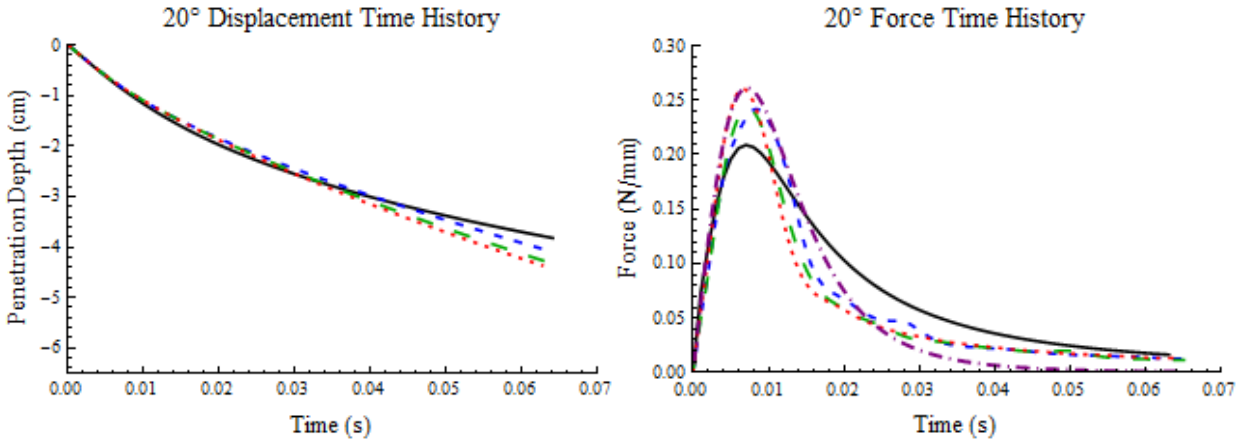

Figure 4.26: HGMS displacement and force time histories for the 20° deadrise angle wedge

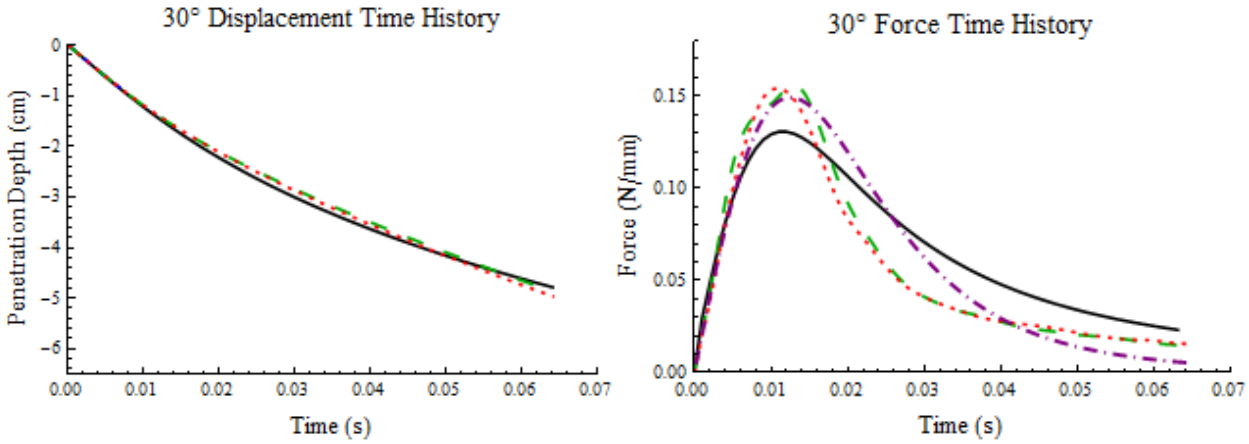

Figure 4.27: HGMS displacement and force time histories for the 30° deadrise angle wedge

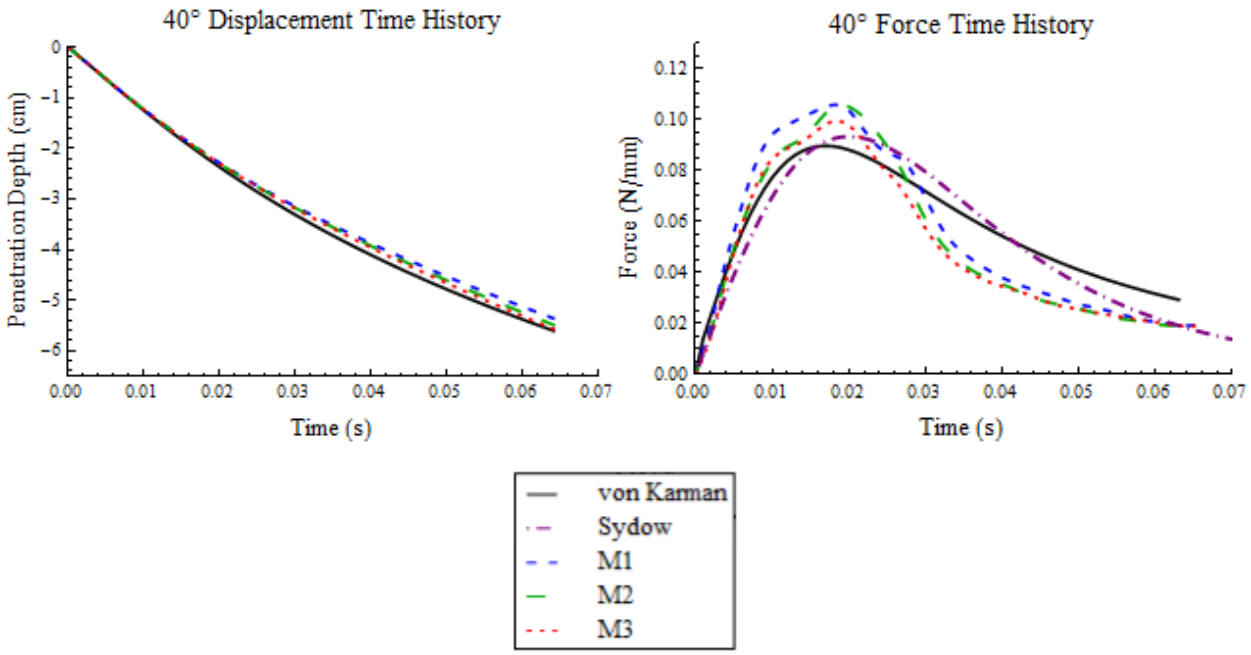

Figure 4.28: HGMS displacement and force time histories for the 40° deadrise angle wedge

4.8 Summary of the Advanced Mesh Schemes

In this chapter, a new methodology to analyze the impact of wedge into a calm body of water has been investigated. The actual properties of water were used with the inherent compressiblity incorporated in the SPH particles. It was discovered that conventional FSI modeling methods were not capable of capturing the intricate physics of the event. A new meshing technique based on multiple resolutions of SPH particles was developed, combined with a larger quadrilateral Lagrangian brick element bath. Both a vertical (VGMS) and horizontal (HGMS) gradient were tested, with three size variations of dense particles to see the effects of mesh resolution on the convergence of the model.

For the VGMS, comparisons between wedge deadrise angle and depth of the dense mesh were drawn. For smaller deadrise angles, the impact force is high and produces a large wave formation. The wedge does not penetrate into the fluid as deep and therefore a shallower dense particle resolution is needed. Conversely, larger deadrise angles have a lower impact force and slice deeper into the water with a decreased wave form; a deeper dense particle section is required.

The HGMS proved to have several limitations in its ability to accurate model fluid physics. The transition from the dense to the coarse gradient introduces several problems with the formation of the wave. The coarse particles could not be displaced as easily as the lighter dense particles and

resulted in a delayed wave formation causing the free surface of the water to be altered and slightly raised. A memory error resulting in numerical instabilities was also a problem with the 30° wedge and the M1 gradient. However, all three of the gradients performed well when impacted with the 40° wedge. The qualitative results closely mirrored those from experiments and the impact force time history matched Sydow's formulation much closer than the VGMS.

Overall, the discrete gradient mesh scheme with different particle resolutions improved accuracy with only moderate increase in computation time when compared to high density resolution models. The VGMS proved to be more versatile than the HGMS as better results were achieved without any numerical instability errors. A vertical gradient of SPH particles is recommended and will be used in subsequent analyses.

Chapter 5. Small-Scale System Level Experimental Studies

Moving forward from the initial rigid body wedge studies, a larger damage incorporating FSI analysis will be conducted. Transitioning from a small wedge investigation to the analysis of a full-size passenger aircraft water ditching would be impractical; not only is there a severe difference in size between the two objects, but also the inability to validate the numerical model. To produce more relevant research, the analysis of a scaled passenger aircraft will be conducted. The aircraft is outfitted with an instrumented composite undercarriage to reflect the continued use of these materials in the contemporary aircraft designs. This chapter will focus on experimental testing and the methods utilized to develop an authentic ditching event that will be used to validate the numerical methodology.

To develop and test the methodology, the physical and virtual investigations were conducted on a $^1/_{36}$ scale Boeing 747-400. While this seems to be small, the model has a wingspan of 1.91 m and is a relatively large size model. Figure 5.1 is a comparison between the full-size aircraft and the model. For the results from the experimental and virtual tests to be analogous, it must be ensured that both models are impacting with the same speed and aircraft attitude. This is achieved with a physical test stand that can accurately and repeatedly control the physical conditions of the model aircraft at impact, which will be replicated in the numerical analysis.

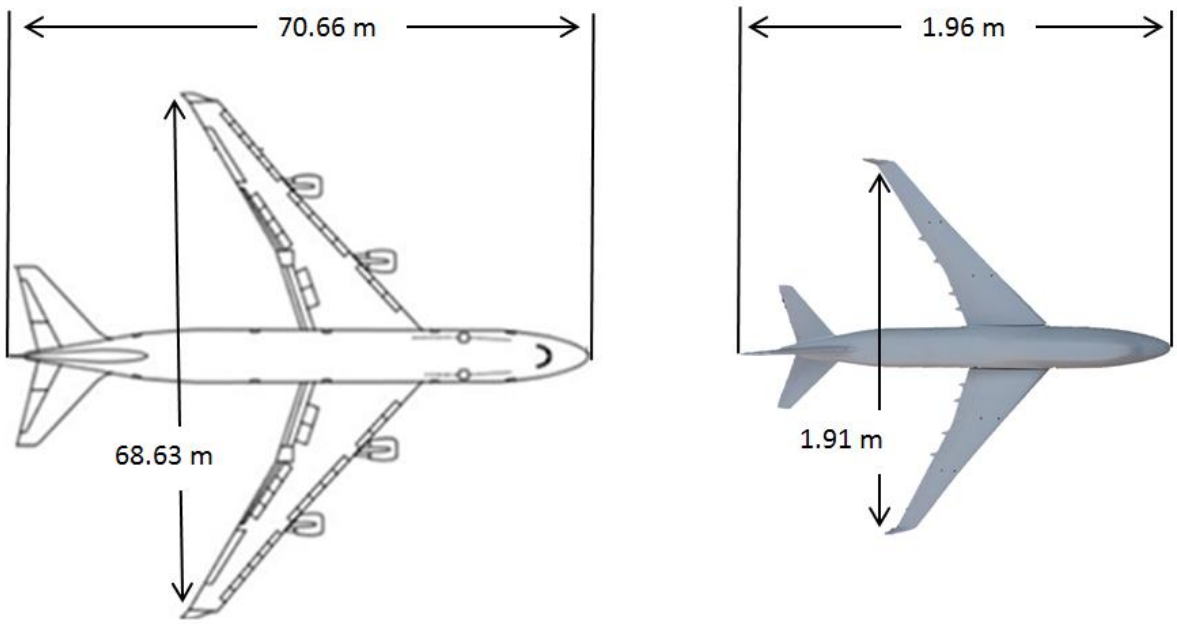

Figure 5.1: Size comparison between a full-size B747-400 and the scaled experimental model

5.1.1 Test Platform

To create an experimental platform capable of controlling the dynamics of the aircraft during the ditching impact, several test platforms were developed. The first iteration of the test stand developed by previous researchers consisted of a set of tensioned wires that guided the plane into the water (Figure 5.2). This test stand had several issues that required a redesign, but served as a good first iteration and highlighted features essential for future designs. The central concern with the guided wire design was that the aircraft was never released from the wires. This forced the aircraft to follow a set path throughout impact and altered the natural dynamics of the plane. By over constraining the plane, its path and pitch were constantly being altered by the guide wires resulting in unrealistic results. Another issue was the amount of tension required for the pulleys, supporting the plane, to travel smoothly could not be achieved. The wheels frequently got caught in a bind, which created difficulties in generating a consistent impact velocity.

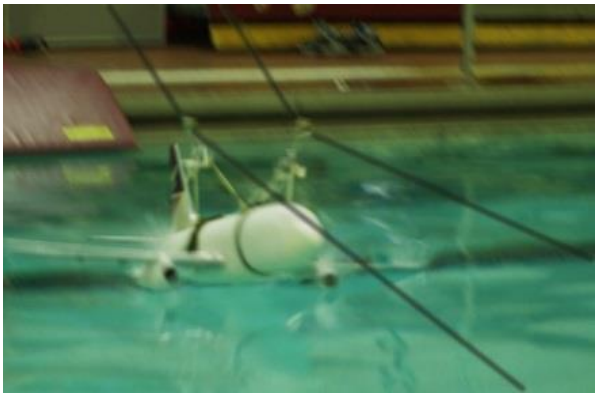

Figure 5.2: Scaled aircraft ditching conducted with tensioned wire test platform

To avoid these issues, a completely new test stand design was developed. Rather than using tensioned wires, a rail design was created. This platform enables control over the glide angle, pitch, roll, yaw, and speed of the aircraft until it is released just above the surface of the water. There is minimal influence on the dynamics of the plane throughout the approach and no influence during the impact into the water with the rail design.

The test stand is constructed from a set of rails supported by two towers. The rails are twelve feet long and are angled horizontally between the two towers. The height of each tower can be varied to produce a variety of incoming glide angles of the plane. The test stand is positioned beside the pool with the legs of the shorter tower placed edge. This lower tower supports the rails 1.22 *m* from the end, to produce an overhang above the water. The overhang was designed to release the plane as close to the surface of the water as possible to reduce the distance the plane is in free fall. This distance varies based on the angle of the rails, but at a rail angle of fifteen degrees the undercarriage of the aircraft is less than half a meter above the water. While this is a relatively small drop, it does factor into the relative velocity and pitch of the aircraft at impact. This will be further studied through motion analysis techniques.

The plane initially starts at the taller of the two towers and is attached to a cart. The cart has four casters, one at each corner, that roll smoothly through the rails and is outfitted with a mechanical release mechanism that opens on impact at the bottom. The plane is attached to the cart via a harness made of thin polyester webbing that is place tightly around forward and aft sections of the aircraft. At each section a line is attached to the webbing and formed into a loop. With a negligible profile and mass, the harness stays attached to the plane throughout the approach and impact into the water.

Two rail test platforms were developed. The first generation of the platform was functional and proved that the concept was valid, but required a long setup time and the tower sections began to deform due to weak materials composing the towers after several testing sessions. A model of the platform is shown in Figure 5.3. The towers and supports are composed of ¼ inch angled steel which deformed after repeated setups and impacts the aircraft is released. The towers also were cumbersome to move to and from the testing facility, as they were over three meters long.

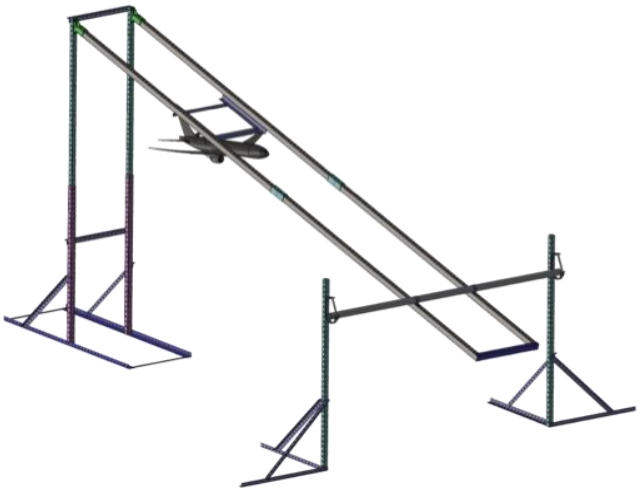

Figure 5.3: First generation rail test platform

To reduce setup time and create a structure that could handle the loads from repeated testing, a second generation test stand was constructed. The towers of this test stand are made of ¼ inch steel rectangular tubing, which much stronger than angle brackets. The back tower was also redesigned with a telescoping base. This allowed the structure to be moved easier and enabled faster setup time. An additional support tower located at the center of the railings was also added to the design. The middle tower reduced bending in the rails as the plane traveled down them and aided in the adjustment of the glide angle.

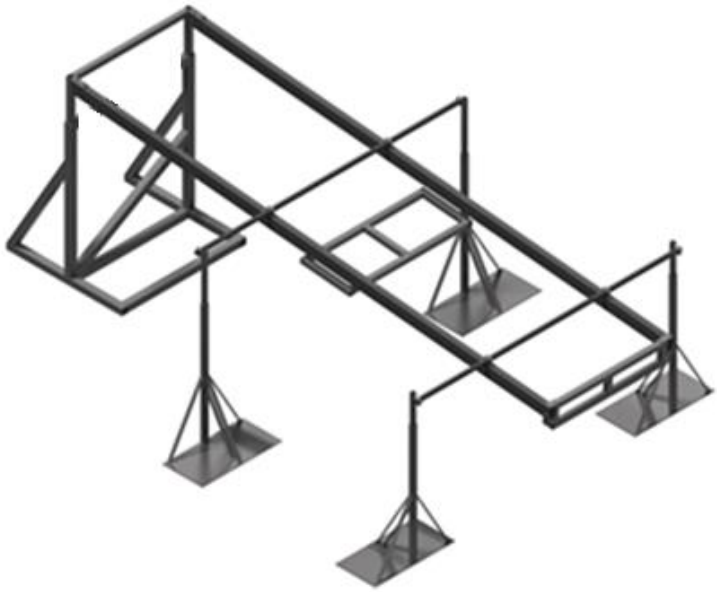

Figure 5.4: Second generation rail test platform

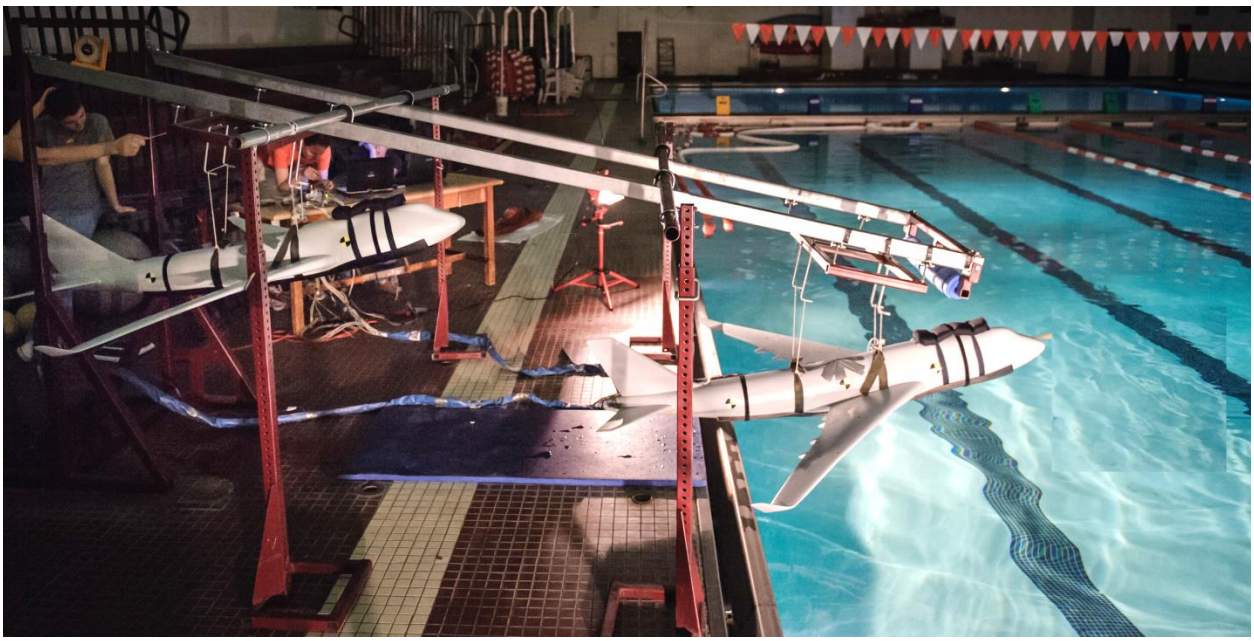

Figure 5.5: Aircraft at initial release and moment just prior to free-fall using the second generation test platform.

To create a ditching event with the scaled model as accurate as possible, the dynamics of the plane just prior to impact were studied. While the center of gravity is not of great importance relative to the aerodynamic center for this testing, due to the lack of lift generated by the wings, it

does play a critical role in the dynamics of the plane landing. The initial center of gravity (CG) for the model was skewed towards the tail of the plane due to the weight of the empennage and the absence of engines. This created a nose-up moment in the aircraft producing a pitch angle much larger than initially desired in the short distance the plane falls after being released by the test platform. To adjust this, the location of the center of gravity on a full-size B747 was researched. As with all aircraft, the CG is not at one specific location rather there is a forward and rearward limit to where the CG is located. This information was then related to the scaled model, where the middle of the CG limits was selected. To move the CG to the desired location a set of weights weighing 4.54 *kg* were strapped on top of the front fuselage. The weights were positioned vertically over the fuselage to minimize the interference with the water. This resulted in a balanced plane with a CG between the wings (Figure 5.6).

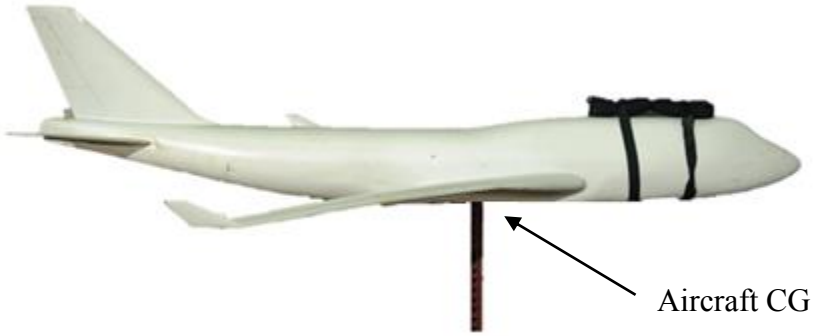

Figure 5.6. Scale model aircraft balanced at the center of gravity

5.1.2 Motion Analysis

To qualitatively compare the virtual results to that of the physical experiment, a high speed camera was used to record the impact. The camera is capable of recording up to 500 frames per second, but as the frame rate increases the viewing area decreases. To reach a balance between frame rate and viewing area, the experiment was recorded at 250 frames per second. At this decreased rate, the viewing area is capable of capturing the initial impact and brief moments after and is sufficient to compare with the simulation results. The analysis of these videos will also add insight into the small details of ditching that cannot be seen with the naked eye.

Three crash dots were placed along the fuselage of the aircraft at the forward, middle, and aft sections. By knowing a predetermined length in the video, the dark blue line, the crash dots can be tracked through frames of the video to measure the velocity and pitch of the aircraft. The teal and

red points are the location of the crash dots located at the forward and middle sections of the aircraft as it falls to the surface of the water.

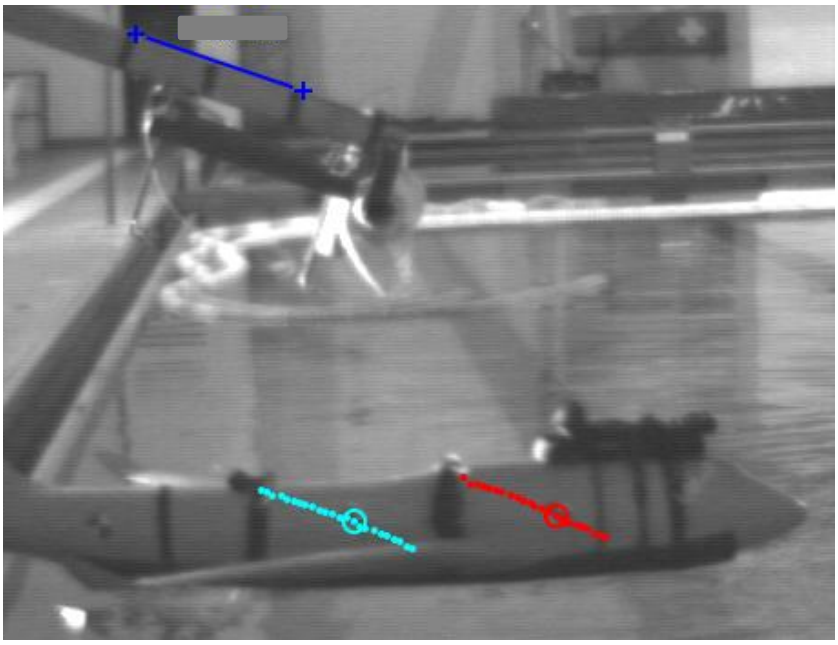

Figure 5.7: Motion analysis of aircraft as it glides to the surface of the water.

Each test is analyzed and documented into a spreadsheet (Table 5-1). The decent angle of the test stand rails is recorded and the components of velocity along with the overall velocity magnitude is measured. The approaching glide angle of the aircraft is recorded and the pitch of the aircraft at impact. A brief account of the tests is added to document the overall attitude of the aircraft at impact.

Table 5-1: Sample data collected from motion analysis

Trial Number	Rail Angle	x velocity	y velocity	vel magnitude	Glide Angle	Aircraft Pitch	Impact Description
	(degrees)	(m/s)	(m/s)	(m/s)	(degrees)	(degrees)	
1	-14.6	-3.12	-1.71	3.56	28.81	-0.5	Pitched Down
2	-14.0	-2.76	-1.55	3.16	29.30	6.5	Held Pitch
3	-15.8	-2.86	-1.51	3.24	27.76	4.5	Held Pitch
4	-14.3	-3.04	-1.48	3.38	25.99	4.9	Held Pitch

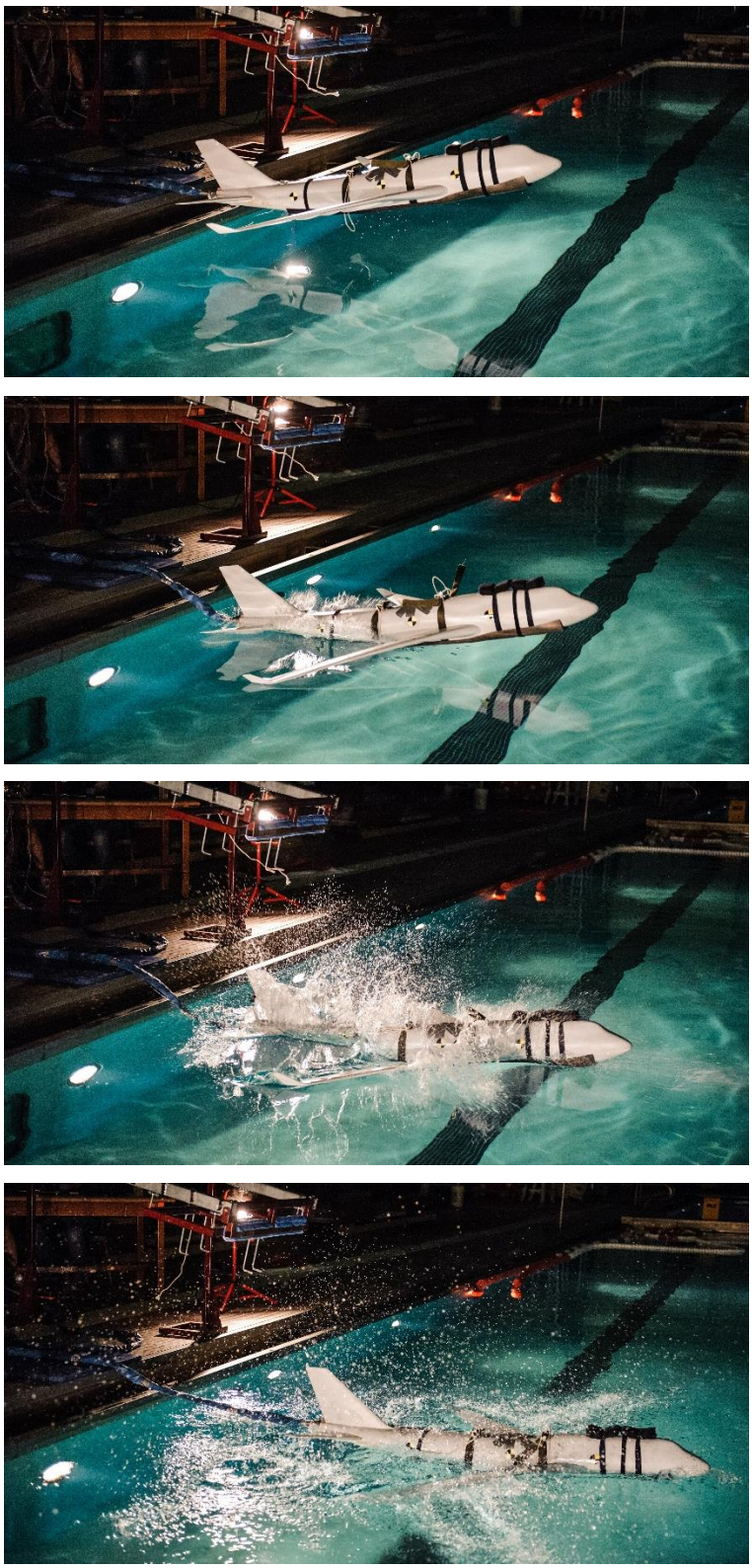

Figure 5.8: Experimental aircraft ditching impact progression.

An interesting phenomenon was captured during testing after the initial impact with the water. The aircraft, with a positive pitch angle, impacts the water initially towards the rear of the undercarriage. The nose then follows, slamming into the water. What happens next is interesting, as the nose of the aircraft rocks out of the water then levels with the water surface. This is due to the center of gravity and the moments created upon the undercarriage of the aircraft.

When the rear aircraft first impacts the water, it creates a high pressure on the surface of the water displacing the water in the form of splashing and wave creation. This creates a force on the undercarriage behind the CG, rotating the nose of the aircraft down. The entire undercarriage is now displacing water. As the aircraft continues forward the nose of the aircraft encounters the untouched surface of the water as the rear moves into the void once occupied by the front of the plane. This creates a nose-up moment and the nose is pitched out of the water. Once the forces on the rear and front of the aircraft at equivalent the aircraft moves forward with a level pitch.

5.1.3 Composite Data Analysis

To measure strain in the composite, ten rosettes of three rectangular strain gauges in a stacked construction were used (Figure 5.9a). Five locations were chosen as points of interest and a rosette was mounted on the top and bottom at each position (Figure 6.5). These locations are in the middle and rear of the aircraft as this is where first impact will occur with the water and the highest strain should be expected. Each rosette allows for laminate strain ε_x , ε_y, and $\gamma_{xy}$to be calculated in one precise location in the orthotropic material. This can be easily achieved through Equation 5.1 by setting the orientation of the gauges coincident to the effective laminate directions (Figure 5.9b)

$$\begin{aligned} \varepsilon_x &= \varepsilon_1 \\ \varepsilon_y &= \varepsilon_3 \\ \gamma_{xy} &= 2\varepsilon_2 - (\varepsilon_1 + \varepsilon_3) \end{aligned} \qquad 5.1$$

The gauges have a 350 *ohm* resistance, which is preferable as this higher resistance decreased lead wire effects and reduces heat generation in the gauge [52]. Both of these aspects are important as there is a lead wire length of ten meters to the data acquisition system and the gauges are stacked and mounted on a material with poor conductance properties. To protect the strain gauges from the repeated short-term water immersions during testing, water resistant RTV silicone rubber coating was applied. The RTV was recommend by the strain gauge manufacuter to seal and protectant the gauges from water.

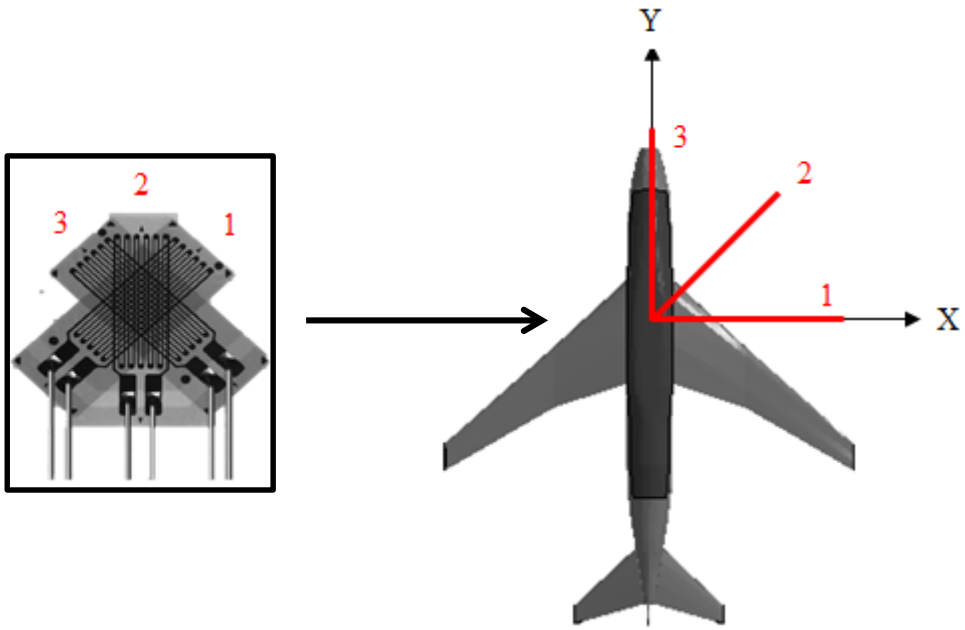

Figure 5.9: a) A rosette of three rectangular strain gauges in a stacked pattern [53]. b) The orientation of the rosette on the undercarriage of the scaled aircraft.

To calculate the strength of the composite undercarriage, test strips were created with the same material, ply orientation of $[0/90]_s$, and cured at the same autoclave conditions as the undercarriage. This is important as laminate properties can be drastically different when the material is handled differently or subjected to different cure cycles. The 308.4 *mm* long strips were tested on an Instron tension test machine with a 50 *kN* load cell in accordance with ASTM standard D4018-99: Standard Test Methods for Properties of Continuous Carbon and Graphite Fiber Tows. The standard is relatively loose compared to other testing standards, in a way highlighting the difficulty in testing composite materials.

The standard allows for specimens to be cut into a dogbone configuration or simply left with a uniform width. It was decided that cutting a dogbone into the specimen could result in heat induced effects, such as matrix melting, without the proper tools so a uniform width specimen was tested. Additionally, specimens are allowed to be tabbed or untabbed. A tab, as it relates to composite testing, is a way to lock the specimen into the grips of the testing machine in an effort to reduce slipping. Composite materials are typically smooth, thin, and very strong making it difficult to get a firm hold of the material in the grips. Initially, a tab fabricated of a fine aluminum mesh pressed against the composite and covered by a thin solid aluminum piece was used. Three

tests were conducted with this tab configuration, but the results were inconclusive due to the grips slipping. When the load on the specimen reached about 30kN, the composite would slip in the grips and never reach failure. Another tab method was tried this time placing 80 grit sandpaper between the specimen and the grips. This this method prove very successful and the ultimate strength of the composite laminate was capable of being reached. In accourdance with the ASTM standard, four samples were tested under quasistatic conditions with a displacement rate of 2 *mm/minute*. The modulus of the laminate enabled testing to calculate the effective engineering properties E_x and E_y considering the cross-ply symmetric orientation of the laminate.

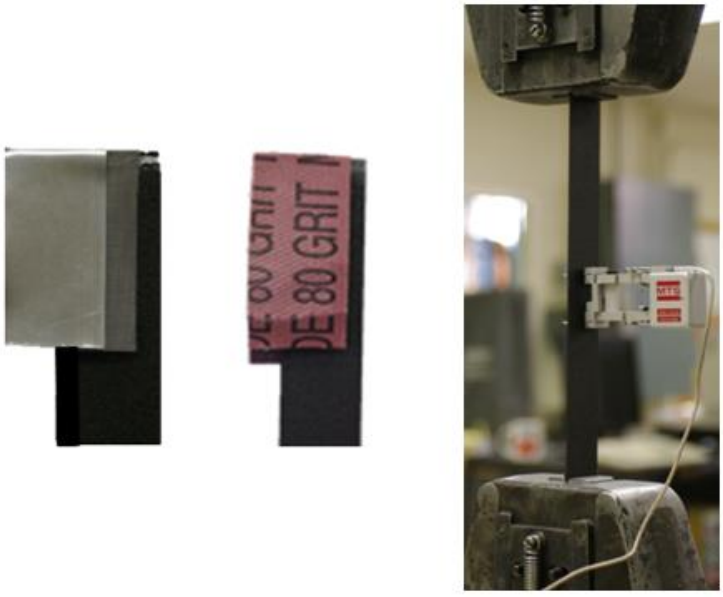

Figure 5.10: a) Aluminum tab; b) 80 grit sandpaper tab; c) Composite specimen in the grips of the tension test machine with an extensometer attached.

The results of the four samples are plotted in Figure 5.11 comparing stress vs. strain. Each test displays an initially linear relationship, with an average effective modulus of 75.74 *GPa* and standard deviation of 2.22 *GPa*. These results are inline with what is expected for a graphite reinforced composite based on CLT. Two clear failure mechanisms are clearly seen in the results. The horizontal areas are an effect of delamination, as layers begin to de-bond from one another. Once delamination occurs, the ultimate strength of the composite occurs soon after as the fibers break and the specimen in no long capable of carrying load. The change in ultimate strength can be attributed to several factors. First, there could be slightly different imperfections within each specimen, initiating failure at different strains. A greater possiblity however, and the reason why

composite materials are so difficult to test, is the influence of the grips holding each end. Failure could have initialed based on how tight each specimen was clamped in the jaws. The optimum amount of pressure is difficult to achieve because without enough pressure the specimen will slip, while too much pressure will induce fiber breakage at the grip. The composite undercarriage is not expected to experience enough force to break during ditching testing, so an exact ultimate strength value is not of too great of importance.

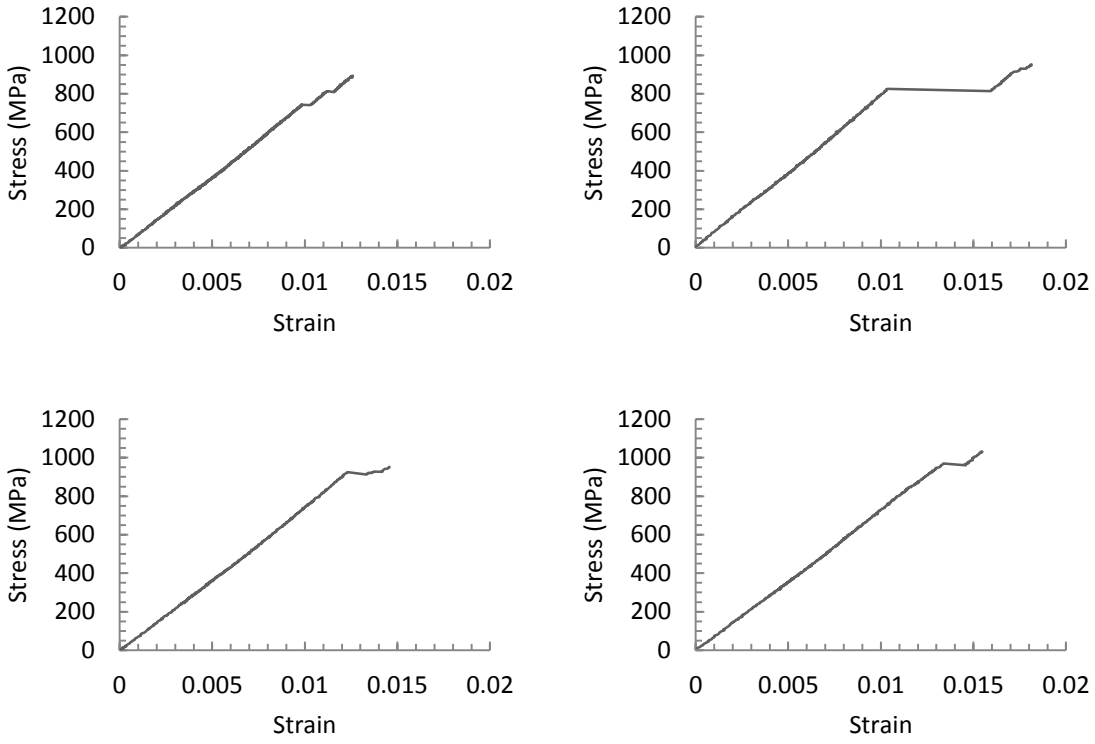

Figure 5.11: Experimental stress vs. strain results of four $[0/90]_s$ specimens.

5.1.4 Data Acquisition System

The data recording device used to measure strain in the composite undercarriage is a National Instruments C-series 9236. The 8 channel data acquisition (DAQ) system is developed exclusively for measuring strain and has an internal quarter-bridge strain gauge configuration. The DAQ system records 10 kilo-samples per second per channel with an accuracy of 24 bits. Two of these DAQs are used in tandem during testing to which accommodates 16 of the 30 strain positions along the undercarriage. While it is nice to have two DAQs, it means that only two full strain locations can be recorded per run.

5.2 Experimental Ditching Quantitative Results

There are six locations along the composite were strain measurements were taken. The locations are spread along the undercarriage to analyze the difference in strain based on the progressive initial impact with the water. Due on the manner in which the aircraft was ditched in the experiments, with a nose-up pitch orientation, the rear of the fuselage should experience more strain than the forward section. This is due to the impact force being greatest at first impact and reducing as drag forces act on the aircraft and slow it down.

Figure 5.12 is top view of the instrumented composite undercarriage, with the forward section pointing to the right. The strain gauges mounted to the composite and are concealed under the grey colored RTV silicon coating and are numbered above the photo. There are also gauges that directly correlate to the underside of the locations to give a deeper understanding to the overall strain through the material. Most the gauges are mounted directly in the middle of the undercarriage, but there are two that are place along the sides to see if there is any unknown strain effects in these rounded areas.

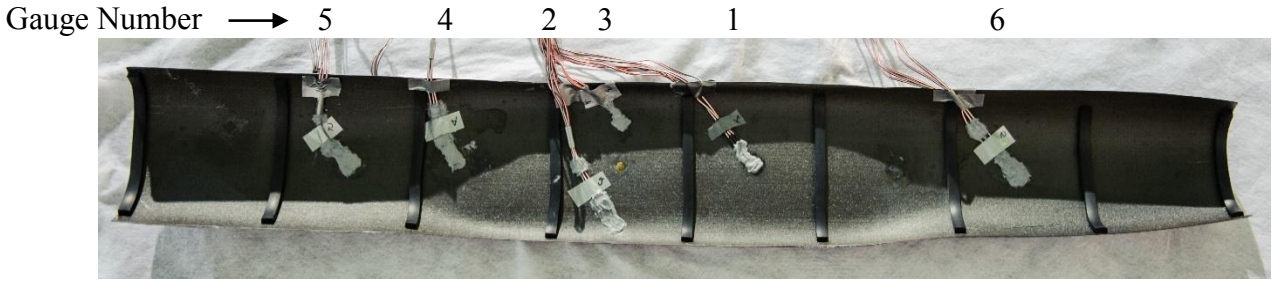

Figure 5.12: Instrumented composite undercarriage

The black strips throughout the undercarriage are ribs used to offset the composite undercarriage from the body of the aircraft. The ribs are composed of a stiff rubber that is pressed firmly against the undercarriage of the aircraft. This offset allows space for the strain gauges and replicates the rib structure of a real aircraft structure allowing the composite to have a realistic deformation.

Numerous tests sessions were conducted with both the first and second generation test platforms. The repeatability in the experiment however, was hard to control. As documented in Section 5.1.1, the first generation test stand deformed, altering the manner in which the aircraft was released each test. These problems were reduced with the second generation test platform,

with an improved design and stronger materials. Testing was still a slow and tedious process as it important that each test was repeated exactly as the previous trial, as only two stain locations could be recorded at once due to the limited recording ability of the data acquisition system. The results were then combined in an effort to analyze the strain at all six locations with one overall ditching orientation.

The results in this section were gathered from a single testing session with the test platform configuration and aircraft orientation remaining constant. The values of these trials gathered through slow motion analysis, are shown in Table 5-2 along with a description of the impact. It can be seen that the there is a slight difference between all trials, but overall the repeatability of the experiment was achieved.

Table 5-2: Motion analysis data with constant aircraft orientation and velocity.

Trial Number	Rail Angle	x velocity	y velocity	vel magnitude	Glide Angle	Aircraft Pitch	Impact Description
	(degrees)	(m/s)	(m/s)	(m/s)	(degrees)	(degrees)	
1	-11.5	-2.54	-1.59	3.00	-32.11	12.7	Held Pitch
2	-11.5	-2.58	-1.95	3.23	-37.18	6.8	Lost 3 degrees of pitch
3	-11.5	-2.58	-1.68	3.08	-33.01	8.1	Held Pitch
4	-11.5	-2.61	-1.90	3.23	-36.05	9.4	Held Pitch
5	-11.5	-2.54	-1.92	3.19	-37.12	9.4	Held Pitch
6	-11.5	-2.57	-1.72	3.09	-33.81	10.1	Held Pitch
7	-11.5	-2.67	-1.87	3.26	-34.95	10.2	Held Pitch
8	-11.5	-2.60	-1.88	3.21	-35.94	10.6	Held Pitch
9	-11.5	-2.63	-1.91	3.25	-35.99	10.4	Held Pitch
10	-11.5	-2.66	-1.84	3.24	-34.71	11.5	Held Pitch
11	-11.5	-2.57	-1.80	3.14	-35.04	12.4	Held Pitch
Average	-11.5	-2.60	-1.83	3.17	-35.08	10.15	

Strain time history results are plotted in the following figures. Another difficulty in conducting this experiment, was the reliability of the strain gauges. Carbon fiber in general is a hard material to apply strain gauges and furthermore, the structure was repeatedly submerged in water. This is the reason why several of the strain locations are not plotted. Data from these gauges was either unrealistic or the gauge itself was accidently ripped off. The data that is shown, are the x, y, and xy (orientation shown in Figure 5.9) strain directions with top and bottom results at each location.

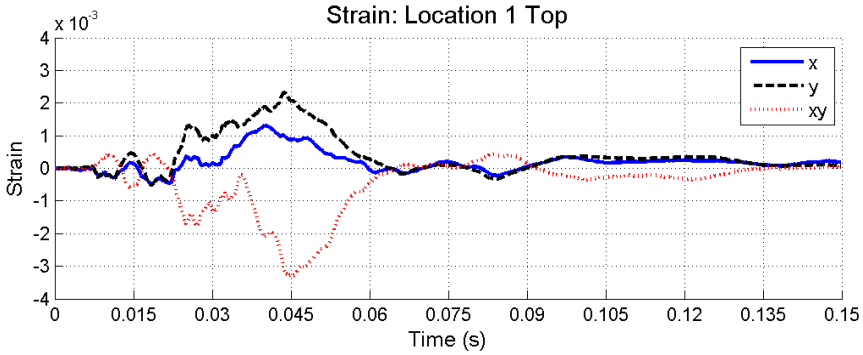

Figure 5.13: Strain time history at location 1

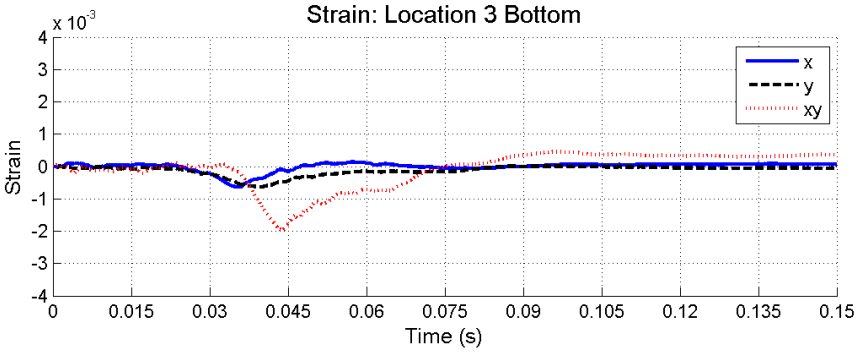

Figure 5.14: Strain time history at location 3

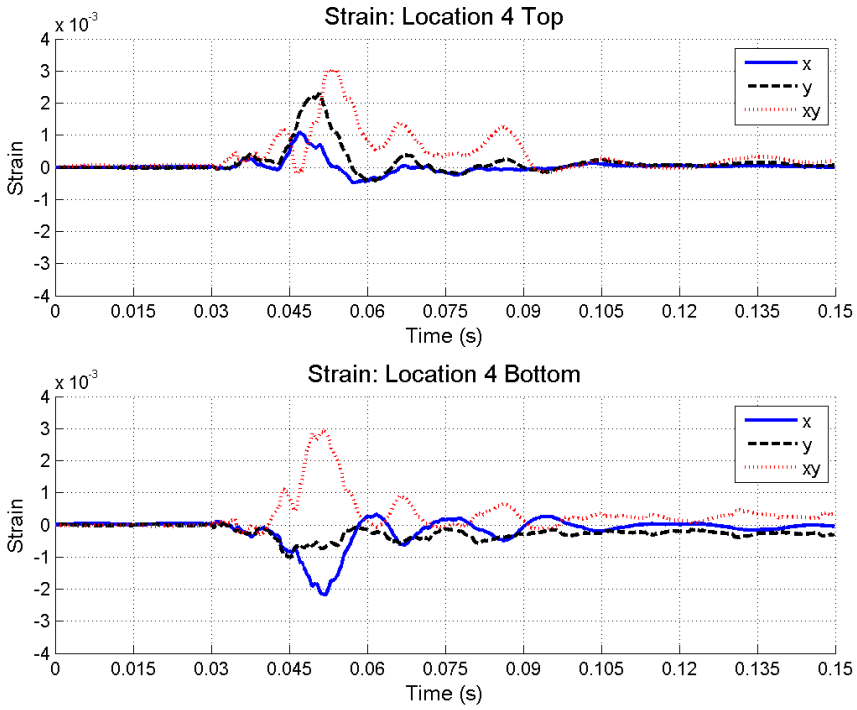

Figure 5.15: Strain time history at location 4

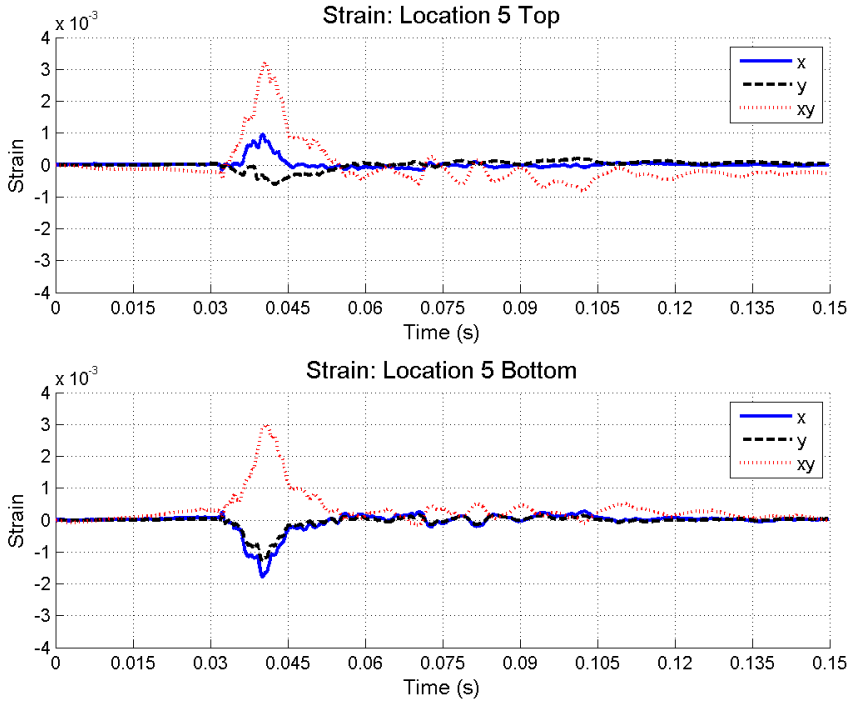

Figure 5.16: Strain time history at location 5

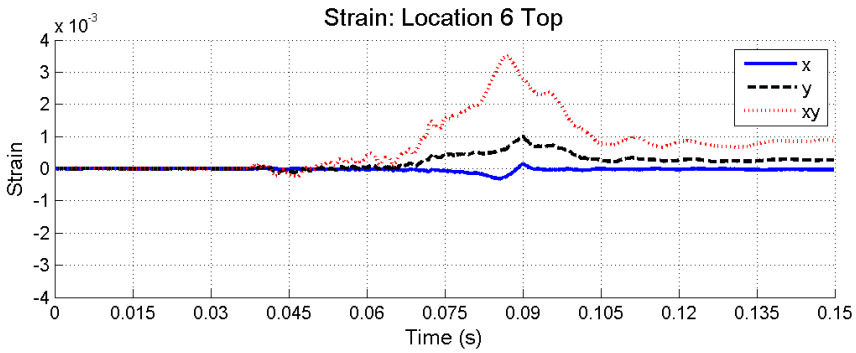

Figure 5.17: Strain time history at location 6

In analyzing the results it can be seen that numerous locations lacked data, with location two being completely absent. This again, relates to the difficulty in conducting this experiment. However, at some locations respectable data was recorded. All the results pass the sanity check with the shear strain, xy, being the largest recorded strain as it is the combined strain in both the x and y planes. Another check, is whether the strain at top and bottom locations are mirrored in form. Examining Figure 5.15, it is seen that the top and bottom locations do have realistic values. The top location has a positive x and y strain, meaning that the material is in tension. This is what is expected. With the impact pressure from the water, the undercarriage should be deforming in a concave down orientation between the ribs. This translates into a positive strain in the top location (closest to the aircraft) signifying the material is in tension. The inverse is also true for the bottom location. The strain is negative, meaning that the material is being compressed.

One aspect of the data that is not what was expected, is the maximum strain. In the test, the aircraft was given an average pitch up angle of 10.15°. With this orientation, the rear of the undercarriage will impact the water first resulting in a higher strain with the forward section having the least strain. This is not shown in the data. The maximum strain in the rear and forward gauges is very close, around $3x10^{-3}$. This indicates that the impact force due to the nose of the aircraft slamming into the water is larger than expected. This could be related to the position of the CG of the aircraft. The CG is skewed towards the nose of the plane. When the empennage of the aircraft hits the water, a moment is created pushing the nose of the aircraft into the water compounded by the forward CG. This produces higher strain rates than previously expected.

With the qualitative and quantitative results of aircraft ditching gathered through small-scale experiments, the numerical analysis of the event can now have a developed.

Chapter 6. Small-Scale System Level Numerical Results

Based on the physical experiments of a $^1/_{36}$ scale Boeing 747-400 conducted in Chapter 5, a numerical ditching analysis was performed. The ditching parameters of the aircraft gathered from motion analysis of the impact were all replicated in the simulation to match the experiment to validate the numerical results. The material parameters, modeling approach, along with the results of the test will be presented in this chapter.

6.1 Composite Material Models

To capture the deformation and strain throughout the composite, the undercarriage was given the deformable model card **Mat_54/55_enhanced_composite_damage*. This card is designed for composite specimens that are composed of unidirectional plies represented by shell elements. The material model is based on the Classical Lamination Theory and incorporates composite failure based on Chang-Chang or Tsai-Wu failure theories. Tsai-Wu was initially selected as the failure criterion, which along with CLT, is developed in Chapter 3.4.1. However, if was found that the failure properties that can be specified within the card are only operational when the Chang-Chang criterion is selected. This is not catastrophic though, as the two theories differ slightly only in the tensile and compressive matrix failure formulation [43]. An element is deleted when all layers (integration points through the thickness) have failed. The status of each layer can be outputted in the output file relating information as to what failure mode occurred.

This material card was used to define the material properties inside the **Part_composite* keyword. Defining the part in this manner, rather than through the *section* card, reduces defining a composite part with three cards, down to two. In this keyword the material properties along with the element formulation, orientation, and thickness of each ply is defined.

The element formulation used to model the deformable undercarriage is the Belytscho-Wong-Chiang (BWC) shell element. The undercarriage is expected to bend and warp and this must be accounted for in the element formulation. The BWC is a co-rotational bilinear shell element

with reduced integration. To properly represent a composite material using shell elements, the *LAMSHT* box must be set to one in **Control_shell* keyword. This turns on Lamination theory within the shell, without this the element will have a stiffness much greater than specified. This element was found by *Charoenphan et.al* to correctly model curvatures and stresses with in balanced and symmetric composite elements well [54]. When compared to shell element formulations the BWC is also a fast calculating element requiring only ten percent more CPU time of the most basic element formulation [55].

To ensure the composite response is equal to that of the fabricated composite, a numerical tension test was performed on a single element with the material properties found in the physical experiment. The element was prescribed the same boundary conditions of those in the experimental test, with two nodes fixed and the other two given a displacement of 2 *mm/minute* (Figure 6.1).

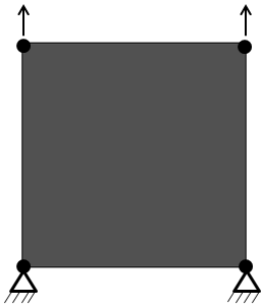

Figure 6.1: Loads and boundary conditions applied to the single element numerical tension test.

The results of all four experimental tension tests along with numerical tension test are plotted in Figure 6.2. The numerical analysis matches the experimental tests well with the average modulus, delamination and fiber breakage points accurately modeled. The material model damage parameters are now accurately predicting the behavior of the undercarriage layup and can be inputted into the aircraft simulation.

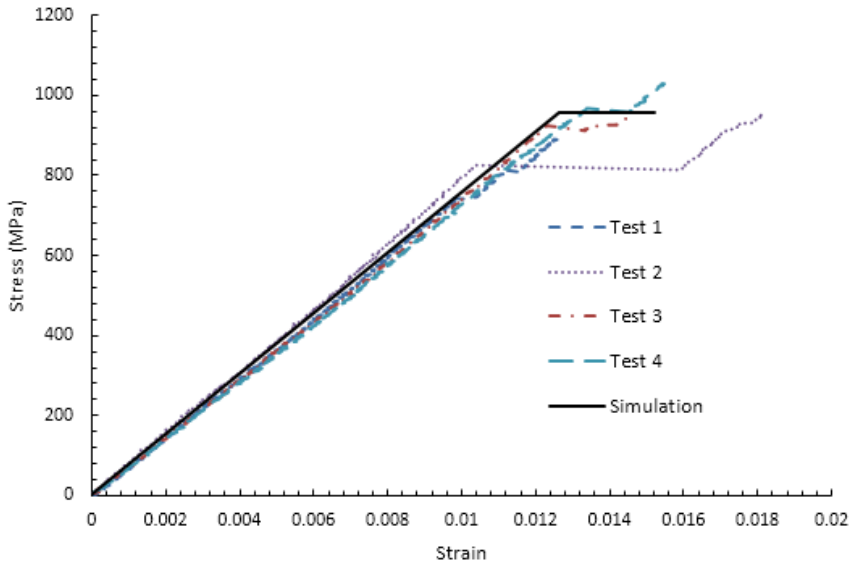

Figure 6.2: Comparison between physical experiments versus numerical simulation

6.2 Modeling Approach

One of the most important aspects of conducting an accurate FEA, is meshing. A handsome mesh reduces computation time, numerical instabilities, and makes it easier to calculate a correct solution. When first meshing the aircraft, the automatic mesher produced distorted elements shapes with short side lengths (Figure 6.3). Due to the way the time step is calculated as explained in Section 3.1, a very small increment was obtained which resulted in extremely long run times. To reduce computation time of the aircraft, two modeling strategies were applied: defeaturing and partitioning.

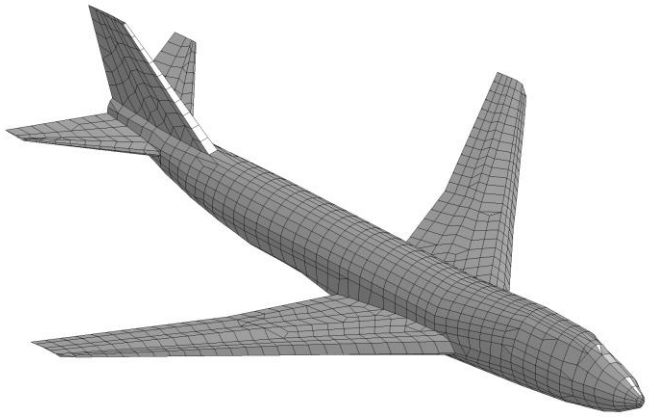

Figure 6.3: Initial aircraft mesh scheme

Defeaturing is a technique that reduces the unnecessary features of an object while still maintaining the overall characteristics. In modeling the aircraft, this was done by removing the winglets and radome. The geometry of both of these features require many elements of a very small size. The main area of interest on the plane is the composite undercarriage, so having elements that increase computation time in an area that is not necessary is bad modeling practice.

Partitioning is another method to create uniform elements to improve accuracy. It reduces the geometry of the object into smaller sections in an effort to control the mesh. Once the object is partitioned, the edges of the partition can be seeded with nodes to control exactly where the elements will be formed. Partitioning does involve extra time in the modeling development process, but rewards users with more accurate results and faster computation time.

The density of the rigid aircraft mesh is important when specifying contact. While the aircraft appears to have an overly dense mesh, a coarse mesh has the possibility of producing contact instabilities. Rigid bodies have very little effect on calculation time, as stress and strain are not computed. The general guideline is to have a rigid body mesh equivalent to that of the deformable body it will contact, to promote proper distribution of contact forces. While it is not realistic to have a mesh density of the aircraft equal to that of the meshless particles representing water, a moderately dense mesh of Figure 6.4 is a good middle ground.

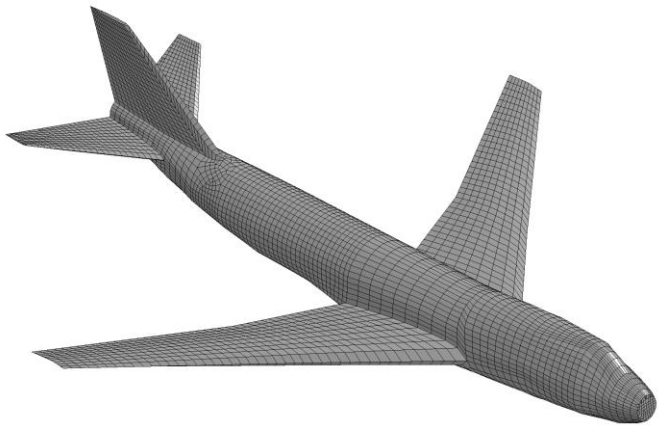

Figure 6.4: Aircraft mesh scheme after partitioning and defeaturing were performed

After the mesh for the aircraft was developed, efforts were focused on creating the composite undercarriage. Modeling the boundary conditions between the aircraft and the composite undercarriage proved to be challenging. In the physical model, there are nine equally spaced rubber ribs adhered to the undercarriage. These ribs provide protection of the strain gauges

while roughly representing the internal structure of an aircraft. The composite is mounted to the belly of the plane by two straps that are wrapped around the composite. Initial models tried to replicate these conditions by creating strips of solid elements and giving them the properties of rubber found in the literature (Figure 6.5). Initially this worked fine as the aircraft and undercarriage glided to the water surface, but at contact numerical errors occurred. The rubber elements hourglassed and terminated the simulation. Numerous methods were tried to fix this, but did not work. Alternatively, the solid elements were removed and in their place nodes were tied from the aircraft to the undercarriage. These boundary conditions do not fully model the experimental test, but the rib pieces were constructed out of a dense rubber and this strategy is a form of defeaturing the problem.

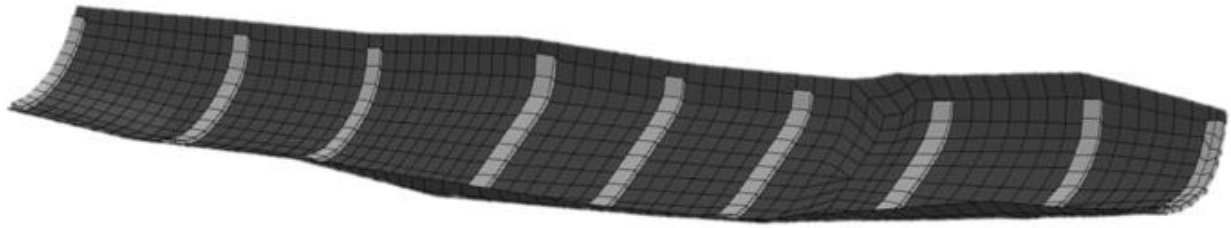

Figure 6.5: Mesh of composite undercarriage

The water for the aircraft ditching simulation was modeled with a similar methodology that was developed in Section 4.3. A bath of SPH particles, arranged in a lattice configuration were placed at the area of impact. This impact area (Figure 6.6) is larger than the wingspan of the aircraft to ensure that the aircraft does not contact the Lagrangian elements that surround the particle bath. Symmetry was not used in this model due to the behavior of the aircraft when it is ditched with different attitudes. In the simulations presented in this paper symmetry could have been applied, but when the aircraft is ditched with yaw angle, which was not conducted due to time constraints, it is not a valid assumption.

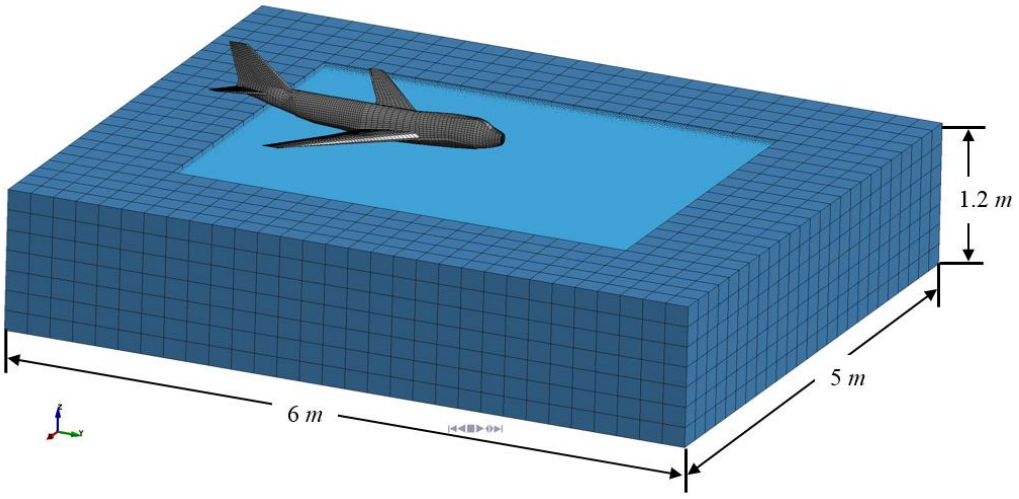

Figure 6.6: Layout and dimensions of the aircraft ditching model

The von Mises stress-time history of the composite undercarriage is plotted in BLANK. The stress contours are shown at 5*ms* intervals, with the first contour being prior to impact, to confirm that the initial stress state in the structure is zero. At impact, the stress reaches a maximum of 15 *MPa* along the bottom of the undercarriage. With a small 3°picth angle of the aircraft modeled in the simulation, this makes sense as the impact force will act on a larger area than it would for a higher pitch angle. After the initial impact, the stress moves to the forward section of the undercarriage when the nose of the aircraft crashes into the water. As the aircraft moves through the fluid, the stress moves irregularly throughout the undercarriage.

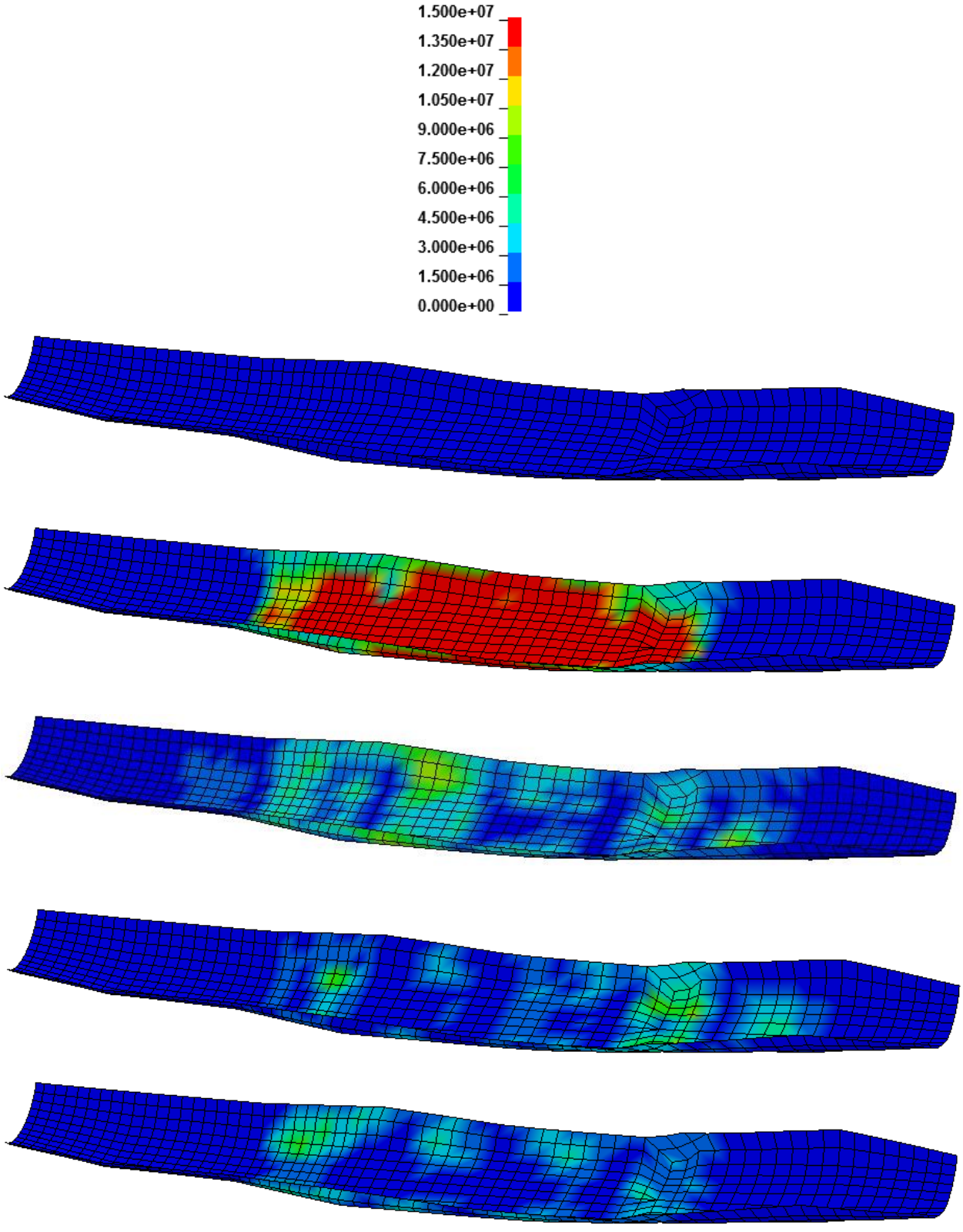

Figure 6.7: von Mises (*Pa)* stress-time history contours at 5*ms* intervals.

Chapter 7. Full Scale Aircraft Simulations

Even with the advancement of numerical analysis techniques, results mean little without proper validation. FEA is a valuable tool for analyzing structures, but errors can be made throughout the model development process and within in the code itself. This is the reason why engineers must carefully examine simulations, using insight gained through formal education to ensure the correct physics of the event are present. One method to guarantee this, is through the comparison of numerical models to physical experiments. Models can be validated against experiments to ensure accuracy. Where this method falls short however, is in analyzing large complex events. Sometimes measurements cannot be performed or the cost of the experiment is too expensive. This brings us to the analysis of full-size aircraft ditching events. Aircraft are too expensive to constantly test the crashworthiness of the structure and limited assessment of progressive damage can be attained. The work presented in this thesis outline the steps taken of creating a methodology, based on small-scale experiments, to create an accurate numerical model. Simulations validated against small-scale experiments give faith that the model is accurately capturing the physics of the event. This methodology can then be scaled up to larger models through dimensional analysis with the confidence that the simulation is valid.

7.1 Dimensional Analysis

Dimensional analysis is a method that reduces the physics of a complex event into several significant terms that capture the overall behavior of the event [56]. It revolves around the idea of similarity; allowing objects with the same basic physical characteristics, but different sizes to be related to one another. Based on the number of parameters chosen to describe the event, numerous dimensionless parameters, or pi terms, can be calculated; however one term will always be dependent on the others as shown in Equation 7.1. Dimensional analysis is useful in analyzing aircraft crashworthiness as it is unrealistic to be able to crash a full-size plane for this study, but plane models are readily available.

$$\Pi_1 = f(\Pi_2, \Pi_3, \dots, \Pi_n) \tag{7.1}$$

To apply dimensional analysis to water ditching conducted in this research, one must decide which elements of the physics in the event want to be maintained from the full scale to the small scale. Previous researchers conducted dimensional analysis of water ditching based on the Froude number [57] and the analysis could also be applied with the Reynolds number. However, both the analyses are related to the properties of the water, and not necessarily accounting for the impact on the structure. A description of each parameter will be presented next.

The Froude number is a dimensionless parameter that relates the inertia forces on a body to gravitational forces. The parameter is used in fluid mechanics as a way to calculate the characteristics of a wave. When $Fr < 1$ the flow is subcritical and the surface waves can move upstream; $Fr > 1$ is a supercritical flow and waves move downstream; and when $Fr = 1$ the flow is critical and the waves move at the same velocity of the flow [28]. In ship hydrodynamic design, the Froude number is used to calculate the drag on the ship from the waves created in the wake. To calculate the Froude number (Equation 4.3) the velocity of the fluid is divided by the square root of gravity times a characteristic length. Waves will of course be created during a ditching, however the FSI not only involves a fluid, but also the aircraft. If the Froude number was used as the basis of the dimensional analysis, then only the characteristics of the fluid are evaluated, which is not the main objective in this study.

$$Fr = \frac{V}{\sqrt{gL}} \tag{7.2}$$

To characterize different fluid flow regimes the Reynolds number is calculated. The Reynolds number is dimensionless ratio of internal forces to viscous forces in a fluid. The flow is characterized into three regions; laminar, turbulent, and the transition zone in between. Comparing Reynolds numbers through similarity is common in fluid dynamics. The number is calculated based on the density, velocity, and viscosity of a fluid and a characteristic length. However, like previously stated with the Froude number, this parameter accounts for fluid properties with no consideration of the dynamics of the structure.

$$Re = \frac{\rho V L}{\mu} \tag{7.3}$$

To create a ditching impact force on the scaled model equivalent to that experienced by a full-size aircraft, both linear momentum and conservation of energy were considered. The properties of soft impact were broken down and placed into three categories that affected the event;

fluid properties, structural geometry, and external forces. The parameters related to aircraft ditching from each of this categories is shown below.

Fluid Properties: ρ, μ

Geometry: A

External Forces: w, v_0

For similarity to be applicable, the geometry of the smaller model must match that of the full-size aircraft. The geometry of interest, is the initial impact area of the aircraft. This area is composed of the undercarriage and the underside of the wings and depending on the pitch of the aircraft, changes. Instead of trying to calculate the area of impact for each separate case, the scale ratio of the model compared to the full-size aircraft was used; as the aircraft will have. The initial velocity of the aircraft was selected as the dependent variable as it can be controlled relatively easily in the physical experiment.

The number of dimensionless parameters that can be created from the assembled variables is equal to the number of variables, minus the number of characteristic dimensions. Based on the number of variables found above and combining those that are composed of one another, two non-dimensional parameters that can be calculated; one based on fluid density and the other fluid viscosity.

$$v_0 = f(\rho, A, w, \mu) \tag{7.4}$$

To calculate the non-dimensional parameter, three characteristic dimensions are used as a basis: mass (M), length (L), and time (T). Each variable in Equation 7.4 is reduced to these basic dimensional terms.

$$\left(\frac{L}{T}\right) = f\left[\left(\frac{M}{L^3}\right), (L^2), \left(\frac{ML}{T^2}\right), \left(\frac{M}{LT}\right)\right] \tag{7.5}$$

Conducting the analysis based on the density of the fluid, the dimensionless parameter in Equation 7.6 is calculated. While Equation 7.7 is based on the viscosity of the fluid.

$$\Pi_1 = v_0 \left(\frac{\rho A}{w}\right)^{\frac{1}{2}} \tag{7.6}$$

$$\Pi_2 = v_0 \left(\frac{\mu A^{\frac{1}{2}}}{w}\right) \tag{7.7}$$

As shown, the Pi terms that are developed incorporate the parameters that are found in both the Froude and Reynolds numbers. While the prominent parameters are not explicitly written in the calculation, the properties that used to calculate the dimensionless numbers are present. To calculate the required velocity to be achieved by the model (denoted with subscript *m)* to replicate the physics in a full-scale aircraft (denoted with subscript *f)*, each pi term is equated to itself based on the properties of each individual event. Equation 7.8 is the equation developed based on Π_1.

$$\left[v_0\left(\frac{\rho\, A}{w}\right)^{\frac{1}{2}}\right]_{model} = \left[v_0\left(\frac{\rho\, A}{w}\right)^{\frac{1}{2}}\right]_{full-size} \tag{7.8}$$

This can be easily solved, as all the variables are known except for the velocity of the model aircraft.

$$v_{0_m} = v_{0_f}\left(\frac{w_m}{\frac{A_m}{A_f}w_f}\right) \tag{7.9}$$

The same calculation can be performed with Π_2, resulting in a the model velocity calculation in Equation 7.10.

$$v_{0_m} = v_{0_f}\left(\frac{\mu_f}{\mu_m}\right)\left(\frac{A_f}{A_m}\right)\left(\frac{w_m}{w_f}\right) \tag{7.10}$$

To analysis outlined in this section present a methodology for scaling the physics of a small scale experiment to that of full size event. Dimensional analysis was used to relate the physics of the full-size aircraft ditching to experiments conducted on scaled aircraft models. This thesis, limited by time, will not cover numerically modeling the ditching of a full-size aircraft with this methodology. However, in the following section, an analysis of a full-size deformable aircraft fuselage section dropped into water will be presented.

7.2 Analysis of a Full-size Deformable Section Drop Test

In conjunction with members of the CRASH Lab, a numerical analysis of a deformable aircraft section drop test was conducted. The test was based on the Crash Simulation of Vertical Drop Tests of Two Boeing 737 Fuselage Sections [58]. In the report, the FAA conducted a drop test of a 3.05 *m* fuselage section of a Boeing 737 with an impact velocity of 9.14 *m/s* onto a hard surface. This analysis was done by the Lab to compare numerical results against those published

in the paper. In the future, the analysis will be expanded and a larger model of the entire aircraft will be simulated.

In an effort to expand the material covered in this thesis, the section was used to conduct a numerical analysis drop test into a pool of water using the developed ditching methodology All the primary components of the structure were modeled: the outer skin, frames, ribs, stringers, floor beams, and floor. The 8,870 *kg* section was dropped at 9.14 *m/s* into a 5 *m* deep water bath composed of only meshless Lagrangian particles. All the structural components were modeled with a deformable material card and aluminum 7075-T6, except for the outer skin and floor, which were made of aluminum 2024-T3 (Table 7-1).

Table 7-1: Aircraft section material properties

Material	Young's Modulus	Poisson's Ratio	Yield Stress	Ultimate Failure Strain
	(MPa)	-	(MPa)	(m/m)
Aluminum 2024-T3	73084.43	0.33	310.35	N/A
Aluminum 7075-T6	71705.48	0.33	243.07	0.05

The results of the test are shown in Figure 7.1 and Figure 7.2. In the first figure, the fuselage section is shown 0.2 seconds after first impact with the water. The dynamics of the fluid particles are marginally captured as splashing results, but more separation is expected. A finer particle resolution in future simulations is required for this to occur.

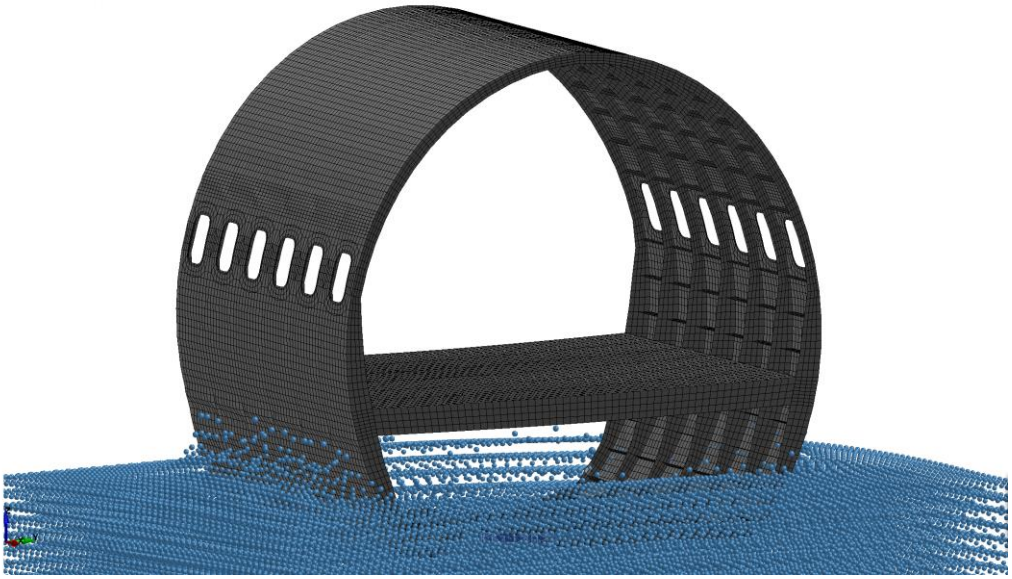

Figure 7.1: Drop test of an aircraft section into water.

A closer inspection of the fuselage at the same moment in time is presented in Figure 7.2. The force of the impact severely deforms the internal structure of the fuselage. The von Mises color contours and fringe level are shown in the figure. As expected, the impact produces a stress in the material beyond the yield stress resulting in deformation. The ribs, which take the majority of the force, buckle under the impact load and displace into the cargo bay. The floor deforms little, as small amounts of stress are registered in the floor beams. This is important as FAA regulations require that the floor remain undamaged to guard passenger safety.

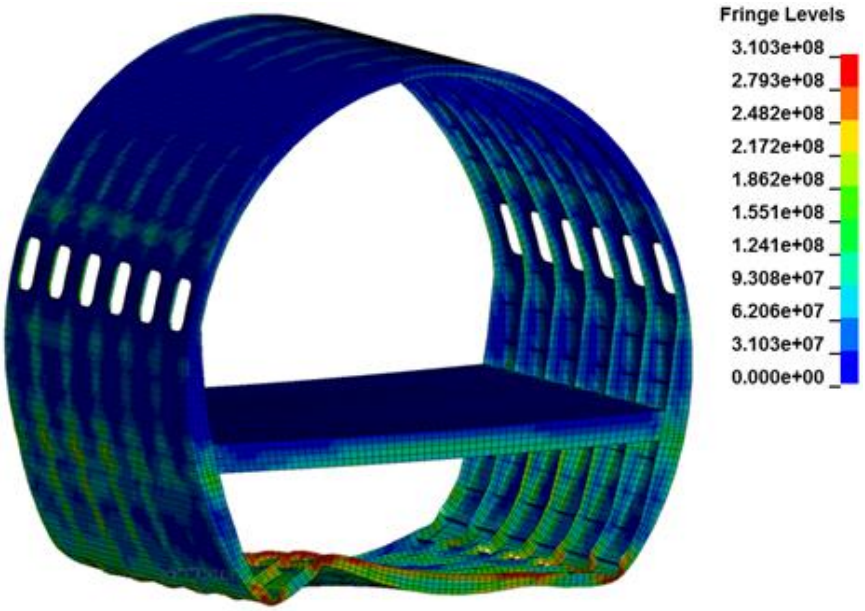

Figure 7.2: von Mises stress of the deformed aircraft section.

Chapter 8. Conclusions and Future Work

The focus of the research was to develop a numerical analysis methodology to capture the physics of aircraft water ditching. Numerically analyzing aircraft structural designs is key to providing safe, efficient, future aircraft. Models provide the ability to test the entire structure and examine the progressive failure of the entire system, which physical experiments cannot do, or are too expensive to conduct.

The underlying theory of this research is fluid-structure interaction. FSI is a difficult phenomenon to model, as two materials with extremely different properties must be coupled through contact. The ability to accurately model interaction between the two materials is vital as each one affects the dynamics of the other and overall evolution of the event. Before aircraft ditching simulations were conducted, an in depth analysis of FSI was performed. The water entry of a wedge was modeled. It was important when modeling the wedge, to make sure the methodology could translate to larger models. Accurate material properties were used throughout the simulations with the inherent compressibility found in meshless Lagrangian particles. Previous researchers forced incompressibility by altering the speed of sound through the fluid, but due to the limitations of this trick it was not used this this research. Through these methods it was discovered that the physics of the impact, specifically the evolution of the water was not captured accurately. Splashing was not present in the models, which resulted in the formation of a wave that was much too large and an unrealistic rise of the free-surface of the water ensued. A new modeling methodology was required.

Two novel advanced mesh schemes were developed. Both schemes relied on computationally efficient Lagrangian elements to enforce proper boundary conditions of the simulation, while placing meshless particles at the area of impact. Each mesh scheme had a section of dense and coarse particle resolutions, but differed the manner in which they were oriented. The VGMS, had a vertical gradient while the HGMS horizontally changed resolutions. It was found that these advanced mesh schemes represented the physics of the event with less than a six percent error when comparing the 20° and 30° deadrise angles to Sydow's analytical results. The qualitative phenomena absent in the initial model were captured with the advanced schemes nicely correlating

to experimental results. However, it was observed that the VGMS performed better at capturing the overall evolution of the impact and had no numerical instability issues. It is important to note that this methodology is size independent and can be used from mesoscale models to full system level simulations.

Water ditching experiments were then conducted on a small-scale Boeing 747. Multiple test platforms were developed with the final design was based on a set of angled rails being the best. With this design, the aircraft is attached to a cart that travels down two rails and is released just prior to impact with the water. The platform has no influence on the dynamics of the aircraft as it enters the water and after much testing proved to produce repeatable trials.

The aircraft was outfitted with an instrumented composite undercarriage to reflect contemporary aircraft structures. Strain gauges were mounted on the composite at six strain locations. At each location, the strain in the longitudinal, lateral, and shear directions on both the top and bottom of the undercarriage were measured. Results from these tests served as a method of validation for the numerical analysis. To ensure that the parameters specified in the numerical model were analogous to the experiment, motion analysis was performed on frames of video taken with a high speed camera.

Based on the FSI methodology developed from wedge water entry impacts, a numerical analysis of the small-scale experimental aircraft ditchings was constructed. The model featured a deformable composite undercarriage with carbon fiber material properties mounted to the fuselage of a rigid aircraft. The simulation was very computationally expensive due to the large size of the model and the small refinement of the fluid particles. Many of the phenomena seen in the experiment were captured with the numerical analysis. The dynamics of the simulated aircraft mirrored the physical test. Specifically, the nose of the aircraft slamming into the water, then slightly rising back out of the water as the empennage moves into the cavity of the fluid, then finally floating on the free surface of the water.

Lastly, methods were discussed on how to relate the small-scale experimental ditchings to that of a full-size aircraft. Dimensionless parameters were developed based on conservation of energy and momentum to ensure that the impact forces of the structures were accurately scaled. A preliminary numerical analysis of a full-size B737 section was tested into water. The progressive damage and deformation of the structure was captured throughout the impact. This model is in the

initial stages of development with the goal of modeling the ditching of a deformable, full-size aircraft with internal structure.

8.1 Recommendations for Future Work

The modeling techniques developed in this work are the first steps towards creating an efficient, effective, methodology capable of capturing the intricacies of FSI. Many aspects of FSI and aircraft water ditching were investigated in this research. As with all experiments, there are areas that can be further examined and improved upon. The physical test platform is one of these areas. Currently, the aircraft is released at the top of the rail platform and accelerated down the tracks by only gravity leading to a fixed velocity based on the angle of the rails. A new acceleration mechanism should be developed for an increased velocity range. Improvements to the instrumented undercarriage could also be made. The strain gauges mounted to the composite proved to be unreliable, mostly due to the fact the undercarriage is handled a lot and the gauges are accidently pulled by the lead wires. Mounting wireless strain gauges would improve the accuracy of the test data.

A large portion of this thesis was devoted to creating an accurate FSI methodology to accurately represent the physics of the fluid. The novel mesh scheme that was developed has areas that can be further researched and improved. More wedge deadrise angles should be investigated to calculate the required area of dense particles and find a trend between the two. The SPH densities of the dense and course sections can also be altered to find the best resolutions of the two that captures splashing while reducing computation time. A smooth gradient with particle distance changing radially is probably ideal.

Numerical modeling the aircraft was a difficult task. The scale difference between the aircraft geometry and fluid particle resolution was computationally expensive. Higher fidelity modeling strategies should be used, to create a more efficient simulation platform. This model must now be scaled up to the full-size aircraft. Primary internal structures must be modeled throughout the aircraft to create a realistic ditching event. This has been partially done with the section model in the previous chapter, but needs to be further developed to model the entire aircraft.

References

[1] 2012, "Water Landing," www.wikipedia.com.

[2] Federal Aviation Administration, 2013, "Destination 2025."

[3] Climent, H., Benitez, L., Rosich, F., Rueda, F., and Pentecote, N., 2006, "Aircraft Ditching Numerical Simulation," International Congress of the Aeronautial SciencesHumburg, Germany.

[4] Hall, K., 2012, "US Airways Pilot."

[5] Board, N. T. S., 2009, "Loss of Thrust in Both Engines After Encountering a Flock of Birds and Subsequent Ditching on the Hudson River US Airways Flight 1549," Washington, D.C. .

[6] Freissinet, S., 2011, "Worries About New Composite Made Airplane," www.1001crash.com.

[7] Von Karman, T., 1929, "The Impact on Seaplane Floats During Landing," No. TN No. 321, NACA.

[8] Wagner, H., 1932, "Phenomena Associated with Impacts and Sliding on Liquid Surfaces," ZAMM - Journal of Applied Mathematics and Mechanics / Zeitschrift für Angewandte Mathematik und Mechanik, 12(4), pp. 193-215.

[9] Sydow, J., 1938, Über den Einfluß von Federung und Kielung auf den Landestoß, Zentrale für wiss. Berichtswesen bei der Deutschen Versuchsanstalt für Luftfahrt.

[10] Mayo, W., 1945, "Analysis and Modification of Theory for Impact of Seaplanes on Water," No. 810, NACA.

[11] Dobrovol'skaya, Z. N., 1969, "On some problems of similarity flow of fluid with a free surface," Journal of Fluid Mechanics, 36(04), pp. 805-829.

[12] Zhao, R., and Faltinsen, O. M., 1996, Water Entry of Arbitrary Two-dimensional Sections with and Without Flow Separation.

[13] Cointe, R., and Armand, J. L., 1987, "Hydrodynamic Impact Analysis of a Cylinder," Journal of Offshore Mechanics and Arctic Engineering 109, pp. 237-243.

[14] Cointe, R., 1989, "Two-Dimensional Water-Solid Impact," Journal of Offshore Mechanics and Arctic Engineering, 111, pp. 109-114.

[15] Dalrymple, R. A., and Rogers, B. D., 2006, "Numerical modeling of water waves with the SPH method," Coastal Engineering, 53(2–3), pp. 141-147.

[16] Monaghan, J. J., 1992, "Smoothed Particle Hydrodynamics," Annual Review of Astronomy and Astrophysics, 30(1), pp. 543-574.

[17] Monaghan, J. J., 1994, "Simulating Free Surface Flows with SPH," Journal of Computational Physics, 110(2), pp. 399-406.

[18] Oger, G., Doring, M., Alessandrini, B., and Ferrant, P., 2006, "Two-dimensional SPH simulations of wedge water entries," Journal of Computational Physics, 213(2), pp. 803-822.

[19] Shao, S., and Lo, E. Y. M., 2003, "Incompressible SPH method for simulating Newtonian and non-Newtonian flows with a free surface," Advances in Water Resources, 26(7), pp. 787-800.

[20] Shao, S., 2009, "Incompressible SPH simulation of water entry of a free-falling object," International Journal for Numerical Methods in Fluids, 59(1), pp. 91-115.

[21] Anghileri, M., Castelletti, L.-M. L., Francesconi, E., Milanese, A., and Pittofrati, M., 2011, "Rigid Body Water Impact–Experimental Tests and Numerical Simulations Using the SPH Method," International Journal of Impact Engineering, 38(4), pp. 141-151.

[22] Shah, S. A., 2010, "Water Impact Investigations for Aircraft Ditching Analysis," Masters of Engineering, Royal Melbourne Institute of Technology.

[23] 2009, "Legacy in Safety: NASA Contributions to Knowledge in Aircraft Ditching," National Aeronautics and Space Administration.

[24] Fisher, L. J., and Hoffman, E. L., 1950, "Model Ditching Investigation of the Douglas DC-4 and DC-6 Airplanes," National Advisory Committee for Aeronautics.

[25] Belytschko, T., Liu, W. K., and Moran, B., 2000, Nonlinear Finite Elements for Continua and Structures, Wiley.

[26] Fisher, L. J., and Hoffman, E. L., 1949, "Model ditching Investigation of the Douglas DC-4 and DC-6 Airplanes," National Advisory Committee for Aeronautics.

[27] Fisher, L. J., and Hoffman, E. L., 1957, Ditching Investigations of Dynamic Models and Effects of Design Parameters on Ditching Characteristics, National Advisory Committee for Aeronautics.

[28] Fox, R. W., McDonald, A. T., and Pritchard, P. J., 2006, Introduction to Fluid Mechanics, Wiley.

[29] Thompson, W. C., 1972, "Ditching Investigation of a 1/30-Scale Dynamic Model of a Heavy Jet Transport Airplane," National Aeronautics and Space Administration.

[30] Montanes, L. B., Manez, H. C., Siemann, M., and Kohlgrueber, D., 2012, "Ditching Numerical Simulations: Recent Steps in Industrial Applications," Aerospace Structural Impact Dynamics International Conference Wichita, Kansas.

[31] Zhang, T., Li, S., and Dai, H., 2012, "The Suction Force Effect Analysis of Large Civil Aircraft Ditching," Science China Technological Sciences, 55(10), pp. 2789-2797.

[32] Francesconi, E., Anghileri, M., Castelletti, L.-M. L., and Pittofrati, M., 2008, "Survey of Feasible Numerical Approaches to Analyse the Behaviour of a Composite Skin Panel During a Water Impact," 26th International Congress of the Aeronautical SciencesGosier, Guadeloupe.

[33] Chandra, C., Wong, T. Y., and Bayandor, J., 2011, "Crashworthiness Assessment in Aircraft Ditching Incidents," 27th International Congress of the Aeronautical SciencesNice, France.

[34] Toso, N. R., 2009, "Contribution to the Modelling and Simulaiton of Aircraft Structures Impacting on Water," Doctor of Philosophy, Universitat Stuttgart.

[35] 2009, "Controlled Impact Demonstration," www.nasa.gov.

[36] Harewood, F. J., and McHugh, P. E., 2007, "Comparison of the Implicit and Explicit Finite Element Methods using Crystal Plasticity," Computational Materials Science, 39(2), pp. 481-494.

[37] Huebner, K. H., 2001, The Finite Element Method for Engineers, Wiley.

[38] Inman, D. J., 2008, Engineering Vibration, Prentice Hall International.

[39] Limited, W. H., 1995, "An analysis of the Response of Helicopter Structures to Water Impact," Stress department report SDR156.

[40] Liu, G. R., and Liu, M. B., 2003, Smoothed Particle Hydrodynamics: A Meshfree Particle Method, World Scientific Publishing Co. Pte. Ltd., Toh Tuck Link, Singapore.

[41] Hallquist, J. O., 2006, "LS-Dyna Theory Manual " Livermore Software Technology Corporation.

[42] Hyer, M. W., 2009, Stress Analysis of Fiber-Reinforced Composite Materials, DEStech Publications,Inc., Lancaster, Pa.

[43] 2012, "LS-Dyna Keyword User's Manual Volume II," Livermore Software Technology Corporation

[44] 2012, "LS-Dyna Keyword User's Manual Volume I," Livermore Software Technology Corporation

[45] Kuroda, K., Hamada, H., Hideki, H., and Shuigeru, I., 2007, "Forming of Aluminum Alloy Plate by Underwater Shock Wave of Explosive," 6th European LS-Dyna Users' Conference.

[46] Hertel, E. S., 1992, "The CTH Data Interface for Equation-of-State and Constitutive Model Parameters," Sandia Report SAND92-1297.

[47] 2012, "LS-Dyna Aerospace Working Group Modeling Guidelines Document," LS-Dyna Aerospace Working Group.

[48] Liu, M. B., Liu, G. R., and Lam, K. Y., 2002, "Investigations into Water Mitigation Using a Meshless Particle Method," Shock Waves, 12(3), pp. 181-195.

[49] Tabiei, A., 2012, "Tutorial Fluid-Structure Interaction in LS-Dyna," LS-Dyna Online.

[50] Webster, K., 2007, "Investigation of Close Proximity Underwater Explosion Effects on a Ship-Like Structure Using the Multi-Material Arbitrary Lagrangain Eulerian Finite Element Method," Master of Science, Virginia Tech.

[51] May, A., 1975, "Water Entry and the Cavity-Running Behavior of Missiles," No. TR-75-2, Naval Sea Systems Command Hydroballistics Advisory Committee

[52] "Strain Gauge Selection: Criteria, Procedures, Recommendations," No. TN-505-4, Vishay Precision Group.

[53] 2011, "General Purpose Strain Gages - Stacked Rosette," Vishay Precision Group

[54] Charoenphan, S., Bannk, L., and Plesha, M., 2000, "Use of LS-Dyna Shell Elements in the Analysis of Coposite Plates with Unbalanced and Unsymmetric Layups," 6th International LS-Dyna Conference.

[55] Tabiei, A., 2013, "LS-Dyna Tutorial Shell Elements in LS-Dyna," LS-Dyna Online.

[56] Sonin, A. A., 2001, "The Physical Basis of Dimensional Analysis," Massachusetts Institute of Technology

[57] Gretsch, J., Henry, M., Jivani, M., Liwanag, M., Rogers, A., Smisko, A., Wolf, D., Siddens, A., Satterwhite, M., and Bayandor, J., 2012, "A Virtual Aerospace Crashworthiness Modeling Platform: Part I, Substantiation Water Ditching Trials," 50th AIAA Aerospace Sciences Meeting including the New Horizons Forum and Aerospace Exposition, American Institute of Aeronautics and Astronautics.

[58] Jackson, K., and Fasanella, E., 2002, "Crash Simulation of Vertical Drop Tests of Two Boeing 737 Fuselage Sections," No. DOT/FAA/AR-02/62, Federal Aviation Administration.